ATOMKI
ANNUAL REPORT
2006

MTA atomki DEBRECEN

INSTITUTE OF NUCLEAR RESEARCH
OF THE HUNGARIAN ACADEMY OF SCIENCES
DEBRECEN, HUNGARY

INSTITUTE OF NUCLEAR RESEARCH
OF THE HUNGARIAN ACADEMY OF SCIENCES
DEBRECEN, HUNGARY

ANNUAL REPORT
2006

ATOMKI

Postal address:
P.O. Box 51
H-4001 Debrecen,
Hungary

Editor:
I. Rajta

HU ISSN0 0231-3596

Preface

Last year was rather quiet. There were no science conferences and there were few formal occasions at the Institute. A notable exception was a meeting of the European Committee for Future Accelerators (ECFA) held on 6-7 October here. Otherwise the year was a normal average year, largely devoted to work. In some of the long-term projects milestones were reached. It is thus appropriate to pause for a moment and summarize some of the results. It is reasonable to start the report with mentioning some of these significant results.

The Atomki contribution to the detector system called compact muon solenoid (CMS) has been completed. The CMS is one of the four systems of detectors designed for the particle-physics experiments at the Large Hadron Collider (LHC) to be installed this year at CERN, Geneva. Our job was to develop a system that is monitoring the position of the muon chambers of the CMS detector with an accuracy of 20 microns. The position is unavoidably changing mainly due to the strong magnetic fields. There are 10,000 LED light sources whose positions are monitored by 700 videocameras and their signals are analysed by 36 computers. The system is a harvest of six years' efforts. The test in magnetic field has demonstrated that the system works satisfactorily, and its installation has been started.

The understanding of the proton-proton collisions to be studied at the LHC requires second-order perturbative corrections of quantum chromodynamics. The second corrections had only been calculated for a few kinematically simple cases. Now, however, there has been significant progress in Atomki in elaborating a general procedure. The processes described by the second-order corrections may go with particle emission, but the particle may be subsequently absorbed in a loop-like pattern. There are in fact a two-loop contribution, a one-loop–one-particle contribution and a two-particle contribution. Each of them diverges, but their sum is finite. The technique elaborated is suitable for calculating this sum for a broad class of collisions.

Nuclear binding as a function of neutron number N or proton number Z suffers abrupt changes at certain 'magic' values of N or Z, and that is explained by the closure of the neutron or proton shells occurring at these numbers. One of the magic numbers is 20. Some members of Atomki bombarded a liquid hydrogen target by ^{28}Ne ions produced on-line at RIKEN (Japan). The observed states of ^{27}Ne cannot be explained without the assumption of a significant decrease of the $N = 20$ shell gap.

Nuclear shapes are similar to phases in that, in the limit of infinite particle number, they may be characterized by dynamical symmetries, and may show a first-order 'phase transition'. The phase transition is controlled by the relative weights of symmetry-breaking interaction terms. For finite systems the sudden change is smoothed out, but can still be observed. In the dipole collective (cluster) model of nuclei it was found that the U(3) symmetry survives as a 'quasidynamical symmetry' throughout the whole phase, up to the critical point, even in the domain of strong symmetry-breaking interactions. Thus the definition of phase in terms of quasidynamical symmetry survives in the whole phase diagram.

The presence of hydrogen in surface layers has been detected by means of electron spectroscopy.

In a large team we have been investigating the corrosion state of the structural elements of the Paks Nuclear Power Plant to identify the effects of the decontaminating procedures on the chemical passivity of the surface layers. The team published the first summary of their findings in 2006. They have established that the decontamination applied earlier has damaged

the passive surface layers, which aggravates corrosion. They are now developing better decontamination techniques. The Atomki contribution to this work is the *a posteriori* identification of the phenomena that damage the passive surface layers.

The tritium and radiocarbon emission from the Paks Nuclear Power Plant has been monitored by Atomki for about a decade. The report written in 2006 says the radiocarbon activity of the atmosphere in the 2-km region of the plant is 2–4% higher than the natural level, but it cannot be discerned beyond. The tritium concentration is at the detection limit.

Polymeric Cu(I) compounds which deposit metallic Cu films via thermally induced disproportionation were investigated as inks for copper direct-write. Particle induced X-ray emission and Rutherford backscattering analyses made in Atomki provided valuable insight into the various stages of the deposition process.

Many years of geochronological study of the Carpathian basin and its surroundings have now resulted in a comprehensive treatise that embraces the topography and chronology of 20 million years of volcanic activity in the Carpathian-Pannonian region.

Last year we had the Physics Days, the festivity organized for the broad public, for the twenty-seventh time. The highlighted topic was the physics of social phenomena. The first lecture was concerned with chaos, the most obvious physical feature of society, in more general terms. The lecturer was Prof. Tamás Tél of Eötvös University, Budapest. In the second talk Dr. Illés Farkas of Eötvös University gave a simple example for a social phenomenon that can be represented by a physical model. The phenomenon was mass fleeing in panic. Next Prof. János Kertész of Technical University, Budapest, gave an insight into the performance of the stock exchange. The following speaker, Prof. Zoltán Néda of Babeş-Bolyai University, Kolozsvár (Romania) discussed the distribution of property and income in society. He explained Pareto's law, well-known to economists, in physical terms. The Physics Days were concluded by a discussion of what the school can do against the proliferation of pseudo-scientific ideas. In the background there were, again, numerous visits and classes for school groups at the Institute, and Prof. Zoltán Trócsányi also held his 'master class' to secondary school pupils introducing them to particle-physics research.

There was another public occasion in autumn. In November we repeated the exhibition 'Radioactivity, a Facet of Nature', which had been on in 2002 for the first time. This was the first occasion we used the brand-new Kölcsey Convention Centre of Debrecen. While the exhibition was on, the Hungarian Atomic Energy Authority held a highly successful one-day conference for the public on nuclear energy with some Atomki contributions. We also contributed to another exhibition last year. To mark the 20th anniversary of the Chernobyl accident, there was an exhibition organized by the Central European University, Budapest. Our contribution was a decorative frieze made out of the diagrams of the radioactivity of the precipitation in Debrecen measured by Dr. Éva Csongor *et al.* from 1952 to 1987. A talk at a scientific session on the occasion of the Assembly of the Academy of Sciences was given by Dr. Zsolt Dombrádi.

The 'Honours List' should start with the Medal of Distinction conferred upon Prof. Dénes Berényi by the President of the Academy for his work as Chairman of the Committee of Hungarian Science Abroad and Chief Curator of *Domus Hungarica Scientiarum et Artium* on the occasion of his retiring from these posts. Dr. Zsolt Fülöp was awarded the title of the Doctor of Academy. He also won the Prize of the Physics Section of the Academy as well as the Szalay Prize of the Institute last year. Dr. László Zolnai received the 'Praise' of the Secretary General of the Academy.

But the most prestigious distinction was conferred on the youngest of the honoured. Gábor Katona received his PhD as a *Promotio sub auspiciis Praesidentis Rei Publicae*, and Dr. László Sólyom, President of the Republic, came to the University just to confer this award personally. The condition for this honour is that the candidate should receive all marks 'excellent' throughout his career from the secondary school to the graduate school as well as for his PhD thesis.

The reconstruction of the beamlines of the electrostatic accelerator VdG–5 has been successfully completed. Two instruments were received from the Studsvik laboratory of Uppsala University: the non-radioactive parts of the mass separator OSIRIS and a ^{3}He–^{4}He dilution refrigerator.

The funding of the Institute has not improved, but there was no dramatic decline either. We have been working on a major project called Debrecen Accent (Accelerator Centre) to be submitted in the framework of the National Development Plan based the seven-year EU budget. This project requires a rapid turn towards lucrative industrial innovation. We, however, would like to preserve research at the same time. The conditions for such projects have been changing with time, and we are still far from seeing clearly whether we can contribute to this grandiose scheme and whether we can benefit from it.

The financial and personnel conditions in 2006 are given in the pie charts to follow this Preface.

This Report, prepared in LaTeX, is available on the web at www.atomki.hu in PDF format.

Debrecen, 20 June 2007

Rezső G. Lovas
Director

Organizational structure of ATOMKI

Director:	R.G. Lovas, corresponding member of the HAS
Deputy directors:	Zs. Fülöp, D.Sc.
	S. Mészáros, C.Sc.
Finance director:	Dr. M. Pálinkás

- Secretariat (Scientific Secretary: Z. Máté, C.Sc.)
- Library (Librarian: Mrs. M. Nagy)
- Accounting (Head: Mrs. J. Sass)
- Basic Services and Maintenance (Head: Mr. I. Katona)
- Mechanical Workshop (Head: Mr. I. Gál)

Scientific Sections

Division of Nuclear Physics (Head: J. Cseh, D.Sc.)

- Section of Experimental Nuclear Physics (Head: A. Krasznahorkay, D.Sc.)
- Section of Electrostatic Accelerators (Head: I. Rajta, Ph.D.)
    - Nuclear Astrophysics Group
    - Ion Beam Analysis Group
- Section of Theoretical Physics (Head: A. Kruppa, D.Sc.)

Division of Atomic Physics (Head: Á. Kövér, D.Sc.)

- Section of Atomic Collisions (Head: B. Sulik, D.Sc.)
- Section of Electron Spectroscopy (Head: L. Kövér, Ph.D.)

- Section of Environmental and Earth Sciences (Head: Á.Z. Kiss, D.Sc.)
    - Laboratory of Environmental Studies
    - Radon Group
    - K-Ar Laboratory
    - Radiation- and Environmental Protection Group
    - QMS Laboratory
- DE TTK - ATOMKI Department of Environmental Physics (Head: S. Sudár, C.Sc.)
- Cyclotron Section (Head: F. Tárkányi, C.Sc.)
- Section of Electronics (Head: J. Gál, C.Sc.)

Data on ATOMKI

At present the Institute employs 196 persons. The affiliation of personnel to units of organization and the composition of personnel are given below.

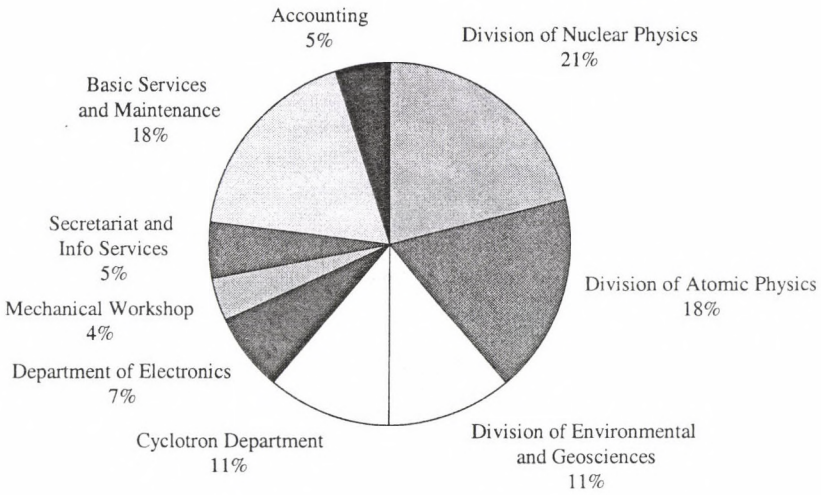

Figure 1. Affiliation of personnel to units of organization

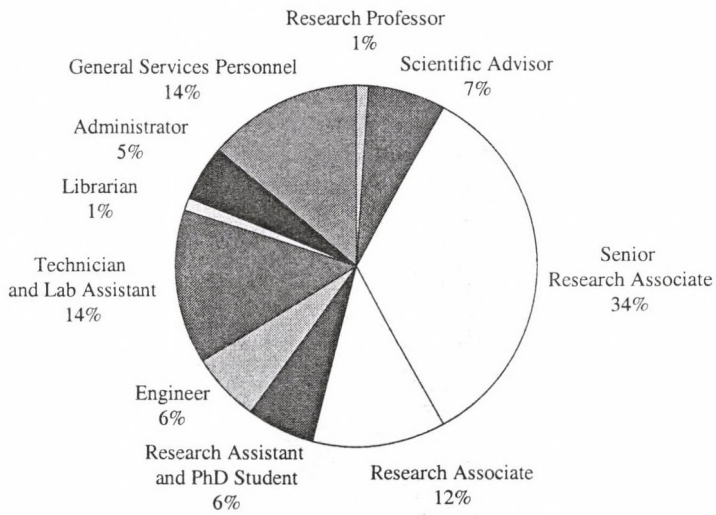

Figure 2. Composition of personnel

Finance

The total budget of the Institute for the year 2006 was 1235 million Hungarian Forints. The composition of the budget and the share of personnel expenditure within the budget are shown below.

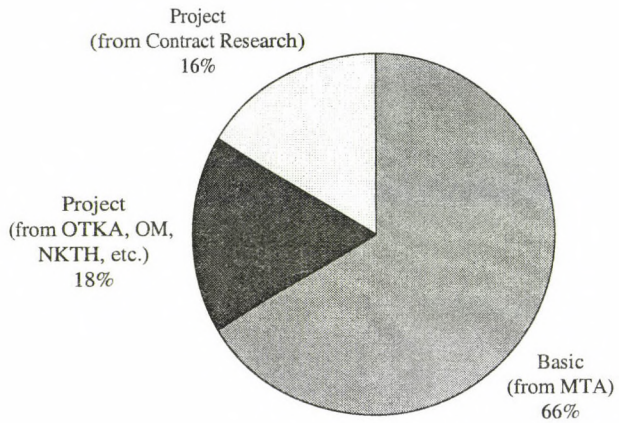

Figure 3. Composition of the budget of the Institute
MTA: Hungarian Academy of Sciences
OTKA: National Fund for Scientific Research
OM: Ministry of Education
NKTH: National Office for Research and Technology

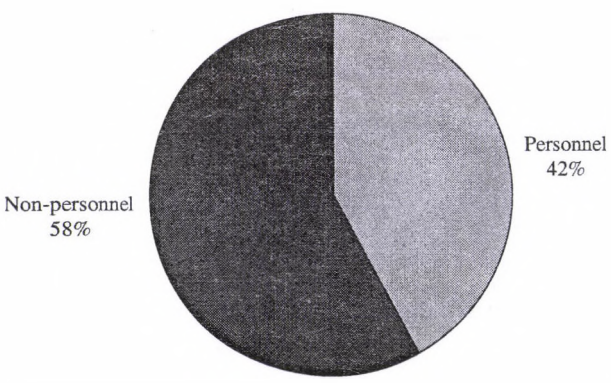

Figure 4. Breakdown of expenditure into personnel and non-personnel expenditures

Table of contents

Szalay and Szent-Györgyi, the forerunners of sonochemistry?

I. Török

Collecting the references to the works by A. Szalay (1909-1987), founder and first director of this Institute, I made a surprising observation. One of his first papers, entitled *Die Zerstörung von hochpolymeren Molekülen mittels Ultraschallwellen* [1], received an increasing number of citations in the last two decades. It was submitted from Szeged, where Szalay was working under the supervision of Albert Szent-Györgyi. The paper discusses whether ultrasound has any chemical effects. Szalay examined gum-arabic, starch and gelatine. He found that their viscosities were reduced when subjected to ultrasound. It was concluded that the large molecules were broken up.

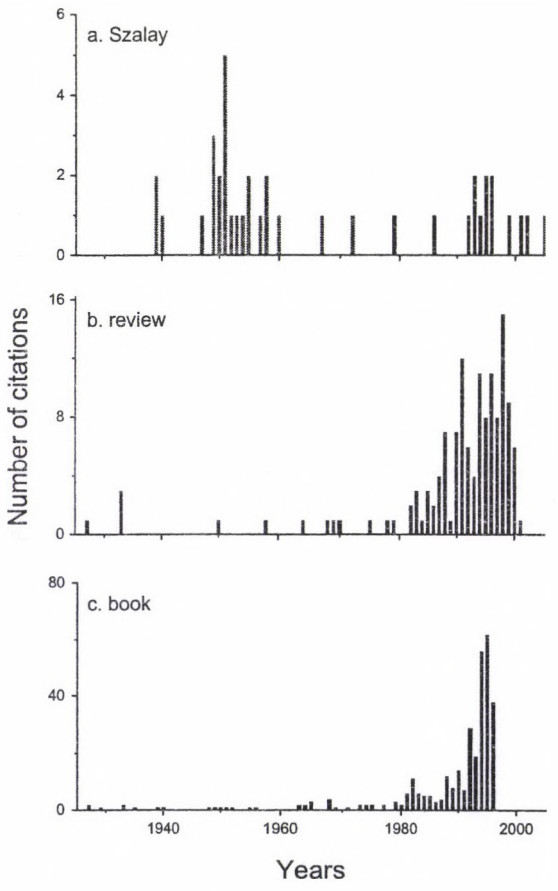

Figure 1. Time spectrum of references to the original paper [1] (a), of all citations in the review [2] (b) and in the book [4] (c), respectively.

The time spectrum of the citations of the paper is given in Fig. 1.a. Most of the citing papers were concerned with sonochemistry. One of them, a review [2], contained 135 citations. The time spectrum of the cited papers is shown in Fig. 1.b. The peak at 1951 shows the moment when sonochemistry became quantitative.

There was a short note on the same subject published in Nature by Albert Szent-Györgyi himself [3]. It was a sort of advertisement of Szalay's work published to attract the interest of a more general audience. Szent-Györgyi wrote that the subject was to be abandoned for shortage of funding. In this way, however, they missed to be the founding fathers of a new discipline, sonochemistry, which now has its own scientific society, journal etc. (e.g. European Society of Sonochemistry, Ultrasonics Sonochemistry).

At the end of the 20th century sonochemistry gave birth to an industry ('sonochemical engineering'), with large ultrasound generators etc. The numerous industrial applications include handling of sewage-waters, making bioetanol, treating crude oil to reduce its sulphur content etc. The story offers a good example for the delay between basic research and industrial applications. Sonochemistry operates with mechanical effects, which fits well into the trend called 'green chemistry'. Anyhow, Szalay and Szent-Györgyi became the forerunners of that industry, polymer sonochemistry, by about 50-70 years. In 1996 a review of sonochemistry was published in Hungarian, with Szalay mentioned in it [4]. The time spectrum of its sources is also given in Fig. 1.c.

The family of Professor Szalay remembers that he was very proud of this paper. Fig. 2 is his portrait of those times. Fig. 3 shows the marble memorial tablet put up at the entrance of ATOMKI on the occasion of the 10th aniversary of his death. This year will be the 20th anniversary.

Figure 2. The portrait of A. Szalay from the time of paper [1].

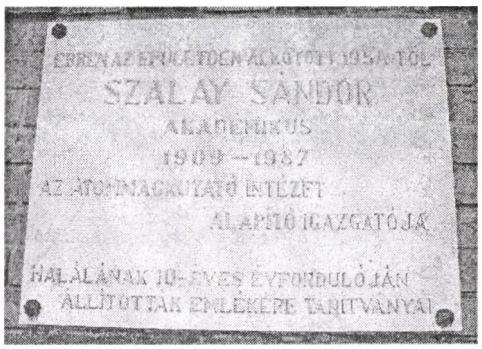

Figure 3. The marble tablet to the memory of academician Szalay, put up at the entrance of ATOMKI.

Thanks are due to the Szalay family for the portrait.

[1] A. Szalay, Z. Phys. Chem. 164A (1933) 234. *Note: S. Szalay published his papers as A. Szalay in the international literature. The equivalent of the Hungarian name Sándor is the English Alexander.*

[2] N. Kardos, J.-L. Luche, Sonochemistry of carbohydrate compounds, Carbohydrate Research 332 (2001) 115.

[3] A. Szent-Györgyi, Nature 131 (1933) 278.

[4] B. Török and Á. Molnár: Kémiai átalakulások mikrohullámú és szonokémiai aktiválással. In: A kémia újabb eredményei. 82. (1996). Akadémiai Kiadó, Budapest, 1997.

1.1 On the q-deformation of Lie-algebras by general complex parameter

J. Cseh and G. Tímár

The physical interpretation of a quantum-algebraic model is well-established when the deformation parameter is real or pure phase. Recently we have carried out quantitative investigations in order to see whether or not the dynamically symmetric limits of a two-dimensional interacting boson model can be bridged by quantum deformation [1]. The answer turned out to be negative for these canonical values of the deformation parameter. Previously a conjencture was put forward [2] on the possible bridging of the dynamical symmetries by deformations with general complex parameters. Now we made a quantitative test of this guess in the two-dimensional model [3].

In particular, we intended to check what kind of improvment can be obtained in this manner when the search is performed systematically, and the calculation includes the whole spectrum. The result is shown in Figure 1, where the deviation W between the q-deformed spectrum and the dynamically symmetric limit is shown as a function of the absolute value of the complex deformation parameter, and each single line corresponds to a given phase (which was changed also systematically between 0 and 2π). The upper, middle and lower parts show the landscape, intermediate and fine-resolution pictures around the minimum.

The conclusion is very interesting and somewhat surprising: not anly that the gap between the dynamical symmetries can not be bridged by allowing general defromation parameters, but in addition the general complex numbers can not improve at all the approximation that is available by a well-behaved pure phase-parameter.

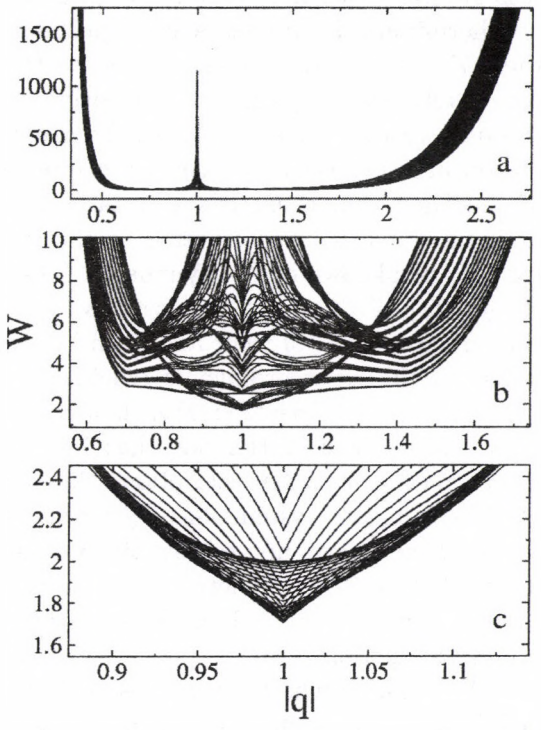

Figure 1. The deviation of the q-deformed rotational spectrum from that of the classical vibrational one for arbitrary q-values. Each line corresponds to a definite phase-value of the complex number, while its absolute value is shown on the horizontal axis.

[1] J. Cseh, G. Tímár, ATOMKI Ann. Rep. 2005, 25.

[2] R. K. Gupta, J. Phys. G20 (1994) 1067.

[3] J. Cseh, G. Tímár, J. Phys. A39 (2006) 6979.

1.2 $\mathcal{PT}$-symmetric potentials in higher dimensions

G. Lévai

Quantum mechanical Hamiltonians invariant under the simultaneous action of the $\mathcal{P}$ space and $\mathcal{T}$ time inversion operations possess several unusual features. Despite being non-hermitian, the discrete energy spectrum of these $\mathcal{PT}$-symmetric systems can be partly or completely real. Typically the transition from the fully real energy spectrum to the complex one occurs when the non-hermitian component of the Hamiltonian exceeds a certain critical limit, and it can be interpreted as the spontaneous breakdown of $\mathcal{PT}$ symmetry. The orthogonality of the energy eigenstates and the time-independence of their norm can be guaranteed if the inner product is redefined in a suitable way, $\langle\psi|\phi\rangle_{\mathcal{PT}} \equiv \langle\psi|\mathcal{P}\phi\rangle$, however, the *pseudo*-norm defined this way has indefinite sign. With only a few exceptions the study of $\mathcal{PT}$-symmetric systems has been restricted to one-dimensional non-relativistic problems, in which case $\mathcal{PT}$ symmetry amounts to the requirement $V^*(-x) = V(x)$ imposed on the potential function.

The question whether the unusual features of $\mathcal{PT}$-symmetric systems persist in higher spatial dimensions arises naturally. Since the kinetic term $T = (2m)^{-1}\mathbf{p}^2$ is $\mathcal{PT}$-symmetric, this kind of generalization imposes constraints on the potential function only. Formulating the problem in polar coordinates, the equations $V(\rho,\varphi) = V^*(\rho,\varphi+\pi)$ and $V(r,\theta,\varphi) = V^*(r,\pi-\theta,\varphi+\pi)$ have to hold in $d = 2$ and 3 dimensions. Centrally symmetric potentials are obviously uninteresting, since $\mathcal{PT}$ symmetry allows only *real* $V(\rho)$ or $V(r)$ functions.

The solutions of an arbitrary non-central potential cannot be given analytically in general, however, in some special cases the solution is possible by separating the variables [1]. Substituting $\psi(\rho,\varphi) = \rho^{-1/2}\phi(\rho)\tau(\varphi)$ into the two-dimensional Schrödinger equation one arrives at the equation

$$\phi''\tau + \frac{1}{\rho^2}\phi\tau'' + [\frac{1}{4\rho^2} - V(\rho,\varphi) + E]\phi\tau = 0\ . \quad (1)$$

If $\tau''(\varphi)$ can be expressed as $\tau'' = [K(\varphi) - k]\tau$ such that $V(\rho,\varphi) = V_0(\rho) + \rho^{-2}K(\varphi)$, where $V_0(\rho)$ and k are real, while $K^*(\varphi+\pi) = K(\varphi)$, then an *hermitian* radial Schrödinger equation can be separated as

$$-\phi'' + [V_0(\rho) + (k - \frac{1}{4})\frac{1}{\rho^2}]\phi - E\phi = 0\ . \quad (2)$$

The exact solution of Eq. (2) can be obtained for a few radial potentials in the standard way. As an illustration, let us consider the $\tau(\varphi) = c_\varphi \exp[\mathrm{i}\sin(m\varphi)]$ function, where m is an odd integer. Then $k = m^2/2$ and $V(\rho,\varphi) = V_0(\rho) - \frac{m^2}{\rho^2}\left[\frac{1}{2}\cos(2m\varphi) + \mathrm{i}\sin(m\varphi)\right]$. Although this illustration presents only one particular solution of the problem, it demonstrates some important features of $d = 2$ $\mathcal{PT}$-symmetric systems. It is notable, for example, that the periodicity of the real and imaginary components of the angle-dependent potential term has to be different.

In a more general approach $K(\varphi)$ and k can be chosen a $\mathcal{PT}$-symmetric potential and its *real* energy eigenvalues. Then the differential equation for $\tau(\varphi)$ is interpreted as a Schrödinger equation in itself, only the boundary conditions have to be chosen in a suitable way. The Scarf I potential with unbroken $\mathcal{PT}$ symmetry [2] could be an appropriate choice, for example.

The three-dimensional case can also be discussed in the same way and the conclusions remain similar [1]. Using the generalization of the spherical harmonics $Y_{lm}(\theta,\varphi)$ the separation of an *hermitian* radial Schrödinger equation becomes possible again. The angular and radial differential equations will also be connected by parameters appearing in both sectors. Preliminary results indicate that the spontaneous breakdown of $\mathcal{PT}$ symmetry cannot be implemented easily, furthermore, the sign of the pseudo-norm alternates following a pattern observed for $d = 1$ problems.

[1] G. Lévai, J. Phys. A **40** (2007) F273.

[2] G. Lévai, J. Phys. A **39** (2006) 10161.

1.3 Charged exciton resonances in two and three dimensions

J.Zs. Mezei, A.T. Kruppa and K. Varga

In this work we have extended the study of stability of Coulombic few-particle systems to resonance states [1]. Besides the study of three dimensional systems, we have also investigated the properties of resonance states in two dimensions to study the effect of confinement and model electron-hole systems in semiconductor quantum wells.

The complex scaling method combined with the stochastic variational approach has been used to calculate the position (energy and width) of the resonance states. The use of correlated Gaussian basis combined with the stochastic variational method is proved to be very fruitful for the description of more than three particles, and by rotating the coordinates into the complex plane a (non square integrable) resonant wave function becomes square integrable (L^2) and is hence accessible by basis set expansion.

We will limit our study to the case where two particles have equal masses and charges and the third particle has an opposite charge. The systems in these calculations therefore can be characterized by either $X^+ = (M^+, M^+, m^-)$ or by $X^- = (M^+, m^-, m^-)$, where the masses of the particles satisfy $M \geq m$, so we introduce $\sigma = m/M$ to define the mass ratio between two particles. Excitonic atomic units were used in the calculations.

The position of the resonance for the $X^- = (M^+, m^-, m^-)$ and $X^+ = (M^+, M^+, m_e^-)$ systems as the function of the mass ratio are shown in Figure 1. The n=2 thresholds (both 2D and 3D) are also shown. The position of the resonance E_R in both cases shows a very smooth behavior. The width of the resonance Γ is also smooth as the function of the mass ratio in the case of X^-. In contrast, there are interesting variations in the X^+ case. The oscillation of the width is not caused by the vicinity of the other resonance. The changes may be due to a structural change: a molecule like system is transformed into an atom like system by changing the mass ratio. The calculated lifetimes of the resonances are in the nano- and picosecond region so there is a chance for the experimental determination of these resonances.

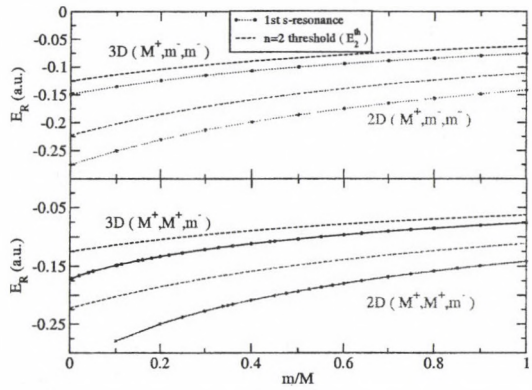

Figure 1. The position (real part of the energy) of the resonance state as the function of the mass ratio for negatively and positively charged trions in 2D and 3D. The resonance energy is given by $E_R - \frac{i}{2}\Gamma$. The second thresholds are also shown both for 2D and 3D systems.

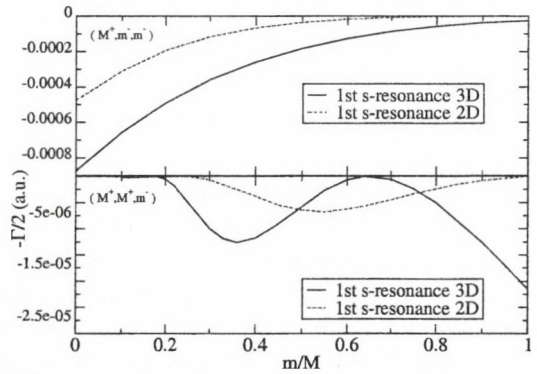

Figure 2. The imaginary part of the energy of the resonance state as the function of the mass ratio for positively and negatively charged trions in 2D and 3D. The resonance energy is given by $E_R - \frac{i}{2}\Gamma$.

[1] J. Zs. Mezei, A. T. Kruppa and K. Varga, submitted to Phys. Rew. A.

1.4 Entangled versus unentangled measurements on two antiparallel spins

T. Vértesi

One of the central problems in quantum information theory is the state discrimination problem: Suppose one is given a single quantum system, which is known to be in one of several possible pure states each having a certain *a priori* probability. Given this *a priori* description, one wishes to carry out a measurement on the system that will yield as much information about the state as possible.

Some time ago Peres and Wootters [1] addressed the intriguing problem, whether there is a difference between collective, as compared to local, measurements on two particles. Technically, in the first case one permits arbitrary quantum operations on both particles, while in the latter case one is restricted to local operations on each particle and classical communication between the two particles. Peres and Wootters [1] showed numerical evidence that even if the two particles are in the same state, collective measurements can do better then local measurements. But among collective measurements it is interesting to consider two mutually exclusive and exhaustive classes: (1) unentangled measurements, those whose outcomes are associated with product states, and (2) entangled measurements, those for which at least one outcome is associated with an entangled state.

Then an interesting question was posed recently by Wootters [2] about the power of these kinds of collective measurements, whether every ensemble of product states could be distinguished just as well by an unentangled measurement as by an entangled measurement. Although it turned out, that a special ensemble of product states can be optimally distinguished by an unentangled measurement [2], the question in general left open.

In Ref. [3] we addressed this question by focusing on the following special state discrimination problem: Given a source which emits a pair of antiparallel spin-1/2 particles polarized along a random space direction the task of the observer is to perform an unentangled measurement on the two spins which provides the maximum gain of information about the polarization direction.

In the study [3] we used a particular form of the information gain, well-defined for a continuous distribution of the signal states and exploited its rotational invariance. Then applying Jensen's inequality and the Lagrange multipliers method enabled us to develop analytically an upper bound to the information gain attainable by an unentangled measurement. Explicitly, we have obtained analytically the upper bound 0.7935 bits and numerically the upper bound 0.557 bits of information gain achieved by the best unentangled measurement, while we have found the lower bound 0.8664 bits for the best entangled measurement.

This result entails that interestingly for the case of antiparallel spins the optimal measurement (which particularly is an entangled one) is more than one and half times more effective than an unentangled measurement, and would give a conclusive answer for Wootters' question [2] demonstrating that not every ensemble of product states can be distinguished optimally by an unentangled measurement.

Acknowledgements

This work was supported by the Grant Öveges of the National Office for Research and Technology.

[1] A. Peres and W.K. Wootters, Phys. Rev. Lett. **66**, 1119 (1991).

[2] W.K. Wootters, Int. J. Quant. Inf. **4**, 219 (2006).

[3] T. Vértesi, arXiv:quant-ph/0611201, submitted for publication.

2.1 Study of beam induced heating effects in ^{3}He gas

Z. Elekes, Zs. Fülöp, Gy. Gyürky, E. Somorjai for the LUNA Collaboration

Experiments aiming at low cross section determination require high beam intensity, excellent target stability and low background conditions. Windowless gas target systems proved to match these requirements.

When an intense ion beam passes through an extended gas target, however, a reduction of the gas density in the interaction zone occurs as a consequence of heat transfer from the beam. Therefore the bulk gas pressure measured by sensors may not be a relevant quantity for target thickness determination. This effect has been investigated for proton beam hitting nitrogen gas target and is expected to be of the order of 10 % if the dissipated power is of the order of 20 mW/mm [1]. For the ^{14}N(p,γ)^{15}O reaction – studied recently by the LUNA collaboration – the effective density of an extended gas target under bombardment could be determined via the investigation of the location of a well defined resonance [2]. However, this method cannot be applied for the ongoing LUNA project, the ^{3}He(α,γ)^{7}Be reaction study [3], where no resonance is present in the studied energy region.

The present work reports on an effort to determine the beam heating correction in ^{3}He gas and consequently reduce the uncertainty due to beam induced loss in target density below 2 %, in order to reach a total uncertainty of 4 % in the cross section of the ^{3}He(α,γ)^{7}Be reaction.

The beam heating investigation was based on the detection of α projectiles elastically scattered on ^{3}He gas target nuclei. Here, the measured scattering rate is proportional to the well-known Rutherford cross-section as well as to the convolution of the beam current and target density.

Because of the very high beam intensity a second thin scattering foil made of carbon was introduced between the particle detector and the collimator facing the gas target. The two consecutive scattering processes reduced the counting rate in the detector drastically. Measurements were performed at different collimator positions along the gas target chamber with beams of different energies and intensities resulting in different dissipated powers. As an example the result for one position is shown in Fig. 1.

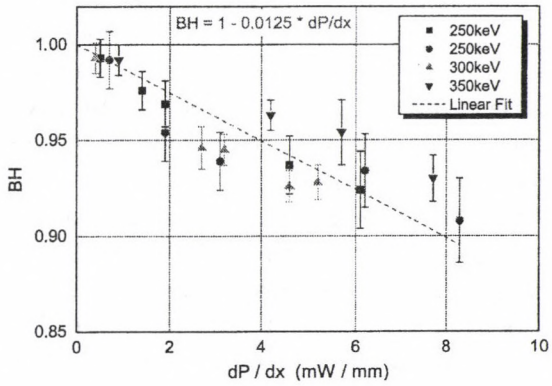

Figure 1. Beam heating effect (relative decrease of target density) as a function of the dissipated power per unit length.

The determined slopes of the beam heating effect factor for each investigated positions have been averaged resulting in a slope [4] that is approximately a factor 2 higher than the one obtained by [1] with nitrogen gas target and proton beam.

The ongoing ^{3}He(α,γ)^{7}Be LUNA experiment can use the obtained effective target density with an uncertainty between 1.3 % and 1.6 %, matching the desired precision.

[1] J. Görres et al., Nucl. Instr. Meth. 177 (1980) 295.

[2] A. Lemut, LUNA Coll., Phys. Lett. B634 (2006) 483.

[3] D. Bemmerer, LUNA Coll., Phys. Rev. Lett. 97 (2006) 122502.

[4] M. Marta, LUNA Coll., Nucl. Instr. Meth. A569 (2006) 727.

2.2 Low energy cross section of ^{3}He$(\alpha,\gamma)^7$Be measured with activation

Gy. Gyürky, Z. Elekes, Zs. Fülöp, E. Somorjai for the LUNA collaboration

The ^{3}He$(\alpha,\gamma)^7$Be reaction plays an important role both in primordial nucleosynthesis of ^{7}Li and in stellar hydrogen burning. The primordial abundance of ^{7}Li is an important test of big bang nucleosynthesis model calculations and presently the models are not able to reproduce the observed ^{7}Li abundance. Additionally, the reaction rate of ^{3}He$(\alpha,\gamma)^7$Be is the major nuclear physics source of uncertainty in the predicted fluxes of the high energy ^{7}Be and ^{8}B neutrinos from the sun. Therefore the precise measurement of the ^{3}He$(\alpha,\gamma)^7$Be cross section in (or close to) the relevant energy regions is of great importance.

The LUNA collaboration has launched an experimental program on the ^{3}He$(\alpha,\gamma)^7$Be reaction in Italy's Gran Sasso underground laboratory to measure high precision cross section of the reaction by detecting both the prompt γ-radiation from the reaction (on-line method) and the decay of the produced ^{7}Be (activation).

In the first phase of the experiment the cross section has been measured with the activation method. The LUNA 400 kV accelerator provided an α-beam between 220 and 400 keV with a beam intensity of typically 200 μA. The beam current has been measured with a calibrated beam calorimeter. The ^{3}He$(\alpha,\gamma)^7$Be reactions took place in a differentially pumped windowless gas target filled with 0.7 mbar enriched ^{3}He. The reduction of the gas target pressure along the beam line (the beam heating effect) as well as the impurities in the target gas has been measured with a movable particle detector built in the chamber detecting the elastically scattered ^{4}He.

The produced ^{7}Be has been collected onto a detachable copper catcher that served also for the beam stop. The ^{7}Be activity has been measured subsequently on two HPGe detectors. The absolute efficiency of the detectors has been measured with ^{7}Be calibration sources which were prepared in ATOMKI and whose activity was measured both in ATOMKI and in Gran Sasso. Owing to the ultra low background detectors, the proper shielding and the strong cosmic ray suppression of the underground laboratory, activities as low as 25 mBq has been successfully measured with high precision.

The cross section has been measured with 4% total uncertainty in the energy range between $E_{c.m.} = 93$ and 169 keV, much lower than ever reached before with activation method. Fig. 1. shows the results in the form of astrophysical S factor together with the results from previous experiments and an R-matrix calculation fitted to the present data. The measured energy region is directly relevant for primordial nucleosynthesis and the high precision of the data puts a strong constraint to the extrapolation down to solar energies. Therefore the nuclear physics uncertainty both in primordial nucleosynthesis models and solar neutrino flux calculations is strongly reduced [1,2].

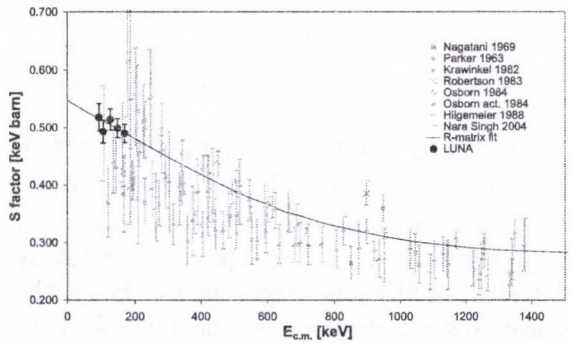

Figure 1. Astrophysical S factor of the ^{3}He$(\alpha,\gamma)^7$Be reaction. See text for details.

[1] D. Bemmerer *et al.* (LUNA Collaboration), Phys. Rev. Lett. 97 (2006) 12502.

[2] Gy. Gyürky *et al.* (LUNA Collaboration), Phys. Rev. C 75 (2007) 035805.

2.3 In-beam γ-ray spectroscopy of the neutron rich nucleus ^{21}N

Zs. Dombrádi, D. Sohler, F. Azaiez[a)], B.A. Brown[b)], M.G. Saint-Laurent[c)], O. Sorlin[c)], M. Stanoiu[a,d)], Y. Penionskhevitch[e)], N. L. Achouri[f)], J. C. Angélique[f)], M. Belleguic[a)], C. Borcea[g)], C. Bourgeois[a)], J.M. Daugas[c)], F. De Oliveira-Santos[c)], Z. Dlouhy[h)], C. Donzaud[a)], J. Duprat[a)], Z. Elekes, S. Grévy[c)], D. Guillemaud-Mueller[a)], F. Ibrahim[a)], S. Leenhardt[a)], M. Lewitowicz[c)], M.J. Lopez-Jimenez[c)], S.M. Lukyanov[e)], W. Mittig[c)], J. Mrazek[h)], F. Negoita[g)], Zs. Podolyak[i)], M.G. Porquet[j)], F. Pougheon[a)], P. Roussel-Chomaz[c)], H. Savajols[c)], Y. Sobolev[e)], C. Stodel[c)], J. Timár

To reveal the disappearance of the N=14 subshell closure in nitrogen isotopes the structure of ^{21}N was investigated by means of the in-beam γ-ray spectroscopic technique using fragmentation reactions of radioactive beam at GANIL, France.

In the experiment after the fragmentation of a primary beam of ^{36}S on a C target, the produced nuclei were selected by the ALPHA spectrometer. A secondary target composed of a plastic scintillator sandwiched by two C foils was palced at the dispersive focus of the SPEG spectrometer. The plastic scintillator part of the 'active' target was used to select the incoming nuclei through energy loss and time of flight measurements. The fragments induced in the secondary reactions were identified also by standard ΔE-TOF method through the SPEG spectrograph which was optimized for A/Z=3. The γ rays emitted by the fragments in flight were observed by 74 BaF_2 detectors situated symmetrically above and below the target. To decrease the background caused by the scattered γ rays we used the BaF_2 array in add-back mode. The relatively high efficiency of this array made possible to observe $\gamma\gamma$ coincidences. The Doppler-shift caused by the large fragment velocity (v/c=0.34) was taken into account in creation of the γ-ray spectra.

In the BaF_2 spectrum of ^{21}N shown in Fig. 1. a wider peak dominates at about 1180 keV. Determining the energy dependence of the peak width from the systematics of single peaks of other nuclei observed in the present experiment, this wide peak could be resolved into two γ rays of 1159 and 1228 keV energy. In addition, we have a wide bump ranging from 1600 to 2800 keV. This bump can be fitted by three weaker γ rays of 1790, 2142 and 2438 keV. Putting a wide gate on the 1159+1228 keV doublet, all the γ rays assigned to this nucleus are enhanced relative to the background, even the small peak at 884 keV becomes significant. Putting a narrow gate on the peaks in the wider bump, we can see that the 1790 keV transition is in coincidence with both the 1159 and 1228 keV γ rays, while the higher energy transitions see only the 1159 keV transition in the coincidence spectra. The $\gamma\gamma$-coincidence information together with the γ-ray energies and intensities obtained was used in the construction of the level scheme of this nucleus.

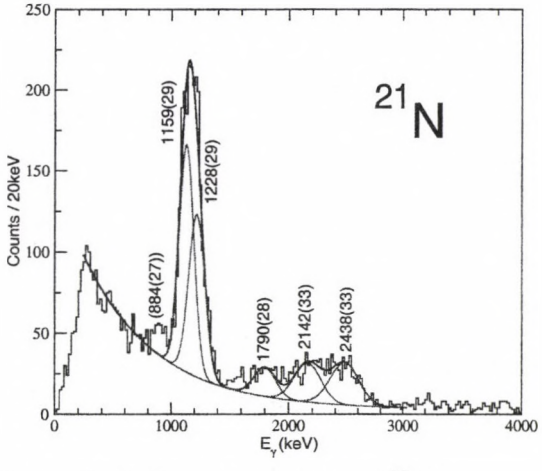

Figure 1. BaF_2 γ-ray spectrum of ^{21}N.

b) IN2P3-CNRS, Orsay, France
b) NSCL, MSU, East Lansing, USA
c) GANIL, Caen, France
d) GSI, Darmstadt, Germany
e) FLNR, JINR, Dubna, Russia
f) LPC, Caen, France
g) IFIN-HH, Bucharest-Magulere, Romania
h) NPI, Rez, Czech Republic
i) University of Surrey, Guildford, UK
j) CSNSM, IN2P3-CNRS, Orsay, France

2.4 Vanishing N=20 shell gap: study of excited states in ^{27,28}Ne

Z. Elekes, Zs. Dombrádi, A. Saito[a], N. Aoi[b], H. Baba[a], K. Demichi[a], Zs. Fülöp, J. Gibelin[c], T. Gomi[a], H. Hasegawa[a], N. Imai[d], M. Ishihara[b], H. Iwasaki[d], S. Kanno[a], S. Kawai[a], T. Kishida[b], T. Kubo[b], K. Kurita[a], Y.U. Matsuyama[a], S. Michimasa[d], T. Minemura[b], T. Motobayashi[b], M. Notani[d], T. Ohnishi[d], H.J. Ong[d], S. Ota[e], A. Ozawa[b], H.K. Sakai[a], H. Sakurai[d], S. Shimoura[d], E. Takeshita[a], S. Takeuchi[b], M. Tamaki[d], Y. Togano[a], K. Yamada[a], Y. Yanagisawa[b], K. Yoneda[b]

In order to test modern shell model calculations excited states of neutron rich isotopes ^{27,28}Ne have been studied. In the present experiment, a 94 A·MeV energy primary beam of ^{40}Ar with 60 pnA intensity hit a ^{181}Ta production target of 0.5 cm thickness. The reaction products were momentum- and mass–analyzed by the RIPS fragment separator. The secondary beam included neutron-rich ^{24}O, ^{25,26,27}F, ^{27,28,29,30}Ne and ^{29,30,31,32}Na nuclei. The RIPS was operated at 6% momentum acceptance. The total intensity was approximately 100 cps. The identification of incident beam species was performed by energy loss, time-of-flight and magnetic rigidity ($B\rho$). The secondary beam was transmitted to a liquid hydrogen target at the final focus of RIPS. The average areal density of the hydrogen was 210 mg/cm^2. The position of the incident particles was determined by two PPACs placed at F3 upstream of the target. The scattered particles were detected and identified by a PPAC and a silicon telescope. The telescope consisted of three layers with thicknesses of 0.5, 0.5 and 1 mm. The Z identification was performed by TOF-energy loss method. Based on ΔE-E information, isotope separation was carried out among the different neon isotopes. The DALI2 setup, including 146 NaI(Tl) scintillator detectors, surrounded the target to detect de–exciting γ rays emitted by the inelastically scattered nuclei. In Figure 1 the resulting γ ray spectra can be seen. Determinig the cross sections in ^{28}Ne, and using the previously measured B(E2), the neutron and proton transition matrix elements have been deduced via DWBA analysis. The neutron transition probability was found to be more or less enhanced compared to the pure *sd* shell model calculations depending on the value of the effective charges. The number of bound excited states observed in ^{27}Ne by knocking out a neutron from ^{28}Ne is larger than predicted by the *sd* shell model. The presence of a low-lying extra state intruding from the upper *fp* shell can be considered as an indication of a strongly reduced N=20 shell gap.

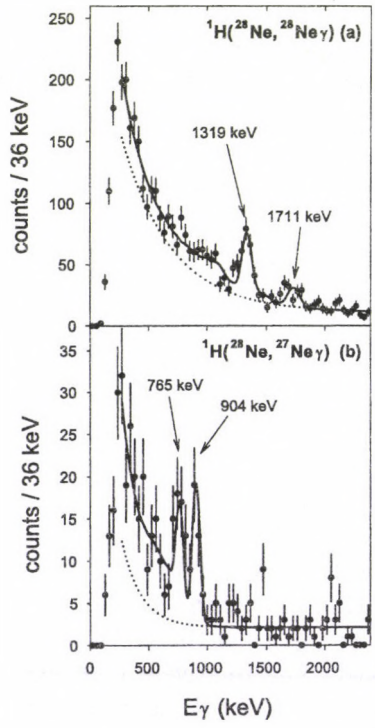

Figure 1. Doppler-corrected spectra of γ rays emerging from ^{1}H(^{28}Ne,^{28}Ne) (a) and ^{1}H(^{28}Ne,^{27}Ne) (b) reactions. The solid line is the final fit including the spectrum curves from GEANT4 simulation and additional smooth polynomial backgrounds plotted as separate dotted lines for each nucleus.

a) Rikkyo University, Tokyo, Japan
b) RIKEN, Wako-shi, Japan
c) IPN, Orsay, France
d) University of Tokyo, Tokyo, Japan
e) Kyoto University, Kyoto, Japan

2.5 Proton inelastic scattering studies at the borders of the "island of inversion": The ^{30,31}Na and ^{33,34}Mg case

Z. Elekes, Zs. Dombrádi, A. Saito[a], N. Aoi[b], H. Baba[a], K. Demichi[a], Zs. Fülöp, J. Gibelin[c], T. Gomi[a], H. Hasegawa[a], N. Imai[d], M. Ishihara[b], H. Iwasaki[d], S. Kanno[a], S. Kawai[a], T. Kishida[b], T. Kubo[b], K. Kurita[a], Y.U. Matsuyama[a], S. Michimasa[d], T. Minemura[b], T. Motobayashi[b], M. Notani[d], T. Ohnishi[d], H.J. Ong[d], S. Ota[e], A. Ozawa[b], H.K. Sakai[a], H. Sakurai[d], S. Shimoura[d], E. Takeshita[a], S. Takeuchi[b], M. Tamaki[d], Y. Togano[a], K. Yamada[a], Y. Yanagisawa[b], K. Yoneda[b]

In order to explore the borders of island of inversion we investigated the nuclei ^{30,31}Na and ^{33,34}Mg by inelastic proton scattering in inverse kinematics. A ^{40}Ar primary beam of 94 MeV/nucleon energy with 60 pnA intensity was transported to a ^{181}Ta production target of 0.5 mm thickness. The RIPS fragment separator analyzed the momentum and mass of the reaction products. The ^{30,31}Na and ^{33,34}Mg beams were produced in two individual runs with different settings of Bρ values. In the first run of ^{30,31}Na, the secondary beam included neutron–rich O, F, Ne and Na nuclei with $A/Z \approx 3$ while mainly Mg and Al isotopes were mixed in the second run of ^{33,34}Mg. The total intensity was about 100 particle/s (pps) for both runs, while the ^{30,31}Na/^{33,34}Mg intensities reached 8, 6, 3 and 2 pps, respectively, on average. The identification of incident beam species was performed on an event–by–event basis by means of energy loss, time–of–flight (TOF) and magnetic rigidity ($B\rho$). The secondary beam hit a liquid hydrogen target. The mean energy of the isotopes in the target was around 50 MeV/nucleon. Two PPACs at F3 upstream of the target monitored the position of the incident particles. The reaction products and scattered particles were detected and identified by a PPAC and a silicon telescope. The Z identification was performed by TOF–energy loss method where the TOF was taken between the PPACs upstream and downstream of the secondary target. The isotope separation was done by use of the ΔE–E method. The de–exciting γ rays emitted by the inelastically scattered nuclei were detected by the DALI2 setup consisting of 146 NaI(Tl) scintillators surrounding the target (see, e.g., Figure 1). To determine the cross sections of the production of the γ rays in proton inelastic scattering the peak positions determined were fed into the detector simulation software GEANT4 and the resultant response curves plus smooth polynomial backgrounds were used to analyze the experimental spectra. From a distorted wave analysis of the cross sections, we derived "matter" deformation parameters (β_M), which are consistent with the charge deformations determined from Coulomb excitation experiments. Based on the "matter" and charge deformation parameters, the neutron deformation parameters could also be extracted. The results show that all these nuclei are largely deformed; the deformation of the proton and neutron distributions are similar and cannot be distinguished at the present experimental uncertainties.

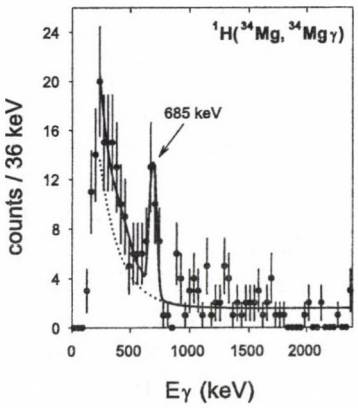

Figure 1. Doppler–corrected spectra of γ rays emerging from ^{1}H(^{34}Mg,^{34}Mg) reaction. The solid line is the final fit including the spectrum curves from GEANT4 simulation and additional smooth polynomial backgrounds plotted as separate dotted lines.

a) Rikkyo University, Tokyo, Japan
b) RIKEN, Wako-shi, Japan
c) IPN, Orsay, France
d) University of Tokyo, Tokyo, Japan
e) Kyoto University, Kyoto, Japan

2.6 Nuclear structure at the border of island of inversion: The case of ^{33}Al

D. Sohler, Zs. Dombrádi, F. Azaiez[a], M. Belleguic[a], M. J. Lopez-Jimenez[b], M. G. Saint-Laurent[b], O. Sorlin[b], N.L. Achouri[c], J.C. Angelique[c], C. Borcea[d], C. Bourgeois[a], J.M. Daugas[b], F. De Oliveira-Santos[b], Z. Dlouhy[e], C. Donzaud[a], J. Duprat[a], S. Grevy[b], D. Guillemaud-Mueller[a], S. Leenhardt[a], M. Lewitowicz[b], S.M. Lukyanov[f], W. Mittig[b], Yu.-E. Penionzhkevich[f], M.G. Porquet[g], F. Pougheon[a], P. Roussel-Chomaz[b], H. Savajols[b], Y. Sobolev[f], C. Stodel[b], M.Stanoiu[a,h], J. Timár

An island of inversion — a small region of the nuclear chart where the order of intruder states arising from the pf shell is lowered below the normal ones from the sd shell — was observed around ^{31}Na. ^{33}Al is predicted to lie at the border of this region, we searched for the effect of intruder states on its structure by in-beam γ-spectroscopic method.

In the experiment carried out at GANIL, France a ^{36}S beam was fragmented on a ^{9}Be target. The emerging fragments were selected and identified by the SPEG magnetic spectrometer by a standard energy-loss-time-of-flight method. The total energy was obtained by a plastic scintillator, while the ΔE and the Bρ information of the fragments were measured in an ionization and two drift chambers, respectively. The time of flight of the fragments was taken from the timing signals in the scintillator. The SPEG was optimized to A/Z=$\frac{8}{3}$ mass to charge ratio. Alltogether 43 different isotopes were identified and about $7.5{\cdot}10^5$ ^{33}Al nuclei were observed.

The γ rays emitted in flight by the excited fragments were observed by 4 Ge detectors and an array of 74 BaF_2 crystals mounted symmetrically above and below the target. The BaF_2 array was used in addback mode by summing up the energies of two γ rays detected in coincidence in adjacent detectors. Due to the relatively high efficiency of the BaF_2 array of about 20% at 1.3 MeV, for the stronger transitions $\gamma\gamma$-coincidence techniques could be exploited.

The spectrum obtained by the Ge detectors for ^{33}Al is shown in Fig. 1. Three stronger peaks at 1644, 1849 and 2131 keV energies are clearly visible. At higher energies two weaker lines appear at 2526 and 2774 keV with 2.0σ and 3.1σ confidence levels, respectively. We assign all these γ rays to ^{33}Al. Using the $\gamma\gamma$-coincidence data a level scheme of ^{33}Al has been constructed, where the energy of the one phonon states is strongly depressed relative to the sd shell prediction. This lowering of the states can be cosidered as a sign for mixing of the normal and intruder neutron configurations in the excitations of the even-even core of the odd proton nucleus ^{33}Al.

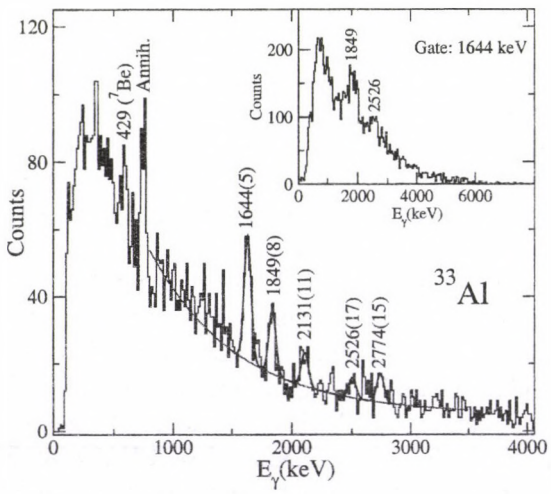

Figure 1. Ge γ–ray spectrum of ^{33}Al. In the inset BaF_2 coincidence spectrum gated by the 1644 keV transition is shown.

a) IPN, IN2P3-CNRS, Orsay, France

b) GANIL, Caen, France

c) Lab. de Phys. Corpusculaire, Caen, France

d) IFIN-HH, Bucarest, Romania

e) Nucl. Phys. Inst., Rez, Czech Republic

f) FLNR, JINR, Dubna, Russia

g) CSNSM, IN2P3-CNRS, Orsay, France

h) GSI, Darmstadt, Germany

2.7 Weakening of the N=28 shell closure at Z=15

Zs. Dombrádi, D. Sohler, B. Bastin[b], S. Grévy[a], O. Sorlin[a], N. L. Achouri[b], J. C. Angélique[b], F. Azaiez[c], D. Baiborodin[d], R. Borcea[e], C. Bourgeois[c], A. Buta[e] A. Bürger[f,g], R. Chapman[h], J. C. Dalouzy[a], Z. Dlouhy[d], A. Drouard[f], Z. Elekes, S. Franchoo[c], S. Iacob[e], B. Laurent[b], M. Lazar[e], X. Liang[h], E. Lienard[b], J. Mrazek[d], L. Nalpas[f], F. Negoita[e], N. A. Orr[b], Y. Penionskhevitch[i], Zs. Podolyak[j], F. Pougheon[c], P. Roussel-Chomaz[a], M. G. Saint-Laurent[a], M. Stanoiu[c,k], I. Stefan[a], F. Nowacki[l], A. Poves[m]

The strength of the N=28 shell closure was studied by in-beam γ-ray spectroscopy of ^{41}P and ^{43}P nuclei.

In the experiment performed at GANIL, France a stabil ^{48}Ca beam impinged onto a ^{12}C target. The fragments produced were separated by the SISSI device and identified through their energy loss (ΔE) and time-of-flight (TOF) measured at the ALPHA spectrometer which was optimised for ^{44}S. The cocktail beam obtained was further fragmented on a secondary ^{9}Be target placed at the entrance of the SPEG spectrometer, tuned to A/Z=3 mass to charge ratio correspoding to ^{42}Si. The secondary reaction products were identified by their magnetic rigidity, ΔE determined in an ionisation chamber, as well as by their TOF and residual energies obtained from a plastic scintillator at the focal plane of SPEG. To detect γ rays arising from the secondary fragments an array of 74 BaF_2 crystals was arranged in two hemispheres above and below the Be target. The γ-ray spectra were obtained by gating event-by-event on the incoming beam nuclei and on the secondary reaction products. The γ rays were corrected for Doppler shifts due to the in-flight emission by the fragments at large velocity (v/c$\approx$ 0.3).

In the γ-ray spectrum of ^{41}P a strong low energy transition at 172 keV is visible together with several slightly overlapping peaks at 420, 964, 1146 and 1408 keV. The 964 and the 1408 keV transitions are in coincidence with the 172 keV γ ray, while the 964 keV transition sees the 420 keV γ line in coincidence, too, resulting in the level scheme presented in Fig. 1. In ^{43}P, in addition to the previously reported low energy transition at 186 keV, a doublet of weak γ lines is observed at 789 and 918 keV. Both transitions are in coincidence with the 186 keV one and are placed to feed it as it is shown in Fig. 1. The obtained level schemes together with the low energy of the 2_1^+ state in ^{42}Si provide evidence for the weakening of the N=28 shell closure with decreasing proton number.

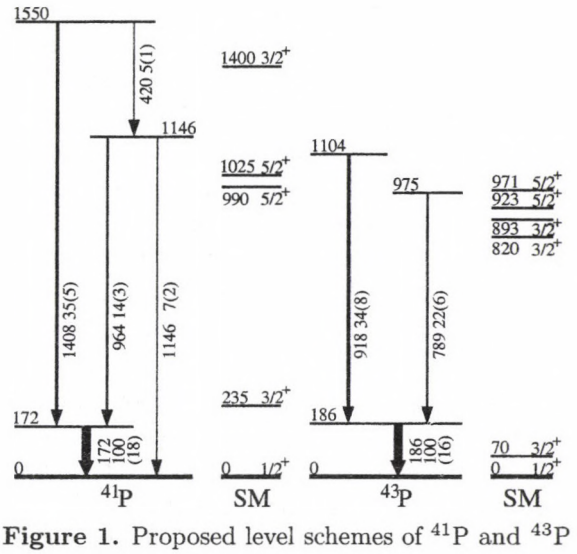

Figure 1. Proposed level schemes of ^{41}P and ^{43}P compared to shell model calculations.

a) GANIL, Caen, France
b) LPC, Caen, France
c) IN2P3-CNRS, Orsay, France
d) NPI, Rez, Czech Republic
e) IFIN-HH, Bucharest-Magulere, Romania
f) DAPNIA/SPhN, CEA Saclay France
g) Universität Bonn, Germany
h) University of Paisley, Scotland, UK
i) FLNR, JINR, Dubna, Russia
j) University of Surrey, Guildford, UK
k) GSI, Darmstadt, Germany
l) IreS, Strasbourg, France
m) Universidad Autónoma de Madrid, Spain

2.8 Study of proton induced reaction cross sections on Germanium isotopes for the astrophysical p-process

G.G. Kiss, Gy. Gyürky, Z. Elekes, Zs. Fülöp, E. Somorjai, M. Wiescher[a], T. Rauscher[b]

The stable proton-rich nuclei with charge number Z≥34 are called p-nuclei [1]. It is generally accepted that the main stellar mechanism synthesizing these nuclei — the so-called p-process — is initiated by subsequent (γ,n) photodisintegration reactions on preexisting more neutron-rich seed nuclei. As the neutron separation energy increases along this path towards more neutron deficient isotopes, (γ,p) and (γ,α) reactions become stronger and process the material towards lower masses [2-4]. Recently it has been stated that (p,n) reactions can also give contribution to the reaction flow [4]. Despite considerable experimental and theoretical efforts in recent years, there are still open questions about the nature of the p-process and the synthesis of the p-isotopes.

As a continuation of our p-process studies [5 and references therein], the proton-induced cross sections of the ^{70}Ge(p,γ)^{71}As and ^{76}Ge(p,n)^{76}As reactions have been measured recently at ATOMKI using the activation method.

The targets were made by evaporating natural metallic Ge on thin, high purity Al foils. Natural targets have the advantage that both reactions can be studied simultaneously in a single activation procedure. The irradiations were carried out at the Van de Graaff and cyclotron accelerators of ATOMKI. The energy range from E_p=1.6 to 4.4 MeV was covered with 400 keV steps. A surface barrier detector was used to monitor the target stability during the irradiation by detecting the backscattered particles. The γ radiation following the β decay of the produced As isotopes was measured with a 40% relative efficiency HPGe detector. The γ spectra were taken for 10 h and stored regularly in order to follow the decay of the different reaction products.

Figure 1. shows the preliminary results and the comparison with the Hauser-Feshbach statistical model calculation, using the NON-SMOKER code.

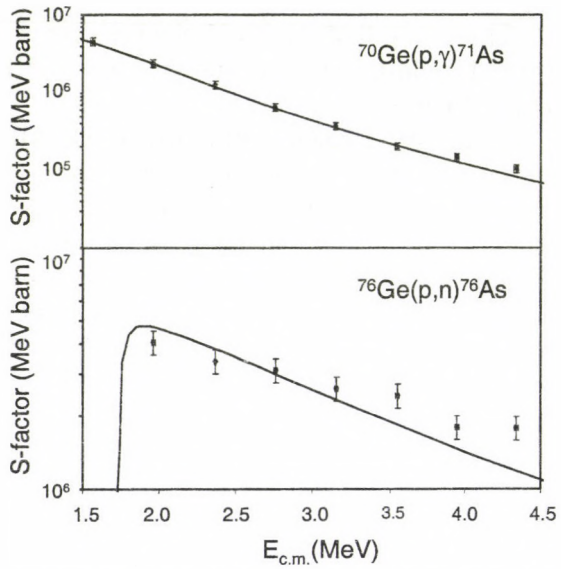

Figure 1. Measured and calculated S-factor of the investigated reactions. The solid line represents the predictions of the Hauser-Feshbach model calculation using the NON-SMOKER code.

The agreement between the statistical model predictions and the experimental data is good in the case of the (p,γ) reaction, while in the case of the (p,n) reaction the slope of the calculated S-factor curve differs slightly from the measured one.

a) University of Notre Dame, Notre Dame, Indiana 46556, USA

b) Universität Basel, CH-4056 Basel, Switzerland

[1] S. E. Woosley and W. H. Howard, Astrophys. J. Suppl. 36, (1978) 285.

[2] M. Arnould, S. Goriely, Phys. Rep. 384 (2003) 1.

[3] T. Rauscher, Phys. Rev. C73 (2006) 015804.

[4] W. Rapp *et al.*, Astrophys. J. 653 (2006) 474.

[5] Gy. Gyürky *et al.*, Phys. Rev. C74 (2006) 015805.

2.9 High-spin structure of ^{105}Ag: search for chiral doublet bands

J. Timár, T. Koike[a,b], N. Pietralla[a,c], G. Rainovski[a,d], D. Sohler, T. Ahn[a,c], G. Berek, A. Costin[a,c], K. Dusling[a], T.C. Li[a], E.S. Paul[e], K. Starosta[f], C. Vaman[a,f]

Nuclear chirality is one of the most intriguing questions of the contemporary high-spin nuclear structure studies. Chiral candidate doublet structures have been observed mostly in two islands of the nuclear chart: around ^{134}Pr and around ^{104}Rh . In this second chiral island the Rh isotopes are rather well studied, however, besides these nuclei there are only the ^{106}Ag and ^{100}Tc where chiral doubling have been documented.

In this region the chiral rotation is expected for the $\pi g_{9/2}\nu h_{11/2}$ configuration in the odd-odd nuclei and for the $\pi g_{9/2}\nu(h_{11/2})^2$ configuration in the odd-mass nuclei. Jerrestam et al. [1] studied the high-spin bands in the ^{105,106,107}Ag nuclei and reported intensive side bands to the above configurations in ^{106}Ag and ^{107}Ag, respectively, however they have not found the corresponding side band in ^{105}Ag. The ^{106}Ag case was reinvestigated recently by Joshi et al. [2] and reported as chiral rotation. The lack of the side band in ^{105}Ag is quite unexpected if we assume similarity with the behaviour of the side bands in the Rh isotope chain.

To clarify if this difference really exists between the Ag and Rh isotopes, and to search for chirality in ^{105}Ag we studied the high-spin structure of the ^{105}Ag nucleus using the ^{100}Mo(^{10}B,5n)^{105}Ag reaction. The beam was provided by the Stony Brook tandem injected superconducting LINAC accelerator. The emitted γ-rays were detected by six Compton suppressed HPGe detectors and a 14 element BGO multiplicity filter. Approximately 10^8 γ-γ coincidence events were collected. The level scheme of ^{105}Ag has been significantly extended. New bands were found and the placement of the yrast $\pi g_{9/2}\nu(h_{11/2})^2$ band was corrected. Experimental Routhians and aligned angular momenta, as well as B(M1)/B(E2) ratios were derived from the data and compared with predictions of total routhian surface calculations, as well as results of the geometrical model of Dönau and Frauendorf, respectively. On the basis of these comparisons configurations were assigned to the observed bands.

No side band to the yrast $\pi g_{9/2}\nu(h_{11/2})^2$ band could be found in the present experiment. If the side-bands in ^{106}Rh and ^{107}Ag are chiral bands, the present results show that the border of the chiral region at the lighter-mass side of the Ag isotopes is very sharp contrary to that of the Rh isotop chain and the isotope or isotone chains in the mass 130 region. It has been shown recently [3] that the energy difference pattern of the chiral doublet bands in the Rh isotopes depends mainly on the properties of the nuclear core. If this is true also for the similar doublet bands around Rh then the present results may indicate that the triaxiality of the nuclear core drops very abruptly from ^{106}Ag to ^{105}Ag.

Acknowledgements

This work was supported in part by the Hungarian Scientific Research Fund, OTKA (contract numbers T046901).

a) Department of Physics and Astronomy, SUNY, Stony Brook, New York, 11794-3800, USA

b) Graduate School of Science, Tohoku University, Sendai, 980-8578, Japan

c) Institut für Kernphysik, Technische Universität Darmstadt, D-64289 Darmstadt, Germany

d) Faculty of Physics, St. Kliment Ohridski University of Sofia, 1164 Sofia, Bulgaria

e) Oliver Lodge Laboratory, Department of Physics, University of Liverpool, Liverpool L69 7ZE, UK

f) NSCL, Cyclotron Laboratory, Michigan State University, East Lansing, MI 48824-1321, USA

[1] Dan Jerrestam et al., Nucl.Phys. **A577**, 786 (1994); Dan Jerrestam et al., Nucl.Phys. **A579**, 256 (1994).

[2] P.Joshi et al., J.Phys. **G31**, S1895 (2005).

[3] J. Timár et al., Phys. Rev. C **73**, 011301(R) (2006).

2.10 Low energy elastic ^{106}Cd(α,α)^{106}Cd scattering for the astrophysical p-process

G.G. Kiss, Gy. Gyürky, Zs. Fülöp, E. Somorjai, Z. Máté,
D. Galaviz[a,b], *K. Sonnabend*[b], *A. Kretschmer*[b], *A. Zilges*[b]

The stable proton-rich nuclei with charge number Z≥34 are called p-nuclei [1]. Despite considerable experimental and theoretical efforts in recent years, there are still open questions about the synthesis of the p-nuclei (p-process).

Stellar abundance calculations for the p-process are involving more than 2000 nuclei in a network that requires more than 20000 reaction rates. Almost none of these reaction rates have been measured and the calculations rely completely on the statistical model. In the case of reactions involving α-particles, one of the input parameters in statistical model calculations to determine the necessary reaction rates is the alpha-nucleus optical potential. However, different global α-nucleus optical potentials predict largely different optical model parameters at astrophysically relevant energies.

Alpha-nucleus optical model parameters can be derived from elastic scattering experiments. In recent years, alpha-nucleus potential parameters of ^{144}Sm, ^{92}Mo, ^{112,114}Sn and ^{89}Y have been experimentally derived at ATOMKI with the cyclotron accelerator [See Ref. 2. and references therein]. As a continuation of our study a new experiment on ^{106}Cd was performed.

The angular distributions were measured at laboratory energies of 15.546, 17.008 and 18.897 MeV, above and below the Coulomb barrier. The target was produced by evaporating enriched metallic Cadmium on thin Carbon foil. The target thickness was about 200μg/cm^2. The target was placed in the centre of the scattering chamber, and spectra were taken (see Fig. 1.) between $20° \leq \vartheta_{LAB} \leq 170°$ in 1°-2° steps. The experimental data were normalised to the Rutherford cross section.

Local optical potential parameters have been derived from fitting the angular distribution. For the real part of the optical potential Double Folding potential and for the imaginary part a combination of surface and volume Woods-Saxon potentials were used. The optical model analysis is still in progress, comparison with predictions of different global optical potential sets are necessary. The comparison of the experimental cross section of the ^{106}Cd(α,γ)^{110}Sn reaction [3] with the predictions using different global potential parameters as well as our local potential parameters is in progress.

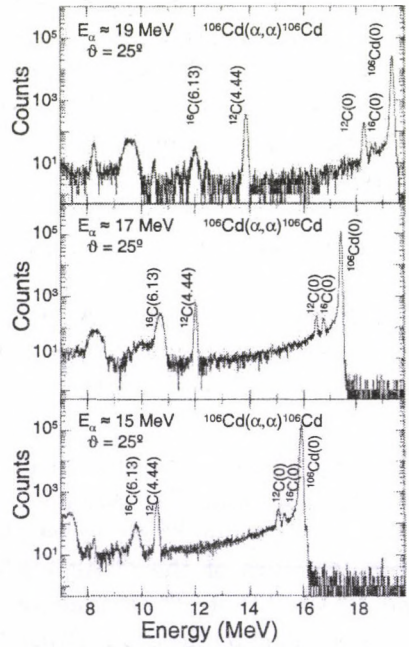

Figure 1. Measured spectra from α-scattering on ^{106}Cd at different energies.

a) Instituto de Estructura de la Materia, 28006 Madrid, Spain

b) Technische Universität Darmstadt, D-64289 Darmstadt, Germany

[1] S.E. Woosley and W.H. Howard, Astrophys. J. Suppl. 36, (1978) 285.

[2] G.G. Kiss et al., Eur. Phys. J. A27 (2006) 197.

[3] Gy. Gyürky et al., Phys. Rev. C74 (2006), 025805

2.11 Cross section of ^{112}Sn(α,γ) in the p-process energy range

N. Özkan[a)], G. Efe[a)], R.T. Güray[a)], A. Palumbo[b)], J. Görres[b)], H.Y. Lee[b)], L.O. Lamm[b)], W. Rapp[b)], E. Stech[b)], M. Wiescher[b)], Gy. Gyürky, Zs. Fülöp, E. Somorjai

Astrophysical p-process studies are based mostly on Hauser-Feshbach statistical models to predict the reaction rates. Although the (p,γ) measurements generally agree with the statistical model predictions within less than a factor of two, (α,γ) measurements show considerable deviation compared to their model predictions [1]. It is, therefore, crucial to investigate the α-induced reaction cross sections experimentally in order to test the reliability of the statistical model predictions. For the recent ^{106}Cd [2] measurements, the (α,γ) results are lower while the (α,p) results are higher than the predictions. For the previously measured two (α,γ) data points on ^{112}Sn [3], only the higher energy value is in good agreement. The measurement of ^{112}Sn$(\alpha,\gamma)^{116}$Te is very important since different optical potentials used in the calculations result in different S-factor predictions [4].

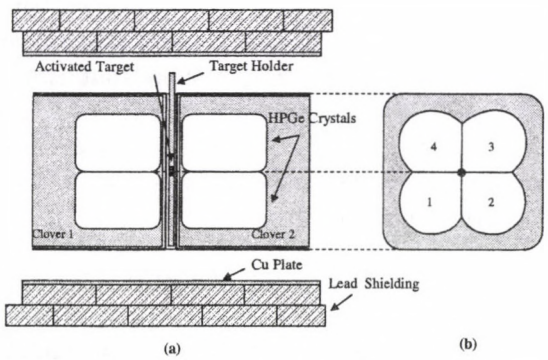

Figure 1. The scheme of the off-line setup to measure the induced γ-ray-activity. (a) Counting area surrounded by Pb and Cu shields. (b) Target position viewed from the front window of the clover detector.

The ^{112}Sn$(\alpha,\gamma)^{116}$Te reaction cross sections have been measured in the effective center of mass energy range 7.59 MeV $\leq E^{eff}_{c.m.} \leq$ 11.42 MeV at the FN Tandem Van de Graaff accelerator at the University of Notre Dame, using isotopically enriched ^{112}Sn targets in the form of thin self supporting foils. The covered energy range spans the Gamow window predicted for this reaction in the high temperature environment. In addition, the ^{112}Sn$(\alpha,p)^{115}$Sb reaction cross sections have also been investigated in the 9.97-11.42 MeV energy range.

The reaction cross sections have been measured using the activation method. The off-line detection system consisted of two Clover Ge detectors. Figure 1 shows the arrangement of detectors and the position of the activated sample in the counting setup.

The present results [5] agree with the previous two data points [3] within the experimental uncertainties. In addition, the measured results were compared with the NON-SMOKER statistical model code [6] calculations. The ^{112}Sn$(\alpha,p)^{115}$Sb results proved to be higher than the predictions. While an agreement is observed at higher energies for the ^{112}Sn$(\alpha,\gamma)^{116}$Te reaction, the experimental data deviate considerably from the theoretical prediction in the lower energy range. The comparison of the results with those of the recent study of α-induced reactions on ^{106}Cd [2] shows a similar behaviour: the theoretical predictions overestimate the (α,γ) measurements and underestimate the (α,p) measurements.

a) Kocaeli University, Umuttepe, Turkey

b) University of Notre Dame, South Bend, USA

[1] Zs. Fülöp et al., Nucl. Phys. A758 (2005) 90.

[2] Gy. Gyürky et al., Phys. Rev. C74 (2006) 025805.

[3] N. Özkan et al., Nucl. Phys. A710 (2002) 469.

[4] D. Galaviz et al., Phys. Rev. C71 (2005) 065802.

[5] N. Özkan et al., Phys. Rev. C75 (2007) 025801.

[6] T. Rauscher et al., At. Data Nucl. Data Tables 79 (2001) 47.

2.12 High-spin structure of ^{121}Xe

G. Berek, B.M. Nyakó, J. Timár and the HLHD collaboration [a)]

The neutron-deficient nuclei around mass number 120 are very well suited to study the interplay between single-particle and collective excitation modes. These nuclei with a few nucleons outside a closed-shell core are soft to γ-deformation and shape driving effects of nucleons in different orbitals can lead to co-existence of different shapes.

A high-statistics experiment aiming at the identification of hyperdeformed states [1] in A$\simeq$120 nuclei has provided valuable data for studying also the normal deformed states at the highest spins in this mass region. The aim of this work is to search for terminating bands in ^{121}Xe and ^{122}Xe as well as to test the cranked shell model at high spins.

The fusion-evaporation nuclear reactions ^{64}Ni(^{64}Ni,α3n) and ^{64}Ni(^{64}Ni,α2n) were used to populate high-spin states in ^{121}Xe and ^{122}Xe, respectively. The beam with energies of 255 and 261 MeV was provided by the Vivitron tandem accelerator at IReS, Strasbourg. The emitted γ-rays were detected by the EUROBALL IV spectrometer [2]. The detection of light charged particles was performed by means of the highly efficient DIAMANT array [3,4], which was mounted inside the target chamber.

A total of about 3.7 $\times 10^9$ Compton suppressed events was recorded when one charged particle has been detected in DIAMANT array. For the analysis of the one-α gated triple-coincidence cube a standard gating procedure was carried out with the help of the RADWARE software package [5].

The level scheme of ^{121}Xe has been constructed using $\gamma\gamma$-coincidence relations, as well as energy and intensity balances. Most of the excited states known from previous studies [6] were confirmed in our experiment and the previously known bands have been extended to higher spins.

In order to compare the high-spin states observed in ^{121}Xe with the theory we performed calculations using the configuration-dependent cranked Nilsson-Strutinsky (CNS) approach [7]. Within this formalism, the observed bands are described in terms of the low-j and the high-j valence orbitals with signature α and approximate principal quantum number N. The calculated configurations are traced in the deformation space (ϵ_2,ϵ_4,γ) as a function of spin I. Their energies are usually expressed in terms of (E-E_{rld}), i.e., the excitation energies with a rigid rotor reference subtracted. Pair correlations are neglected in the calculations. Thus, they can be considered as realistic only at high spins.

A deformed nucleus can increase its spin by collective rotation about an axis perpendicular to its symmetry axis. In a rotational band, higher spin states are built by a gradual alignment of the spin vectors of all the available valence nucleons until, eventually, full alignment is reached. At this point, the rotational band has lost its collectivity and is said to terminate.

Our preliminary results show that two of the bands lose their regular character at high spins, which may be interpreted as a transition from collective behaviour to a regime of non-collective oblate states.

a) see A. Al-Khatib *et al.*, ATOMKI Ann. Rep. (2006)

[1] B. M. Nyakó *et al.*, ATOMKI Ann. Rep. (2005)

[2] J. Simpson, Z. Phys. A 358 (1997) 139.

[3] J. N. Scheurer *et al.*, NIM A 385 (1997) 501.

[4] J. Gál *et al.*, NIM A 515 (2004) 502.

[5] D. C. Radford, NIM A 361 (1995) 297.

[6] J. Timár *et al.*, J. Phys. G 21 (1995) 783., and references therein

[7] A. V. Afanasjev, D. B. Fossan, G. J. Lane, and I. Ragnarsson, Phys. Rep. 322 (1999) 1.

2.13 Competition between collective and noncollective excitation modes at high spin in ^{124}Ba

A. Al-Khatib[a], A.K. Singh[a], H. Hübel[a], P. Bringel[a], A. Bürger[a], J. Domscheit[a], A. Neusser-Neffgen[a], G. Schönwasser[a], G.B. Hagemann[b], C. Ronn Hansen[b], B. Herskind[b], G. Sletten[b], J.N. Wilson[b], J. Timár, A. Algora, Zs. Dombrádi, J. Gál, G. Kalinka, J. Molnár, B.M. Nyakó, D. Sohler, L. Zolnai, R. Clark[c], M. Cromaz[c], P. Fallon[c], I.Y. Lee[c], A.O. Macchiavelli[c], D. Ward[c], H. Amro[d], W.C. Ma[d], M. Kmiecik[e], A. Maj[e], J. Styczen[e], K. Zuber[e], K. Hauschild[f], A. Korichi[f], A. Lopez-Martens[f], J. Roccaz[f], S. Siem[f], F. Hannachi[g], J.N. Scheurer[g], P. Bednarczyk[h], Th. Byrski[h], D. Curien[h], O. Dorvaux[h], G. Duchene[h], B. Gall[h], F. Khalfallah[h], I. Piqueras[h], J. Robin[h], A. Görgen[i], K. Juhász[j], S.B. Patel[k], O.A. Evans[l], G. Rainovski[l], G. Benzoni[m], A. Bracco[m], F. Camera[m], S. Leoni[m], P. Mason[m], B. Million[m], A. Paleni[m], R. Sacchi[m], O. Wieland[m], C.M. Petrache[n], D. Petrache[n], G. La Rana[o], R. Moro[o], G. De Angelis[p], J.C. Lisle[q], B. Cederwall[r], K. Lagergen[r], R.M. Lieder[s], E. Podsvirova[s], W. Gast[s], H. Jäger[s], N. Redon[t]

High-spin states in ^{124}Ba were investigated in two experiments using the ^{64}Ni(^{64}Ni,4n)^{124}Ba reaction at three different beam energies. In-beam γ-ray coincidences were measured with the Euroball and Gammasphere detector arrays, respectively. In the experiment with Euroball, the CsI detector array Diamant was employed to discriminate against charged-particle channels. Six new rotational bands were observed in ^{124}Ba and previously known bands were extended to higher spins and in the low-spin region. One of the bands shows a transition from collective to non-collective behavior at high spins. Configuration assignments are suggested on the basis of comparison with cranked shell model and cranked Nilsson-Strutinsky calculations [1].

a) Helmholtz-Institut für Strahlen-und Kernphysik, Universität Bonn, Nussallee 14-16, D-53115 Bonn, Germany

b) Niels Bohr Institute, Blegdamsvej 17, DK-2100 Copenhagen Ø Denmark

c) Nuclear Science Division, Lawrence Berkeley Laboratory, Berkeley California 94720, USA

d) Department of Physics, Mississipi State University, Mississipi State, MS 39762, USA

e) Niewodniczański Institute of Nuclear Physics, PAN, 31-342 Kraków, ul. Radzikowskiego 152, Poland

f) CSNSM Orsay, IN2P3/CNRS, F-91405 Orsay, France

g) Centre d Etudes Nuclèaires deBordeaux-Gradignan, F-33175 Gradignan, France

h) Institut de Recherches Subatomiques, CNRS-IN2P3, F-67037 Strasbourg, France

i) DAPNIA/SPhN, CEA-Saclay, F-91191 Gif-sur-Yvette, France

j) Faculty of Informatics, University of Debrecen, Hungary

k) Department of Physics, University of Bombay, Mumbai, India

l) Oliver Lodge Laboratory, University of Liverpool, Liverpool L69 7ZE, United Kingdom

m) INFN and Dipartimento di Fisica, Universita degli Studi di Milano, via Celoria 16, I-20133 Milano, Italy

n) INFN and Dipartimento di Fisica, Università di Camerino, via Madonna delle Carceri, I-62032 Camerino, Italy

o) INFN and Physical Science Department, Complesso Universitario di Monte S.Angelo, via Cinthia, I-80126 Napoli, Italy

p) INFN, Laboratori Nazionali di Legnaro, via Romea 4, I-35020 Legnaro, Italy

q) Schuster Laboratory, University of Manchester, Brunswick Street, Manchester M13 9PL, United Kingdom

r) Department of Physics, Royal Institute of Technology, SE-10691 Stockholm, Sweden

s) Institut für Kernphysik, Forschungszentrum Jülich, D-52425 Jülich, Germany

t) IPN Lyon, IN2P3/CNRS, Universitè Lyon-1, F-69622 Villeurbanne, France

[1] A. Al-Khatib *et al.*, Phys. Rev. C74 (2006) 014305.

2.14 Searching for hyperdeformed transmission resonances in ^{232}Pa

L. Csige, M. Csatlós, T. Faestermann[b], Z. Gácsi, J. Gulyás, D. Habs[a], R. Hertenberger[a], M. Hunyadi, A. Krasznahorkay, R. Lutter[a], H.J. Maier[a], P.G. Thirolf[a], H.-F. Wirth[b]

Besides the thorium and uranium isotopes with respect to hyperdeformation the double-odd nucleus ^{232}Pa is of great interest. The fine structure of the fission resonances of this nucleus have been studied so far only via the (n,f) reaction [1] but the results of these experiments showed no conlcusive evidence for the existence of a triple-humped fission barrier of ^{232}Pa.

Using the ^{231}Pa(d,pf) reaction on a radioactive ^{231}Pa target the fission probability of ^{232}Pa as a function of the excitation energy has been measured in order to search for hyperdeformed (HD) rotational bands. In contrast to the (n,f) reaction, the (d,p) reaction can transfer considerable angular momentum. The angular distribution of fission fragments was also studied to get information on spin and K-values of the rotational bands.

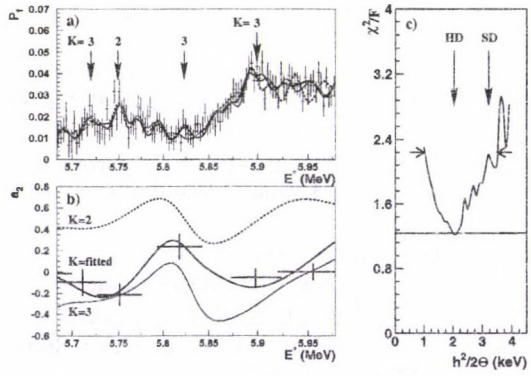

Figure 1. a) Fission probability of ^{232}Pa fitted with rotational bands. Dashed lines indicate the fitted rotational bands with K=2 and K=3 for all members, respectively. b) Fission fragment angular correlation data calculated for rotational bands with different K-values on the experimental a_2 points. c) Result of the χ^2-analysis.

The experiment was performed at the Tandem accelerator of the Maier-Leibnitz Laboratory (MLL) at Garching using ^{231}Pa(d,pf) reaction at a bombarding energy of 12 MeV. The kinetic energy of the ejectile was analysed by a Q3D magnetic spectrometer, set to 139.4°. An energy resolution of ΔE=11 keV was achieved. Fission fragments were detected by a position sensitive avalanche detector (PSAD), which consisted of two perpendicular wire planes, thus allowing for a detection of the fission fragment angular correlation with respect to the recoil axis. The fission detector covered a wide range of $\Theta_R = 0° - 100°$ relative to the recoil axis with a solid angle coverage of 10% of 4π.

Fig. 1a) displays the fission probability spectrum between E=5.7 MeV and E=5.9 MeV. In order to describe the rotational structure, overlapping rotational bands were assumed with the same moment of inertia (θ), and intensity ratio for the band members. During the fitting procedure the energy of the band head and the absolute intensity of the band were used as free parameters while a common rotational parameter was adopted for each band. The angular correlation was analyzed by fitting it with even Legendre-polynomials up to fourth order: the angular coefficients a_2 and a_4 were determined for the most prominent structures parameterized by a series of rotational bands with K-value assigments as indicated in Fig. 1b). The high-resolution excitation energy spectrum deduced from the proton spectrum shown in Fig. 1a) in combination with the analysis of the angular distribution measurement in a consistent description indicate the interpretation of the transmission resonance structures around 5.7 and 5.9 MeV as hyperdeformed rotational bands. The rotational parameter was determined as $\hbar^2/\theta = 2.0^{+1.5}_{-1.0}$ keV based on the χ^2 test shown in Fig. 1c).

a) Ludwig Maximilians Univ., München, Germany

b) Technische Univ. München, Garching, Germany

[1] S. Plattard *et al.*, Phys.Rev.Lett. 46 (1981) 633.

2.15 New fission resonances observed in ^{231}Pa(^{3}He,df)^{232}U

L. Csige, M. Csatlós, T. Faestermann[b], Z. Gácsi, J. Gulyás, D. Habs[a], R. Hertenberger[a], M. Hunyadi, A. Krasznahorkay, R. Lutter[a], H.J. Maier[a], P.G. Thirolf[a], H.-F. Wirth[b]

According to recent calculations the depth of the third minimum for U isotopes is predicted to be much deeper than previously believed [1]. Calculations performed in Ref. [1] predicts actually two deep third minima for different values of the reflection-asymmetry. The previous experimental data obtained so far for ^{234}U [2] and ^{236}U [3] supports the above picture.

In our most recent experiment the fission probability of ^{232}U was measured as a function of the excitation energy, using the ^{231}Pa(^{3}He,df) reaction in order to get information about the third minimum of ^{232}U. The experiments were performed at the Tandem accelerator of the Maier-Leibnitz Laboratory (MLL) at Garching with ^{3}He beam at energy of E=38.1 MeV. The kinetic energy of the ejectiles was analysed by a Q3D magnetic spectrometer set to 35°. Fission fragments were detected by a position sensitive avalanche detector (PSAD), which consisted of two perpendicular wire planes, thus allowing for a detection of the fission fragment angular correlation with respect to the recoil axis ($\Theta_R = 0° - 100°$) with a solid angle coverage of 10% of 4π.

The measured fission probability spectrum is shown in Fig. 2a). In contrast to our previous results obtained so far for ^{240}Pu, ^{234}U and ^{236}U similar resonance structure has not been observed. This may partly be explained by the asymmetry of the inner and outer fission barrier heights which does not favor the occurrence of the transmission resonances and may be attributed to the reduced rotational energy differences due to the lower target spin in ^{231}Pa ($3/2^-$) compared to $7/2^-$ in ^{235}U. A comparison of the experimental angular distribution to the calculated ones (for bands with different K-values) confirms the appearance of rotational bands with low K-values (Fig. 2b).

The reduced energy resolution of FWHM=20 keV caused by the larger energy loss of ^{3}He, compared to the previously used deuterons may also inhibit the resolved observation of rotational states. The result of the fitting procedure suggests the interpretation of the structure as being hyperdeformed fission resonances (three rotational bands with K=1). However, a superdeformed description of the structure can not be excluded at the present time. We are planning to repeat the experiment soon with better energy resolution.

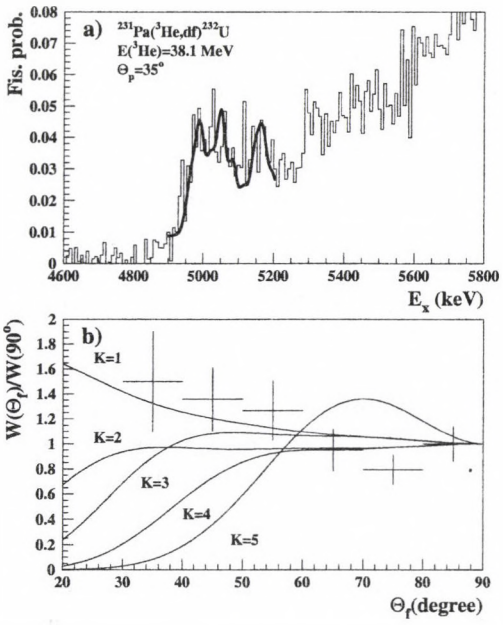

Figure 2. a) Fission probability spectrum measured in ^{231}Pa(^{3}He,d)^{232}U. b) Experimental angular distribution for the 4.9 MeV - 5.2 MeV energy region with angular distributions calculated for rotational bands with different K-value.

a) Ludwig Maximilians Univ., München, Germany

b) Technische Univ. München, Garching, Germany

[1] S. Cwiok *et al.*, Phys.Lett. B322(1994)304.

[2] A. Krasznahorkay *et al.*, Phys.Lett. B461(1999)15.

[3] M. Csatlós *et al.*, Phys.Lett. B615(2005)175.

2.16 Study of the performance of tracking algorithms for the DESPEC planar setup

A. Algora, B. Rubio[a], S. Tashenov[b], J. Gerl[b], B. Quintana[c], M. Doncel[c], F. Lorenzo[c] and A. Jungclaus[d] for the DESPEC Collaboration

DESPEC is one of the experiments of the low-energy branch project of the future installations at FAIR (GSI). The basic instrumentation of this setup includes a set of implantation detectors, a Ge array and neutron detectors to study the decay properties of exotic nuclei. Presently the collaboration is considering two possible setups for the Ge array. One possibility is to use an array of stacks of planar Ge detectors specifically designed for DESPEC. The other alternative is to use standard segmented Ge detectors of EXOGAM [1] or TIGRESS [2] type. The R&D phase requires the realization of Monte Carlo (MC) simulations to determine the optimal setup for the future facility.

In this report we present a preliminary study of the application of tracking techniques to the results of the simulations. The idea is to use the recent developments for AGATA to exploit maximally the possibilities of the new array for DESPEC. To perform this study a new MC code was developed which generates a list-mode output that can be used in combination with the tracking programs and algorithms developed for AGATA. This output resembles the ones obtained in a real experiment and contains information on the position of the interactions and the deposited energy in the sensitive parts of the array following the interaction with radiation.

The results obtained for the planar setup are presented here. This setup consists of an array of 24 composite planar detectors. Each detector unit is formed by a stack of three planar Ge detectors with dimensions $72 \times 72 \times 22$ mm^3 with an active Ge volume of $68 \times 68 \times 22$ mm^3. The distance between the planars is 3 mm and the stack is encapsulated in an Al capsule of 1.5 mm thickness. The described geometry has been implemented using the MC code GEANT4 [3].

In this work the tracking code MGT developed by D. Bazzacco was used [4]. The results, presented in Table 1, correspond to the application of the MGT code to simulation data of centered, point-like monoenergetic gamma sources. The first column shows the energy of the emitted gamma rays. The second presents the maximum peak efficiency that can be obtained with the setup (as a total absorption spectrometer). The third and fourth columns show the peak to total ratio obtained in case the planar detectors and the stacks are considered individually. The fifth column shows the peak to total ratio obtained after the application of the tracking code. Finally, in the last column the efficiency of the tracking algorithm is given.

As part of our work the effect of emission of gamma cascades on the tracking efficiency has also been studied. The next step of our work will be the study of the performance of tracking algorithms for the segmented CLOVER setup.

Table 1. Results of the simulations for monoenergetic gamma rays (see text for details).

E MeV	Eff Peak	P/T pl..	P/T st.	P/T Track.	Track. Eff.
0.10	47.1	85	89	89	99
0.25	38.2	44	55	69	96
0.50	26.7	19	32	48	96
1.00	18.4	11	21	36	94
2.00	13.2	7	16	28	92
5.00	6.8	3	7	13	81

Acknowledgments: A.A. acknowledges the collaboration of Prof. D. Bazzacco and Dr. E. Farnea in the realization of this work.

a) IFIC, CSIC-Univ. de Valencia, Valencia, Spain
b) GSI, Darmstadt, Germany
c) Univ. de Salamanca, Salamanca, Spain
d) Univ. Autonoma de Madrid, Madrid, Spain

[1] http://www.ganil.fr/exogam/
[2] H. C. Scraggs *et al.*, Nucl. Inst. and Meth. A543 (2005) 431
[3] S. Agostinelli *et al.*, Nucl. Inst. and Meth. A506 (2003) 250
[4] D. Bazzacco, The MGT code, unpublished

2.17 Phase Transitions in Algebraic Cluster Models

H. Yepez-Martinez[a], *J. Cseh*[b], *P. O. Hess*[c]

Phase transitions in nuclear systems are of utmost interest. An interesting class of phase transitions can be seen in algebraic models of nuclear structure. They are called shape-phase transitions due to the following reason. These models have analytically solvable limiting cases, called dynamical symmetries, which are characterized by a chain of nested subgroups. They correspond to well-defined geometrical shape and behaviour, e.g. to rotation of an ellipsoid, or spherical vibration. The general case of the model, which includes interactions described by more than one group-chain, breaks the symmetry, and changing the relative strengths of these interactions, one can go from one shape to the other. In doing so a phase-transition can be seen. A phase-transition is defined as a discontinuity of some quantity as a function of the control parameter, which gives the relative strength of the interactions of different symmetries. Real phase transitions can take place only in infinite systems, like in the classical limits of these algebraic models, when the particle number N is very large: $N \to \infty$. For finite N the discontinuities are smoothed out, nevertheless, some indications of the phase-transitions can still be there.

A controlled way of breaking the dynamical symmetries may reveal another very interesting phenomenon, i.e. the appearance of a quasidynamical (or effective) symmetry. This rather general symmetry-concept of quantum mechanics corresponds to a situation, in which the symmetry-breaking interactions are so strong that the energy-eigenfunctions are not symmetric, i.e. are not basis states of an irreducible representation of the symmetry-group, rather they are linear combinations of these basis states. However, they are very special linear combinations in the sense that their coefficients are (approximately) identical for states with different spin values. When this is the case, then the underlying intrinsic state is the same, and the states are said to form a (soft) band.

The phase-transitions, as well as the persistence of the quasidynamical symmetries in the algebraic models of quadrupole collectivity have extensively been studied. In a recent work [1] we have addressed these questions in relation with another important collectivity of nuclei, i.e. clusterization.

Two models were considered, a phenomenological one, containing no Pauli-principle, and a semimicroscopic one, which is based on a microscopically determined model space, being free from the Pauli-forbidden states. The interactions were treated in a phenomenologic and algebraic way in both cases. In this respect the two models have a similar group-structure. We have studied the $SU(3)$ - $SO(4)$ phase-transition, related to the description of the relative motion in terms of the vibron model (in its simplest form in the phenomenological model and in a properly truncated form in the semimicroscopic description).

The analytical study of the large-N limit of both models shows a first order phase transition. We have carried out numerical calculations as well. Three binary cluster systems were chosen, in which the number of open-shell clusters were zero, one and two, respectively. The numerical studies show that the phase-transition is smoothed out for finite N systems, but some fingerprints of it still can be seen.

The appearance of the quasidynamical $SU(3)$ symmetry has also been studied, when moving away from the limit of the real $SU(3)$ dynamical symmetry. It turned out that in each case, when there is a real dynamical symmetry in the limiting case (in the sense that a well-defined $SU(3)$ quantum number can be associated to a band), this symmetry survives as quasidynamical symmetry at least up to the critical value of the control parameter.

[1] H. Yepez-Martinez, J. Cseh, P. O. Hess, Phys. Rev. **C74** (2006) 024319.

[a] *UACM, San Lorenzo Tezonco, Mexico*
[b] *ATOMKI, Debrecen, Hungary*
[c] *Inst. de Ciencias Nucleares, UNAM, Mexico*

2.18 Testing the U(4|12) nuclear cluster supersymmetry scheme with B($E2$) rates

G. Lévai, J. Cseh, P. Van Isacker[a)]

The spectroscopic properties of some light core+α-particle-type cluster systems seem to exhibit certain correlations, and recently we proposed the U(4|12) nuclear cluster supersymmetry to account for them. In this scheme the bosonic and fermionic excitations are identified as oscillator quanta of the relative motion, and nucleon holes in the p-shell core cluster, respectively. As a first step we discussed the α-cluster states of ^{20}Ne and ^{19}F as members of the same supermultiplet assigned to $N_{\rm F} = 0$ and $N_{\rm F} = 1$ fermion, respectively [1]. It turned out that the validity of this supersymmetry scheme is at the same level as that of other supersymmetry schemes in the Os-Ir-Pt region based on the U(6) symmetry of the interacting boson model. The observables analysed in terms of the U(4|12) supersymmetry were the energy spectrum, B($E2$) rates and one-nucleon transfer spectroscopic factors.

Next we extended this scheme to $A = 18$ nuclei, corresponding to systems with $N_{\rm F} = 2$ fermions [2]. (It is notable that other nuclear supersymmetry schemes are restricted to $N_{\rm F} \leq 1$.) In this way the unified description of the α-cluster states of six nuclei, ^{20}Ne, ^{19}F, ^{19}Ne, ^{18}O, ^{18}F and ^{18}Ne became possible. In Ref. [2] a qualitative analysis of one-nucleon transfer spectroscopic factors has been given in six different reactions between the nuclei mentioned above. It was found that the strict selection rules imposed on these processes by the U(4|12) supersymmetry seem to act rather precisely, as the C^2S values of the forbidden transitions are typically an order of magnitude smaller that those of the allowed ones.

In order to estimate the validity of this supersymmetry scheme in a more quantitative way, we extended our analysis to the electric quadrupole transitions [3]. Our aim was to test whether the B($E2$) values seen in the six nuclei can be described by a *common* electric quadrupole transition operator

$$T^{(E2)} = q_{\rm B} B^{(1,1)2} + q_{\rm F}^{\rm IS} A^{(1,1)200} + q_{\rm F}^{\rm IV} A^{(1,1)201} \, .$$

Here the B and A operators act in the bosonic and fermionic model space, respectively, where they have $(\lambda, \mu) = (1, 1)$ SU(3) character and are rank-2 SO(3) tensors. The A operators are also characterized by the isospin quantum number T, and accordingly, they have isoscalar and isovector nature. In our analysis we fitted the three parameters $q_{\rm B}$, $q_{\rm F}^{\rm IS}$ and $q_{\rm F}^{\rm IV}$ to the available B$(E2)_{\rm Exp}$ values first separately (nucleus by nucleus), and then jointly. There were altogether 42 E2 transitions with well-established mean value and error, and a few more with upper or lower limit. Furthermore, there were 14 B($E2$) values for transitions between major shells, which are forbidden in the supersymmetry scheme.

The results confirmed the existence of correlations between the E2 transitions of the six nuclei in several ways [3]. *1)* The parameter sets and thus the B($E2$) values obtained from the separate and joint fits were close to each other; a modearte deviation was seen only in the case of ^{18}O, where there might be considerable mixing between the $K^\pi = 0_1^+$ and 0_2^+ bands. *2)* Parameters extracted individually from the data ($q_{\rm B}$ from ^{20}Ne and $q_{\rm F}^{\rm IV}$ from transitions between pairs of isobaric analogue states) were rather close to the fitted values. *3)* Substituting the two fermionic parameters into the E2 operator describing the B($E2$) values of transitions in the respective *core* nuclei the calculated values agreed rather well with the experimental ones, with the exception of ^{14}C, the core nucleus in the α cluster states of ^{18}O. *4)* The transitions forbidden by the selection rules of the model were found to be weak in experiment too, again, with the exception of ^{18}O. *5)* The avaiable experimental quadrupole moments were also reproduced well using the extracted parameters.

a) GANIL, Caen, France

[1] G. Lévai, J. Cseh, P. Van Isacker, Eur. Phys. J. A **12** (2001) 305.

[2] G. Lévai, ATOMKI Annual Report (2005) 24.

[3] G. Lévai, J. Cseh, P. Van Isacker, submitted.

2.19 Deformation inside and outside the nuclear molecules

J. Cseh[a)], J. Darai[b)], N.V.Antonenko[c)], A. Algora[a)], P. O. Hess[d)], R.V. Jolos[c)], W. Scheid[e)]

Clusterization is an important phenomenon both in light and in heavy nuclei. The two basic natural laws governing the clusterization (just like the composition of nuclei from nucleons) are the energy-minimum principle, and the Pauli-exclusion principle. In a fully microscopic description of clusterization both aspects are taken into account. This kind of description, however, is limited to the territory of light nuclei.

Many interesting aspects of the clusterization, like e.g. the appearance of exotic cluster-configurations, show up only in heavy nuclei. Phenomenologic approaches are applied both to light and to heavy nuclei, on an equal footing, but these models do not really contain the effects of the antisymmetrization, or it is not under control, what aspects of the exclusion principle is incorporated.

Recently we have developed an approach, which involves both the energetic preference and the exclusion principle [?]. The antisymmetrization is not carried out explicitely, it is treated in an approximate way, but it is done microscopically in a well-controlled manner, and consistency-check measures, how effective it is.

We calculate the energetic preference of different clusterizations both on the basis of simple binding-energy-arguments [?], and from the Dinuclear System Model (DNS) [?], including Coulomb as well as nuclear interactions. The potential energy is calculated both for the usual pole-to-pole configuration, and for those more compact configurations, which turn out to be allowed from the microscopic viewpoint.

The exclusion principle is treated by the application of a selection rule, related to the microscopic structure. For light nuclei it is based on the real $U(3)$ symmetry [?], and it is exact to the extent to which the leading term representation is valid. In heavy nuclei it is based on the quasidynamical, or effective $U(3)$ symmetry [?]. Its validity is shown by the consistency of the quadrupole deformation of the cluster state and the state of the parent nucleus.

In these considerations the deformation of the clusters are taken into account, too. Therefore, we investigate the interrelation of the quadrupole deformation and the clusterization from two aspects. On the one side, looking at the possible clusterizations of states with different quadrupole deformation of the parent nucleus, we tend to detemine the deformation-dependence of various cluster-configurations. On the other side, we can investigate the role of the cluster-deformation inside the cluster (or molecular) nuclear states; i.e. figure out, how the relative orientation of deformed clusters can build up different states of the same nucleus.

Here we report on the application of the above methods to the ^{40}Ca nucleus, which is investigated also in the framework of the Antisymmetrised Molecular Dynamics (AMD) [?], thus we can compare our results with those of a fully microscopic treatment. This is interesting for the special case of the ^{40}Ca nucleus, too, at the same time, however, it can be considered as a test of our method, which we apply also to heavy nuclei [?].

We have considered the binary clusterizations of the ground, superdeformed and hyperdeformed states of ^{40}Ca [?]. The clusters were considered to have deformation, like the free nuclei, and we applied no constraint for their relative orientation.

As shown in Figure 1, the ground state prefers asymmetric cluster-configurations, the hyperdeformed state symmetric ones, while the superdeformed state shows more complicated picture. It is interesting, that the ^{12}C+^{28}Si clusterization is allowed in each states. Nevertheless, they correspond to different geometrical configurations, since the relative orientation of the deformed clusters are different.

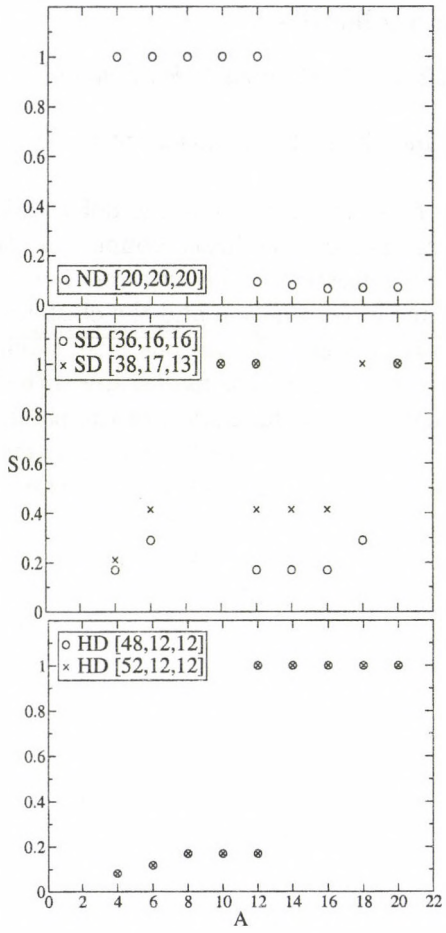

Figure 1. Relative preference of different binary clusterization of the ^{40}Ca nucleus. ND stands for the normal deformed (ground) state, while SD and HD indicate super and hyperdeformed states, respectively.

From the energetic viewpoint this clusterization is in half-way between the energetically most preferred and least preferred alpha-like configurations. The energetic preference turned out to be similar from the simple binding-energy consideration and from the detailed potential-energy calculations.

Our finding is very much in line with the that of the fully microscopic AMD calculations [?], which concluded that the superdeformed state has an ^{12}C+^{28}Si character. Furthermore, the coupling of the clusters are strong in both descriptions. This similarity can be considered as a check of our method with respect to the fully microscopic description, which seems to be very promising from the viewpoint of the more extensive applications to heavy nuclei.

References

[1] J. Cseh, J. Darai, N.V. Antonenko, A. Algora, P. O. Hess, R.V. Jolos, W. Scheid, Rev. Mex. Fis. **S52**, 11 (2006).

[2] B. Buck, A. C. Merchant, and S. M. Perez, Few-Body Systems **29** (2000) 53; B. Buck, A. C. Merchant, M. J. Horner, and S. M. Perez, Phys. Rev. C**61** (2000) 024314.

[3] V.V. Volkov, Phys. Rep. **44**, 93 (1978); *Deep inelastic nuclei reactions* (Energoizdat, Moscow, 1982).

[4] J. P. Elliot, Proc. R. Soc. A **245** (1958) 128, 562.

[5] P. Rochford, D. J. Rowe, Phys. Lett B **210** (1988) 5;
D. J. Rowe, P. Rochford, J. Repka, J. Math. Phys. **29** (1988) 572.

[6] Y. Kanada-Enyo, M. Kimura, H. Horiuchi, AIP Conf. Proc. **644** (2003) 188.

[7] J. Cseh, A. Algora, J. Darai, P. O. Hess, Phys. Rev. **C70**, 034311 (2004).

[a] *ATOMKI, Debrecen, Hungary*
[b] *Univ. Debrecen, Debrecen, Hungary*
[c] *JINR, Dubna, Russia*
[d] *Inst. Cienc. Nucl., UNAM, Mexico*
[e] *JL Univ. Giessen, Germay*

2.20 Ternary clusterization and quadrupole deformation

A. Algora[a], *J. Cseh*[a], *J. Darai*[b], *P.O. Hess*[c]

The investigation of exotic nuclear shapes, e.g. superdeformed and hyperdeformed states is one of the most interesting topics in recent nuclear structure studies. The appearance of exotic cluster configurations (or exotic cluster decay) is another issue of utmost interest. The combination of these two problems brings us to an exciting question: what is the interrelation of these two phenomena, i.e. what are the possible clusterizations of nuclear states with exotic shapes. In a recent paper [1] we addressed this question from the angle of the ternary clusterization. We applied methods which can be generalized to more complicated multicluster-configurations in a straightforward way.

In comparison with other cluster studies the novel feature of our work is that we addressed problems which has been investigated so far (in a systematic manner) only with phenomenologic approaches. Our description is not fully microscopic rather it can be called semimicroscopic, but it reaches a territory which is hopeless for the fully microscopic calculations at present.

As specific examples we considered ternary cluster-configurations in the ground, superdeformed and hyperdeformed states of the light ^{36}Ar and heavy ^{252}Cf nuclei, which were investigated from the viewpoint of possible binary clusterization in [2]. In case of ^{36}Ar the superdeformed state has been found experimentally, and a theoretical prediction is available for its hyperdeformed state. In case of ^{252}Cf the main motivation is provided by the spontaneous fission experiments from its ground state, which indicated several very exotic clusterizations. As for superdeformed and hyperdeformed states of this nucleus, we considered the results of the Nilsson-model with appropriate quadrupole deformation.

An interesting phenomenon found in our work is the appearance of the same cluster-configuration in very different states. E.g. in the ground-state and superdeformed state of a nucleus, or in the superdeformed and hyperdeformed states, or in each of these three. In the ^{36}Ar case e.g. the ^{24}Mg+^{8}Be+^{4}He, ^{20}Ne+^{12}C+^{4}He, ^{16}O+^{12}C+^{8}Be clusterizations are allowed in each of the three states. Furthermore, they are energetically favored as well. (Please, note their similarity to the ^{24}Mg+^{12}C binary configuration, which turned out to be allowed in the ground-state, superdeformed and hyperdeformed states of ^{36}Ar as well [2]. Energetically the ternary configurations are more favored.) The reason for this phenomenon is that if the deformation of the clusters is taken into account, and their different orientations are allowed in the description, and furthermore the effect of the antisymmetrization is included, then different spatial configurations of the same clusters may result in states of the parent nucleus with very different quadrupole configurations. This conclusion is new and unexpected in comparison with the conclusions of the phenomenological models on this phenomenon, and it turns out to be an effect which is ruled out in some approaches by some simplifying model assumptions (e.g. not taking into account triaxial deformations, some relative orientations, or the exclusion principle).

As for the clusterization of the ^{252}Cf nucleus, indicated by the spontaneous fission experiments, we have found that most of the ternary configurations we have investigated are forbidden in the ground-state. Many of them are allowed, however, in the superdeformed and hyperdeformed states. This finding also indicates that the spontaneous fission takes place via the (tiny) component of the ground-state wave function which corresponds to an extremely deformed shape.

[1] A. Algora, J. Cseh, J. Darai, P.O.Hess, Phys. Lett. B639 (2006) 451.

[2] J. Cseh, A. Algora, J. Darai, P.O.Hess, Phys. Rev. C70 (2004) 034311.

[a] *ATOMKI, Debrecen, Hungary*

[b] *Univ. Debrecen, Debrecen, Hungary*

[c] *Inst. Cienc. Nucl., UNAM, Mexico*

2.21 Renormalization group method versus perturbation theory

I. Nándori

According to the main concept of perturbation theory, perturbative treatment is applicable if one of the parameter of the model is much smaller compared to the others or some characteristic length-scale. If the theory has only two parameters, the perturbative regimes are $g_1 \gg g_2$ and $g_1 \ll g_2$. However, non-perturbative solutions are required in the cross-over domain ($g_1 \sim g_2$).

This general strategy finds a natural application in quantum field theory (QFT). The models in QFT are defined at high energy where the coupling constants are smaller than the momentum cutoff (k) and hence the perturbative treatment is allowed. However, one has to determine the low energy effective theory of the model in order to read off measurable quantities and the validity of the high energy perturbative approach is not necessarily guaranteed at low energies. During this procedure which is called renormalization, the momentum cutoff has been moved from high to low energies ($k \to 0$) and the parameters become cutoff dependent. The lowering of the momentum cutoff can be considered as the analog to the thermodynamical limit of microscopic theories in statistical physics. The renormalization group (RG) method is one of the non-perturbative technics which can be used in the cross-over domain in order to connect the high and low energy perturbative regimes.

In Refs.[2-4] we show how this general scenario works for a particular model which has been used as a toy model of quark-confinement [1]. The central subjects of investigation is the two-dimensional massive sine-Gordon (MSG) scalar field theory defined by the action

$$S = \int d^2x \left[\frac{1}{2}(\partial_\mu \phi)^2 + \frac{1}{2}M^2\phi^2 + y\cos(b\phi)\right],$$

where ϕ is a one-component scalar field and the parameters are the mass M, the Fourier amplitude y and the frequency b. The RG analysis determines the scaling of the Fourier amplitude in the strong coupling limit ($M > y$)

$$\left(2 + k\frac{d}{dk}\right)\tilde{y}(k) = \frac{b^2}{4\pi}\,\frac{k^2\,\tilde{y}(k)}{k^2 + M^2}, \qquad (1)$$

where the dimensionless $\tilde{y} = k^{-2}y$ is introduced to eliminate the trivial scale-dependence and M, b are constants. The RG method connects the high and low energy perturbative scaling regimes. In the high energy regime ($M \ll k$), the mass term is negligible, the model possess a periodic symmetry and the solution of Eq.(1) is

$$\tilde{y}(k) \simeq \tilde{y}_0\; k^{-2+b^2/(4\pi)},$$

where $\tilde{y}_0$ is the initial value. For $b^2 < 8\pi$ ($b^2 > 8\pi$) the Fourier amplitude $\tilde{y}(k)$ is increasing (decreasing) parameter if the scale k is decreased (see the figure). At low energies ($M \gg k$), the mass term becomes important and the periodicity has been broken explicitly by the mass which results in a trivial scaling for the Fourier amplitude

$$\tilde{y}(k) \simeq \tilde{y}_0\; k^{-2}$$

which holds independently of b.

Similar RG analysis has been applied in the weak coupling limit ($M < y$) in order to study confining properties of the model and the conjectures of [1] have been confirmed.

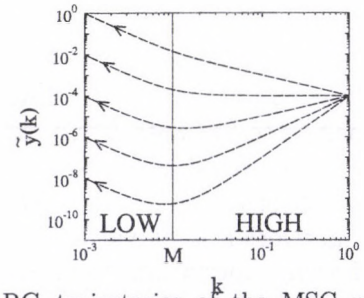

Figure RG trajectories of the MSG model obtained by the solution of Eq.(1) for various frequencies $b^2 = 4\pi, 8\pi, 12\pi, 16\pi, 20\pi$ from top to bottom.

[1] S. Coleman, Annals of Phys. **101** (1976) 239.

[2] I. Nándori, Journal of Phys. A **39** (2006) 8119.

[3] U. D. Jentschura, I. Nándori and J. Zinn-Justin, Annals of Phys. **321** (2006) 2647.

[4] I. Nándori, in preparation; S. Nagy, *et al.* submitted for publication, arXiv: hep-th/0611216.

3.1 Ionization of the hydrogen atom by intense ultrashort laser pulses

S. Borbély[a)], *L. Nagy*[a)], *K. Tőkési*

In this work the ionization probability of the hydrogen atom is studied by ultrashort laser pulses applying quantum mechanical and classical description of the collision system.

The exact solution of the Schrödinger equation for an atomic system in a radiation field is not known. Numerical calculations which solve the coupled state equations using different basis sets were performed, but they converge very slowly at high radiation field intensities. These numerical calculations are not efficient for complex systems, therefore different approaches were proposed. Our present approximation is based on the solution of the time dependent Schrödinger equation (TDSE) where the Coulomb interaction between the active electron and the target nucleus is taken into account as a perturbation. The time dependent wavefunction of the active electron is expanded in terms of Volkov functions (solution of the TDSE for a free electron in radiation field) as:

$$\Psi(\vec{r},t) = \int d\vec{k} c(\vec{k},t) \Psi_V(\vec{r},t;\vec{k}), \qquad (1)$$

where

$$\Psi_V(\vec{r},t;\vec{k}) = e^{i(\vec{k}+\vec{A}(t))\vec{r}} e^{-\frac{i}{2}\int_0^t dt'(\vec{k}+\vec{A}(t'))^2}, \quad (2)$$

with $\vec{A}(t) = -\int_0^t \vec{E}(t)dt$, and $\vec{E}(t)$ is the laser electric field vector. As a first approximation, the Coulomb interaction can be neglected, and the expansion coefficients can be written as

$$c(\vec{k},t) \equiv c(\vec{k}) = \frac{1}{(2\pi)^3} \left\langle e^{i\vec{p}\vec{r}} | \psi_i \right\rangle, \qquad (3)$$

where ψ_i is the initial state wavefunction. The results given by Eq. (3) is known as the Volkov approximation.

As a second approximation, the Coulomb interaction is treated as a small perturbation and the expansion coefficients can be written as:

$$c(\vec{k},t) = c(\vec{k}) + c^{(1)}(\vec{k},t), \qquad (4)$$

where $c^{(1)}(\vec{k},t)$ is the solution of the following equation:

$$\left[\frac{\partial}{\partial t} + E\frac{\partial}{\partial k_z} - iE(k_z t - \int_0^t A(t')dt')\right] c^{(1)}(\vec{k},t)$$

$$= -\frac{i}{(2\pi)^3} \int d\vec{s} c(\vec{k}+\vec{s}) e^{-\frac{i}{2}\vec{s}(\vec{s}t+2\vec{k}t+2\int_0^t \vec{A}(t')dt')}$$

$$\times \int d\vec{r} V(\vec{r}) e^{i\vec{s}\vec{r}}, \qquad (5)$$

where $V(r)$ is the Coulomb potential. The ionization probabilities can be calculated by the help of the coefficients and the wavefunctions. The results given by Eq. (4) is referred as results with perturbation model. The ionization probabilities were also calculated within the framework of the classical trajectory Monte Carlo (CTMC) method. In Fig. 1. the ionization probabilities are compared applying different theoretical models.

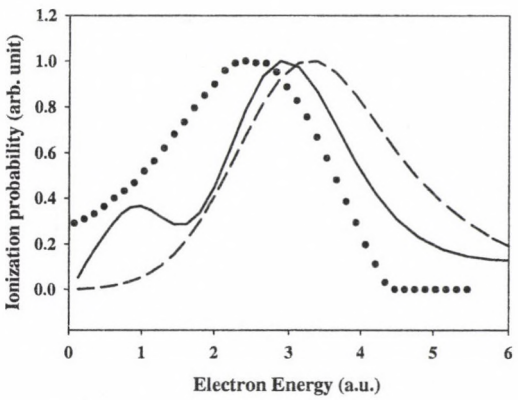

Figure 1. Ionization probabilities as a function of electron energy obtained from H(1s) targets illuminated by laser pulses characterized by $F_0 \sin(\omega t - (\omega\tau + \pi)/2) \sin^2(\pi t/\tau)$ with F_0= 1 au. τ=5 au. and ω=0.05 au. Dashed line: Volkov approximation, Solid line: perturbation model, circle: CTMC model.

Acknowledgements

The work was supported by the Domus Hungarica Scientiarum et Artium, the Inst. for Research Programmes (Sapientia Fundation), the grant "Bolyai" from the Hungarian Academy of Sciences, and the National Office for Research and Technology.

a) Babeş-Bolyai University, Faculty of Physics,400084 Cluj, Kogălniceanu str. nr. 1, Romania

3.2 Energy Losses of Swift Protons to Hydrogen Atoms

K. Tőkési , Z-.J. Ding[a)], Z.M. Zhang[a)]

Full and reduced three-body classical trajectory Monte Carlo (CTMC) theory are used to calculate energy losses of the projectile in proton-hydrogen atom collisions as a function of impact energy.

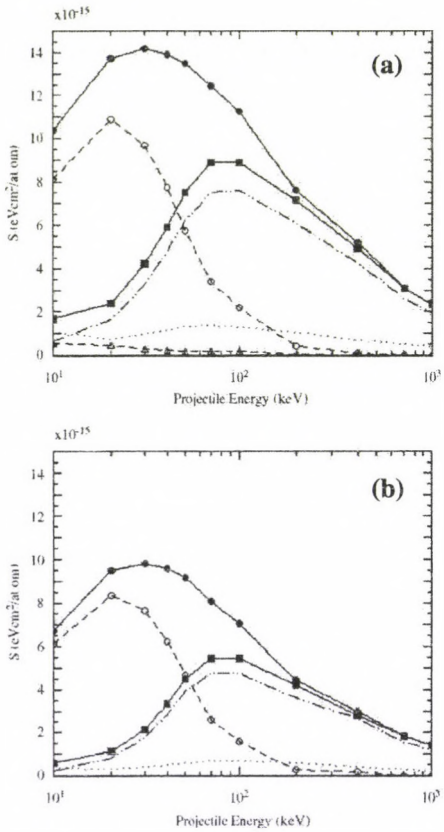

Figure 1. Results of CTMC calculations of the partial and the total stopping power for protons passing through hydrogen targets as a function of projectile energy. (a) Full 3-body, (b) reduced (V[P-T]=0) 3-body CTMC calculations. Dotted line: Excitation; Double-dot-dashed line: Ionization; Dashed line with circle: Capture; Dashed line with triangle: "target exchange", correspond to the knock on collision; Solid line with closed square: Ionization and Excitation; Solid line with closed circle: Sum of all channels.

The total stopping power is presented along with partial contributions of the energy deposition among the channels of excitation, ionization and capture (see Fig. 1). Contributions of the projectile-electron and projectile-target nucleus interactions to the total stopping power are also investigated. In Fig 2. our full 3-body CTMC results are compared with experimental data. The present calculations verify that high order effects should be included for a proper description of the electronic stopping power.

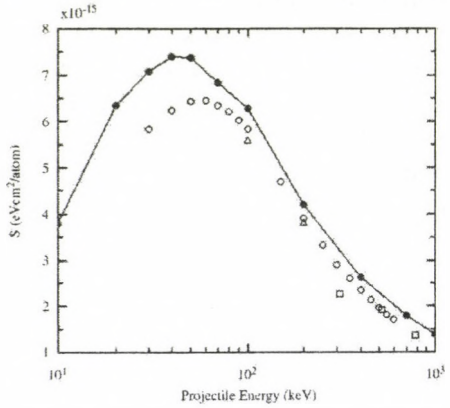

Figure 2. Present full 3-body CTMC results (Solid line with closed circle) for the stopping of protons in atomic hydrogen targets where the projectile scattering angles are restricted to those corresponding approximately to measured angles, compared with experimental data. Experiments: circle: [1], triangle: [2], square: [3].

Acknowledgements

This work was partially supported by the National Natural Science Foundation of China (Grant No. 10025420 and 90206009), the Hungarian Scientific Research Found OTKA No. T046095, the grant "Bolyai" from the Hungarian Academy of Sciences, and TéT Grant No. CHN-3/2004.

a) Hefei National Laboratory for Physical Sciences at Microscale and Department of Physics, University of Science and Technology of China, Hefei, Anhui 230026, P.R. China

[1] H.K. Reynolds et al, 1953. Phys. Rev. 92, 742.

[2] E. Bonderup, P. Hvelplund, 1971. Phys. Rev. A4, 562.

[3] R.A. Langley, 1975. Phys. Rev. B12, 3575.

3.3 Classical descriptions of the electron trajectories in the He atom

Á. Mikó, K. Tőkési

The classical-trajectory Monte Carlo method (CTMC) treats the atomic systems as small solar-systems, where the electrons are moving around the nucleus in properly chosen Kepler-orbits. It is also well known that the multi-electron classical atomic systems are instable due to the autoionization through electron-electron interactions. Therefore most of the classical descriptions use the so called independent particle approach, i.e. they neclect the electron-electron interactions.

In the quasiclassical trajectory Monte Carlo method (QCTMC) appears a qualitative improvement of the classical description of the multi-electron atoms namely the electron-electron interaction is entirely taken into account by the help of the extra potentials providing the validations of the Pauli exclusion principle and the Heisenberg uncertainty principle. The extra potentials ensure that the multi electron atoms are stable even if all electron-electron interactions are taken into account. The extra potentials – representing the constrains – can be written in the following form [1]

$$V = r^{-2} f(rp, \xi),$$

where f is the monotonic decreasing function of the relative distance r and momentum p and ξ is the constant characterized the given atomic state. Figure 1. shows the typical electron trajectories in the helium atom. The calculations were carried out using CTMC model when the electron-electron interaction is neglected (Fig. 1a). In this case the He atom is stable and the electron orbits are closed. However, when the electron-electron interaction is taken into account in the CTMC model the electron trajectories in the He atom show chaotic behavior and after a few cycles autoionization occurs (Fig. 1b). In the QCTMC model the electron trajectories are also closed and stable (Fig. 1c).

Acknowledgements

The work was supported by the grant "Bolyai" from the Hungarian Academy of Sciences, and the National Office for Research and Technology.

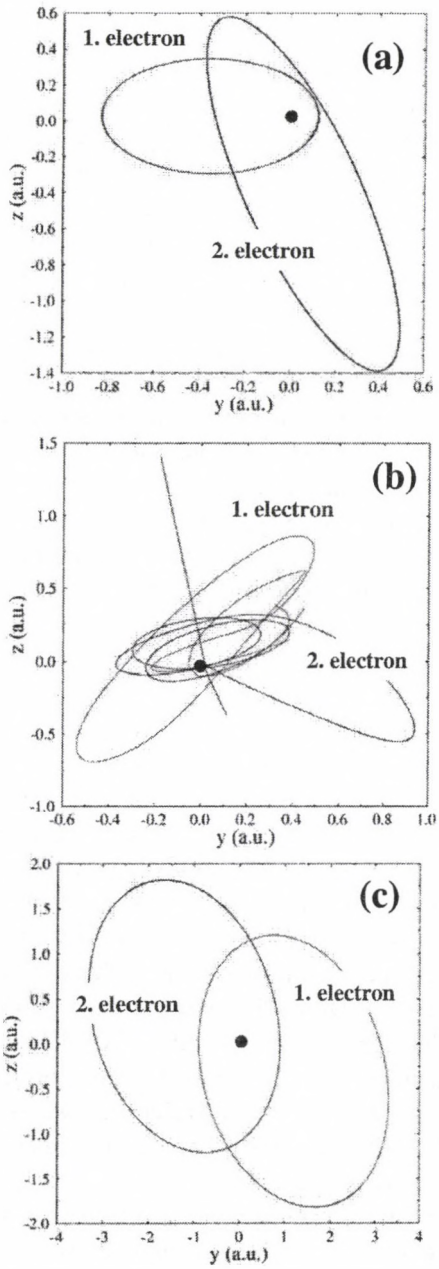

Figure 1. Classical electron trajectories in the He atom. a) CTMC calculation when the electron-electron interaction is neglected, b) CTMC calculation when the electron-electron interaction is taken into account, c) QCTMC results.

[1] C. L. Kirschbaum and L. Wilets, Phys. Rev. **A21**, (1980) 834

3.4 Experimental study of the two-electron correlation in the double continuum state of the He atom

L. Sarkadi and A. Orbán

The developments of the last years in the field of ion-atom collisions are related to the determination of multiply differential quantities. Our present interest is focused on the behavior of two low-energy continuum electrons in the presence of a positive ion. The problem is interesting from fundamental point of view because (i) it is a threshold phenomenon, (ii) the interaction between the particles is the long-range Coulomb force. In collisions such a state can be observed, for example, by simultaneous detection of two electrons ejected in the forward direction with about the same velocity as that of the projectile. Our primary question is whether the outgoing charged projectile is capable to attract more than one low-energy electron (in the projectile reference frame), i.e., the electron cusp exists also in this two-electron case.

To answer the above question, we measure the energy of the simultaneously emitted two electrons with our new time-of-flight spectrometer [1] detecting the electrons in coincidence with the charge-state analyzed scattered projectile to identify the process that results in the three particles in final state. The first very preliminary results have been obtained for 200 keV He^0 + He collision using the 1 MeV VdG accelerator of the Institute. We detected coincidences with the outgoing He^+ ion, i.e., we observed the process in which the two electrons originated from the simultaneous ionization of the projectile and the target.

In fig. 1 the spectra obtained from the triple coincidence measurement clearly show the presence of cusp. In parts a) and b) the energy distributions of the electron e_1 are seen for two different coincidence energy windows for electron e_2. In both cases a definite shift of the peak is visible relative to the cusp of the single ionization process. The direction of the shift depends on the energy of e_2: The peak is shifted to higher energies when the energy of e_2 is fixed on the left hand side of the cusp, and vice versa. The opposite shifts are clear manifestation of the repulsive Coulomb-interaction between the two ejected electrons. Further measurements are going on and are also planned to map accurately the energy sharing between the two ejected electrons.

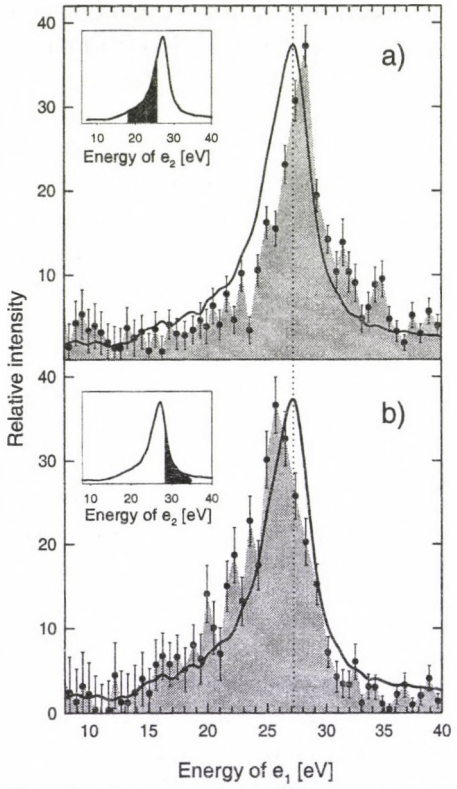

Figure 1. Electron spectra measured at 0° for 200 keV He^0 + He collision. Solid line: coincident detection of the electron e_1 with the outgoing He^+ ion (single ionization of the projectile). Full circles: coincident detection of the electrons e_1 and e_2 with the outgoing He^+ ion (simultaneous ionization of the projectile and the target). The intensities are normalized at the cusp maximum. The insets show the coincidence windows. For spectrum a) the energy of e_2 was fixed in the energy range 18-26 eV, while for spectrum b) the energy range of e_2 was 28-36 eV.

[1] L. Sarkadi and A. Orbán, Meas. Sci. Technol. 17 (2006) 84-90.

3.5 Left-right asymmetry in outer s-shell photoionization

T. Ricsóka, S. Ricz, Á. Kövér, D. Varga, M. Huttula[a)], S. Urpelainen[a)], H. Aksela[a)], S. Aksela[a)]

In the quantum mechanical picture of the atomic ionization/excitation and rearrangement processes the parity is conserved. This means that the left and right side intensities in the angular distribution of the emitted particles are identical. The left-right asymmetry parameter can be determined in the following way:

$$A_{LR} = \frac{\sigma_L - \sigma_R}{\sigma_L + \sigma_R} = 2Re(A_{PV}/A_{EM}),$$

where σ_L and σ_R are the left and right hand side cross sections, A_{PV} and A_{EM} represent the transition matrix elements of the parity violating (PV) and of the electromagnetic interactions (EM), respectively. The non-zero value of A_{LR} indicates that the parity is violated in the considered process [1]. The geometrical definition of the left and right sides can be seen on Fig. 1. The mirroring plane is perpendicular to the polarization direction of the photon beam.

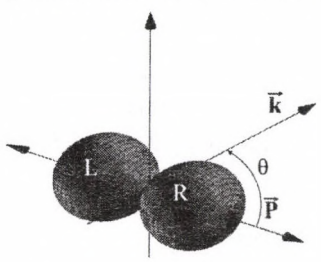

Figure 1. Geometrical definition of the left (L) and right (R) sides and the spatial distribution of photoelectrons in case of linearly polarized light at $\beta = 2$ dipole parameter. $\vec{k}$ and $\vec{P}$ are the momentum and polarization vectors of the incoming photon, respectively, and θ is the polar angle in the measuring plane ($\vec{k}$, $\vec{P}$ plane).

In atomic physics the parity non-conservation (PNC) has been observed only in a few cases (see the overview articles [1-3] and references therein). The parity violation was measured in the resonant photoexcitation processes of the valence electrons by linearly and circularly polarized laser light [4-7]. The PNC was explained in the frame of the Standard Model (SM).

The double differential cross sections of outer s-shells photoelectrons have been measured for noble gases He, Ne, Ar, Kr, Xe and for H_2 molecule by linearly polarized synchrotron radiation in the 220.4 – 255.5 eV photon energy range in order to determine the left-right asymmetry parameters. The experiment was carried out at the beamline I411 on the third generation MAX-II storage ring in Max-Lab, Lund, Sweden [8] during two different beamtimes. Linear polarization of the photon beam was better than 98% [8, 9].

The emitted electrons were analyzed with ESA-22 electronspectrometer [10]. The unique capability of the $ESA-22$ electron spectrometer is to measure the total angular range (15°- 345°) of emitted electrons simultaneously, therefore the confidence in the pattern of the angular distribution is very high. Any instabilities in the photon flux or in the density of the target atoms produce the same effect at all angles.

The relative efficiencies of the detectors were determined by measuring the Ar $L_2 - M_{2,3}M_{2,3}\ ^3P_{0,1,2}$ diagram Auger transitions at the average kinetic energy of 207.0 eV [14] at 400 eV photon energy. All spectra were normalized to this isotropic Auger electron line. Photoelectrons ejected from the outer s-shells were collected at around the kinetic energy of 207.0 eV so that the possible effect of retardation is reduced. The deceleration ratios (E_{kin}/E_{pass}) were varied between 4.83 – 5.31 during the measurements at 40 eV pass energy (E_{pass}) of the spectrometer.

In order to exclude any possible systematic instrumental effects the spectrometer and vacuum chamber were rotated by 180°. A non-zero left-right asymmetry has been observed relative to the mirroring plane before and after the rotation of the equipment by 180°. The values of the measured asymmetry parameters are displayed in Fig. 2. as a function of the atomic mass. The agreement among the three data sets is very good, except for Xe. The figure

clearly shows that the asymmetry parameters differ from zero and increase with decreasing nuclear mass.

As far as we know no experimental investigations and theoretical predictions have been published for the left-right asymmetry in photoionization. The existing quantum mechanical and quantum electrodynamical descriptions cannot explain our findings. As it was mentioned the non-zero value of the asymmetry parameter indicates the break down of the parity conservation in photoionization. In atomic photoexcitation the origin of the parity violation was explained in the frame of the Standard Model as the interaction between the atomic electrons and nucleons via the neutral weak current ([1-3] and the citations in therein).

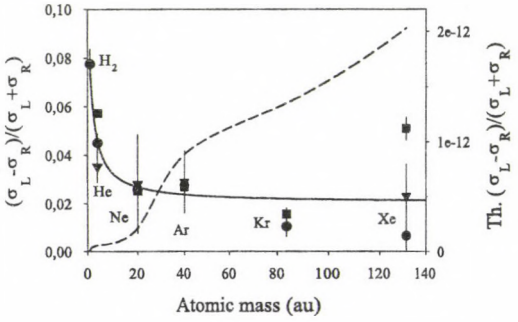

Figure 2. The experimental and theoretical s-shell left-right asymmetry parameters as a function of the atomic mass for H_2 molecule and for the noble gases from He to Xe. The circles show the first measurement, the squares are the reproduction of data a half year later and the triangles represent the asymmetry parameters after the rotation of the whole system by 180°. (The solid line is drawn to guide the eye.) The dashed line and right hand scale denote the theoretical estimation of the left-right asymmetry parameters.

We used similar description for the calculation of the asymmetry parameters for photoionization. A first order non-relativistic independent particle model was applied for the theoretical estimation of the left-right asymmetry parameters for photoionization. The initial and final states of atomic electrons were represented by hydrogen-like wave functions in both the parity violating (A_{PV}) and the parity conserving transition amplitudes (A_{EM}). The parity non-conserving interaction potential was reduced only for the spin independent part (see Eq. 10 in [1]) and dipole approximation was applied for the photoionization [11]. The estimation of the left-right asymmetry parameters is plotted on Fig. 2 with dashed line (with right side scale). As it is seen the order of magnitude and the tendency of the calculated data are in contradiction with the measured one. The disagreement indicates that the observed non-zero asymmetry cannot originate from the weak interaction among the atomic electrons and nucleons. This is true especially for H_2 molecule where the theory predicts very small value for the asymmetry parameter and the experiment shows a maximum.

This is the first observation for the left-right asymmetry in the double differential cross section of the s-shell photoionization.

Acknowledgements

We thank the staff of MAX-laboratory for assistance during the measurements. This work was supported by the Research Council for Natural Sciences and Technology of the Academy of Finland and by the Hungarian Scientific Research Foundation (OTKA Grant No: T037203).

a) Univ. of Oulu, Dept. of Physical Sciences, P.O. Box 3000, 90014, Oulu, Finland

[1] M. A. Bouchiat and C. Bouchiat, Rep. Prog. Phys. **60** 1351 (1997).

[2] J. S. M. Ginges and V. V. Flambaum, Phys. Rep. **397** 63 (2004).

[3] G. W. Botz, D. Bruss and O. Nachtmann, Ann. Phys. **240** 107 (1995).

[4] C. S. Wood *et al.*, Science **275** 1759 (1997).

[5] N. H. Edwards, S. J. Phipp, P. E. G. Baird and S. Nakayama, Phys. Rev. Lett. **74** 2654 (1995).

[6] S. J. Phipp, N. H. Edwards, P. E. G. Baird and S. Nakayama, J. Phys. B **29** 1861 (1996).

[7] M. J. D Macpherson *et al.*, Phys. Rev. Lett. **67** 2784 (1991).

[8] M. Bässler *et al.*, Nucl. Instr. and Meth. A **469**, 382 (2001).

[9] R. Sankari, S. Ricz, Á. Kövér, M. Jurvansuu, D. Varga, J. Nikkinen, T. Ricsóka, H. Aksela and S. Aksela, Phys. Rev. A **69** 012707 (2004).

[10] S. Ricz, Á. Kövér, M. Jurvansuu, D. Varga, J. Molnár, and S. Aksela, Phys. Rev. A **65**, 042707 (2002).

[11] Jwei-Jun Chang, Phys. Rev. A **57**, 717 (1998).

3.6 Observation of left-right asymmetry in outer p-shell photoionization

T. Ricsóka, S. Ricz, Á. Kövér, D. Varga, M. Huttula[a)], S. Urpelainen[a)], H. Aksela[a)], S. Aksela[a)]

In the electromagnetic interaction the parity is conserved, i.e. all processes are invariant for the mirroring of the coordinate system. The left-right asymmetry parameter can be determined in the following way:

$$A_{LR} = \frac{\sigma_L - \sigma_R}{\sigma_L + \sigma_R} = 2Re(A_{PV}/A_{EM}),$$

where σ_L and σ_R are the left and right hand side cross sections, A_{PV} and A_{EM} represent the transition matrix elements of the parity violating (PV) and of the electromagnetic interactions (EM), respectively. The non-zero value of A_{LR} indicates that the parity is violated (PV) in the considered process [1]. The geometrical definition of the left and right sides see on Fig. 1 in the present Annual Report for s-shells.

The parity non-conservation (PNC) in atomic process has been observed for a few heavy atoms [2-5]. The parity violation (PV) was explained in the frame of the Standard Model (SM) as the result of the electroweak interaction between the nucleus and atomic electrons mediated by the exchange of Z_0 boson.

The double differential cross sections of outer p-shells photoelectrons have been measured for noble gases Ne, Ar, Kr and Xe by linearly polarized synchrotron radiation in order to determine the left-right asymmetry parameters. The present investigations were carried out at the beam line I411 of the third generation MAX-II storage ring at Max-lab, Lund, Sweden [6]. Linear polarization of the photon beam was better than 98% [6, 7]. In the present measurement the exit slit of 200 μm was used in the monochromator and the bandwidth of the photon beam was about 0.5 eV. The effect of the different slit size on the left-right asymmetry was tested with $3p$ photoelectrons of argon. A_{LR} was found to remain constant within 2.5% when the width of the exit slit was changed in the range of $50-200$ μm. The incident photon energy range was $220.4-228.7$ eV in the measurement. Argon $2p$ photoelectrons were measured to test the experimental setup (including the beam line and the spectrometer system) at photon energy of 461.2 eV and slit size of 60 μm. The high-resolution settings allowed us to separate the spin-orbit components of the Ar $2p$ photoelectron lines.

The electrons from emitted the collision region were analyzed with ESA-22 electronspectrometer [8]. The emission angles of the electrons are conserved from the target to the detectors due to the applied radial electrostatic field. The photoelectrons were detected by channeltrons in the plane determined by the momentum and the electric vectors of the incoming photon beam at 20 polar angles (15°-345°) relative to the polarization vector. The energy and angular distributions of the Auger- and photoelectrons were measured at the pass energy (E_{pass}) 40 eV and the energy resolution of the analyzer was 90 meV full width at half maximum (FWHM).

The double differential cross sections of the photoelectrons was determined relative to the Ar $L_2 - M_{2,3}M_{2,3}$ $^3P_{0,1,2}$ Auger production cross sections. The energy of these Auger-lines is 207.0 eV [8]. In case the measurement of Auger lines the photon energy was 400 eV. In order to reduce the possible effect of retardation, all photoelectrons ejected form the outer p-shells were collected at the kinetic energy of the $^3P_{0,1,2}$ Auger-electrons.

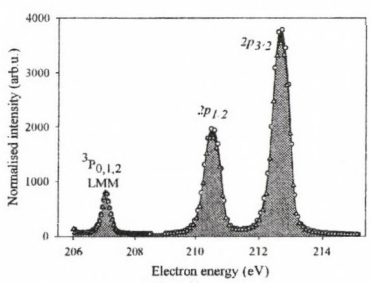

Figure 1. Comparison between the left (black circle and black shaded peak area) and right (triangle and gray shaded peak area) side $2p_{1/2}$ and $2p_{3/2}$ photoelectron spectra of Ar after the normalization for the corresponding area of the $^3P_{0,1,2}$ Auger line.

The Ar $2p$ photoelectron line and the Ar LMM Auger peak were measured in the same spectrum. A photon energy of 461.2 eV was used to bring the Auger and photoelectron lines close to each other. Fig. 1 shows the comparison between the left (black circle and black shaded peak area) and right (triangle and gray shaded peak area) side spectra normalized to the corresponding isotropic Auger line. The left-right asymmetry is clearly seen. The values of the asymmetry parameters were found to be $A_{LR}^{1/2} = 0.015(10)$ and $A_{LR}^{3/2} = 0.0094(90)$ for the fine structure components of Ar $2p$ photoelectrons (the numbers in the brackets show the errors).

As a check the asymmetry parameters for the Ar $2p$ line were also measured by two Scienta analyzers (SES-100 and SES-200) at the beam line I411 at several angels. The angular distribution of the photoelectrons was measured simultaneously by both analyzers (one of them was on the left side and the other one on the right side) and the analyzers were rotated in the dipole plane keeping the same angles. The measured asymmetry parameter of $A_{LR}^{Sc} = 0.010(3)$ is in good agreement with the value obtained with $ESA - 22$ spectrometer. This observation strongly confirms that the left-right asymmetry is the result of a real physical process and it cannot be interpreted as any instrumental effect.

The values of the measured asymmetry parameters are displayed in Fig. 2. as a function of the atomic mass.

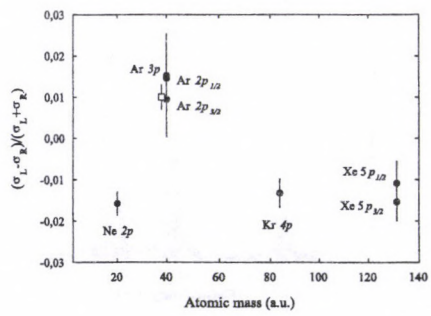

Figure 2. The p-shell experimental left-right asymmetry parameters for the meausrements with both ESA-22 (solid circles) and two Scienta (open square) electronspectrometer as a function of the atomic mass for the noble gases from Ne to Xe.

The asymmetry parameters are approximately independent from the atomic mass and they are opposite sign relative to the s-shells, except Ar $2p$- and $3p$-shells where the channel interaction between the ionization and excitation is strong [9]. The opposite sign of asymmetry among the s- and p-shells confirms that the non-zero asymmetry parameters are the results of a real physical process.

This is the first observation for the left-right asymmetry in the double differential cross section of the p-shell photoionization.

Acknowledgements

We thank the staff of MAX-laboratory for assistance during the measurements. This work was supported by the Research Council for Natural Sciences and Technology of the Academy of Finland and by the Hungarian Scientific Research Foundation (OTKA Grant No: T037203).

a) Univ. of Oulu, Dept. of Physical Sciences, P.O. Box 3000, 90014, Oulu, Finland

[1] M. A. Bouchiat and C. Bouchiat, Rep. Prog. Phys. **60** 1351 (1997).

[2] J. Guéna, D. Chauvat, Ph. Jacquier, E. Jahier, M. Lintz, S. Sanguinetti, A. Wasan, M. A. Bouchiat, A. V. Papoyan and D. Sarkisyan, Phys. Rev. Lett. **90** 143001 (2003).

[3] P. A. Vetter, D. M. Meekhof, P. K. Majumder, S. K. Lamoreux, E. N. Fortson, Phys. Rev. Lett. **74** 2658 (1995).

[4] D. M. Meekhof, P. A. Vetter, P. K. Majumder, S. K. Lamoreux, E. N. Fortson, Phys. Rev. Lett. **71** 3442 (1993).

[5] M. J. D Macpherson, K. P. Zetie, R. B. Warrington, D. N. Stacey and J. P. Hoare, Phys. Rev. Lett. **67** 2784 (1991).

[6] M. Bässler, A. Ausmees, M. Jurvansuu, R. Feifel, J-O. Forsell, P. de Tarso Fonseca, A. Kivimäki, S. Sundin, S. L. Sorensen, R. Nyholm, O. Björneholm, S. Aksela, and S. Svensson, Nucl. Instr. and Meth. A **469**, 382 (2001).

[7] R. Sankari, S. Ricz, Á. Kövér, M. Jurvansuu, D. Varga, J. Nikkinen, T. Ricsóka, H. Aksela and S. Aksela, Phys. Rev. A **69** 012707 (2004).

[8] S. Ricz, Á. Kövér, M. Jurvansuu, D. Varga, J. Molnár, and S. Aksela, Phys. Rev. A **65**, 042707 (2002).

[9] S. Ricz, J. Nikkinen, R. Sankari, T. Ricsóka, Á. Kövér, D. Varga, S. Fritzsche, H. Aksela and S. Aksela, Phys. Rev. A **72** 014701 (2005).

3.7 Simulation of ion guiding through insulating capillaries: effects of inter-capillary interaction

K. Schiessl[a)], W. Palfinger[a)], K. Tőkési , H. Nowotny[a)], C. Lemell[a)], J. Burgdörfer[a)]

Nanocapillaries through insulating foils have received interest as a target for beams of slow highly-charged ions. Transmission of projectiles in their initial charge state have been measured for angles of incidence larger than the geometrical opening angle. Ions are guided along the capillary axis and do not closely interact with the inner walls of the capillary. We have developed a classical trajectory transport theory of this self-organized guiding process that relates the microscopic charge-up with macroscopic material properties and includes multi-capillary effects on a phenomenological level.

In this work simulations for ion guiding through insulating nanocapillaries within the framework of a mean-field classical transport theory are presented. We combine a microscopic trajectory simulation with macroscopic material properties for bulk an surface conductivities of highly insulating materials. Projectiles hitting the inner wall of the insulating material in the early stage of the irradiation deposit their charge on the capillary surface. These charges diffuse along the surface and, eventually, into the bulk due to the small but finite surface and bulk conductivities of the insulator. Projectiles entering the capillary at a later stage are deflected by the Coulomb field of a self-organized charge patch close to the entrance of the capillary. Invoking this scenario we are able to reproduce a range of experimental findings, e.g. ion guiding even for large incidence angles. We have shown that these results can be interpreted on the basis of a linear model including transport of deposited charges along the surface without resorting to freely adjustable parameters. Approximate inclusion of multi-capillary effects [1] further improve the microscopic simulation and show the same qualitative dependence on ion energy or angle of incidence as the experiment (see Fig. 1).

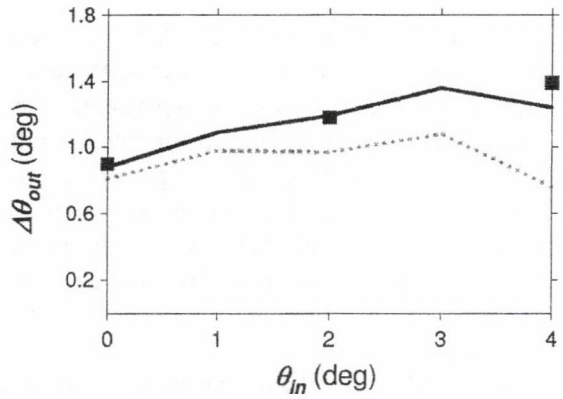

Figure 1. Experimental (squares, [2]) and simulated (dotted line) angular spread of 3.5 keV Ne^{7+} ions transmitted through Mylar nanocapillaries with a diameter of 200nm. The solid curve is obtained by including the defocussing force originating from the ensemble of all charged capillaries situated in the beam spot.

Acknowledgements

We thank Y. Yamazaki for making results available to us prior to publication. The work was supported by the grant "Bolyai" from the Hungarian Academy of Sciences, the TeT Grant No. A-15/04, the Austrian Fonds zur Förderung der wissenschaftlichen Forschung, FWF-SFB016 "ADLIS" and by the EU under contract No. HPRI-CT-2001-50036.

a) Institute for Theoretical Physics, Vienna University of Technology, A-1040 Vienna, Austria, EU

[1] K. Schiessl, W. Palfinger, K. Tőkési, H. Nowotny, C. Lemell, J. Burgdörfer, Nucl. Instrum. Meth. Phys. Res. B, in press.

[2] Y. Kanai, M. Hoshino, T. Kambara, Y. Yamazaki, R. Hellhammer, and N. Stolterfoht, Contribution to the XXIVth ICPEAC, Rosario, Argentina (2005) and Y. Yamazaki, *private communication* (2006).

3.8 Transmission of Ne^{6+} ions through Al_2O_3 capillaries

Z. Juhász, B. Sulik, Gy. Vikor, S. Biri, É. Fekete, I. Iván, F. Gáll, K. Tőkési, S. Mátéfi-Tempfli[a], M. Mátéfi-Tempfli[a], E. Takács[b], J. Pálinkás[b]

Insulating nanocapillaries have attracted considerable attention since the discovery of capillary guiding[1]. Recent experiments have shown that slow charged projectiles (highly charged ions and electrons) are guided through nanocapillaries avoiding collisions with the capillary walls. Collecting experimental data with different kind of materials is of great importance for the understanding of the phenomenon.

In 2006, we have performed systematic measurements with Al_2O_3 capillaries at ATOMKI, Debrecen. We extended our earlier experiments, in which we observed that 3 keV Ne^{6+} ions were efficiently guided by Al_2O_3 capillaries [2]. Angular distribution of the transmitted ions, tilt angle, time, and energy dependences(in the 3-90 keV energy range) of the transmission have been measured with two capillary samples with 140 and 260 nm capillary diameters.

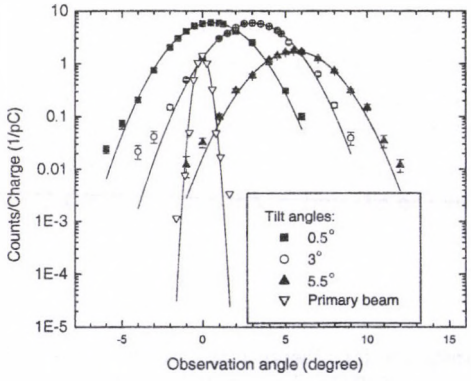

Figure 1. Angular distribution of 3 keV Ne^{6+} ions transmitted through nanocapillaries of Al_2O_3 with capillary diameter of d=140 nm. The capillaries were tilted as indicated in the figure. Solid lines represent Gaussian fit to the data.

We observed significant transmission up to 7.5° tilt angle of the samples. The centroids of the angular distributions of the transmitted ions coincided with the tilt angle as signature of the ion guiding. The FWHMs were about 4° and were nearly independent of the tilt angle and the capillary diameter. These observations are rather similar to earlier observations for polyethylene terephthalate (PET) capillary samples by Stoltefoht et al [1].

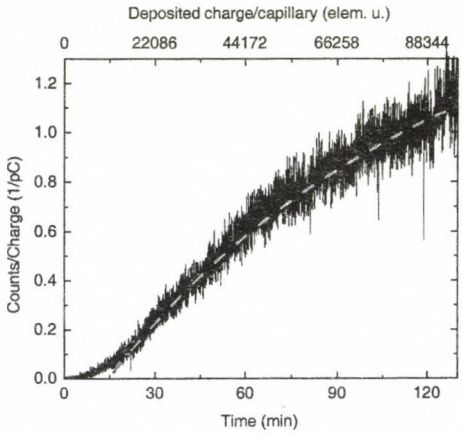

Figure 2. The time dependence of the transmitted Ne^{6+} intensity through capillaries with d=140 nm. The tilt and observation angles were the same (5°). Dashed gray curve is exponential fit.

At the beginning of each set of measurements the time dependence of the transmission was measured. Stationary transmission was reached after a few tens of minutes characteristic charge up time. The time constant was much larger for the sample with the smaller capillary diameter. Both of our Al_2O_3 samples charged up much slower than the PET samples in previous observations. This is probably due to the larger dielectric constant for Al_2O_3. In the transmitted intensity there are significant fluctuations. It is interesting that the relative fluctuations do not decrease as the intensity increases. This is the sign that the transmission is a result of a dynamic equilibrium between charging and discharging processes. Some of the capillaries may become overcharged, that

hamper further ions to enter and pass the overcharged capillaries and their neighbors. Therefore the discharging processes start to dominate in those capillaries, so the capillaries open up later on.

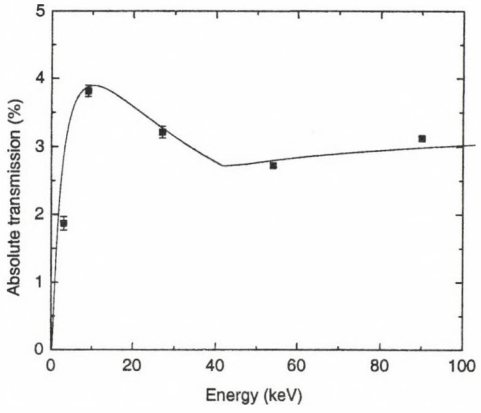

Figure 3. Transmission Ne^{6+} ions ($I_{transmitted}/I_{primary}$) at 0° tilt angle as function of the ion energy (d=260 nm). The solid line repesents calculated transmissions.

We measured the stationary transmission at different ion energies. The transmitted fractions of the ions were much lower than that can be expected from the geometrical opening of the samples. Taking into account the deviations from the ideal geometry and the mirror charge attraction the reduced transmission and its dependence on the ion energy can be understood.

Acknowledgements

This work was supported by the Hungarian National Science Foundation OTKA (Grant No's: T046905, T046454, T042729 and PD050000), and in part by the Belgian Science Policy through the Interuniversity Attraction Pole Program IAP (P5/1/1).

a) Unité de Physico-Chimie et de Physique des Matériaux, Université Catholique de Louvain, Place Croix du Sud, 1, 1348-Louvain-la-Neuve, Belgium

b) Department of Experimental Physics, University of Deberecen, Egyetem tér 1, H-4032 Debrecen, Hungary

[1] N. Stolterfoht, J.-H. Bremer, V. Hoffmann, R. Hellhammer,D. Fink, A. Petrov, and B. Sulik, Phys. Rev. Lett. **88** (2002) 133201-1.

[2] S. Mátéfi-Tempfli et. al. Nanotechnology **17**, 3915 (2006).

3.9 Anisotropy in highly charged ion induced molecule fragmentation

Z. Juhász, B. Sulik, F. Frémont[a)], J.-Y. Chesnel[a)], A. Hajaji[a)]

Studying fragmentation processes of biologically relevant molecules due to highly charged ion impact is important to understand radiation damage in biological tissues. Energy spectra of the charged molecule fragments may reveal the different fragmentation patterns meanwhile the angular distributions of the fragments characterize the dependence of fragmentation probability on the initial orientation of the molecule. The research to explore the angular distribution of the molecule fragments has only recently been started[1].

In 2006 we performed measurements at ARIBE facility at GANIL, Caen (France), in order to investigate orientation effects in molecule fragmentation. Fragmentation of H_2O, C_6H_6 and CH_4, which represent different level of symmetry, have been studied by 60 keV N^{6+} ion impact. Energy spectra of the charged fragments at different observation angles have been taken.

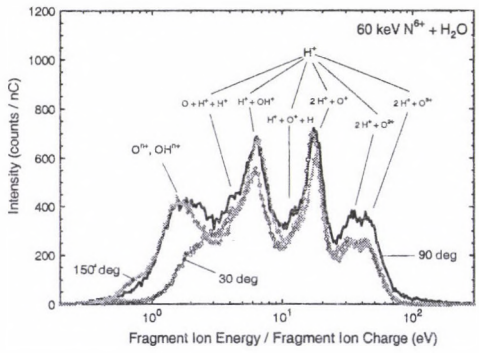

Figure 1. Energy spectra of protonic and heavy fragments in collisions of 60 keV N^{6+} and H_2O.

As our example spectra show the different protonic peaks can be attributed to different fragmentation processes. Significant anisotropy can be seen in the different processes.

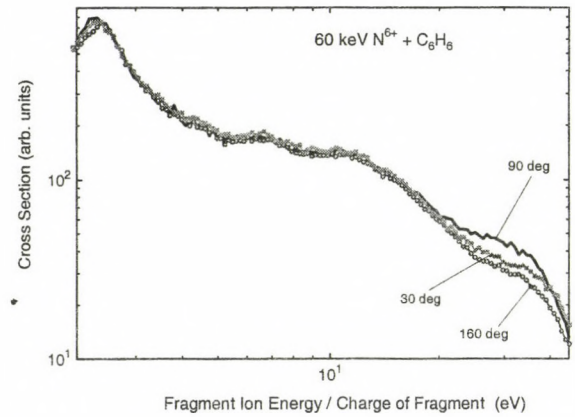

Figure 2. Energy spectra of protonic and heavy fragments in collisions of 60 keV N^{6+} and C_6H_6.

The strongest evidence for the anisotropy can be seen in the spectra of C_6H_6, where the spectra appear isotropic in almost the whole observed energy range except one peak, which has a strong angular dependence and is maximal around 90°.

Acknowledgements

This experiment has been performed at the distributed LEIF-Infrastructure at ARIBE, GANIL, France, supported by Transnational Access granted by the European Project HPRI-CT-2005-026015. The work was supported by the Hungarian National Science Foundation OTKA (Grant No's: T046905 and PD050000).

a) CIRIL Unité Mixte CEA-CNRS-EnsiCaen-Université de Caen Basse-Normandie, F-14050 Caen Cedex 04, France

[1] P. Sobocinski, Z. D. Pešić, R. Hellhammer, D. Klein, B. Sulik, J.-Y. Chesnel and N. Stolterfoht, J. Phys. B **39** (2006) 927.

3.10 Target dependence of charge exchange X-rays

E. Takács[a,b], K. Tőkési, H. Tawara[a,c], C.J. Verzani[d], T. Hohl[b], J.D. Gillaspy[a], J. Pálinkás[b]

X-rays emitted in a series of cascade transitions after electron capture into high Rydberg states of ions have been the central topic of recent astrophysical observations [1]. The current interpretation for the source of these x-rays is that they originate from highly charged ions of the solar wind picking up electrons from neutral atomic/molecular species in the comas of comets, and also from the atmospheres of planets [2]. In order to investigate x-ray spectra from such a charge exchange process that is followed by the cascade of electrons, a series of laboratory investigations of K, L and M x-rays emitted by highly charged ions colliding with various neutral targets have been carried out at NIST [3]. Previous findings have illustrated the importance of multiple electron capture in bare and few electron projectile-ions. Other groups have also made progress in this field studying different collision systems both experimentally [4] and theoretically [5]. In this work we focus on the target dependence of the L and M x-ray emission spectra produced in Kr^{q+} (q=27, 28, and 31) projectiles colliding with various neutral gases. The observed emission lines appear only after a long sequence of cascades originating from Rydberg (n,l) states onto which the initial electron is captured. Such variations among different target gases is expected, as it is known that the initial Rydberg state distributions depend strongly on the ionization energy of the target (EB) as well as the ion charge (q). The dependence on target gases can be used in some applications, as reported previously [6].

Full understanding of the observed x-ray spectrum will require, in addition to the precise knowledge of the initial (n, l) population distributions that was also calculated in the present work, atomic structure calculations for the transition probabilities and their branching ratios between the levels involved in the cascade processes. Work towards these calculations is in progress.

Acknowledgements

This work was partially supported by grants from the Hungarian Science Fund (No: OTKA T046454), by NASA EPSCoR Grant NCC5-601 through the University of Connecticut, and by the U.S. Department of Energy, and the grant "Bolyai" from the Hungarian Academy of Sciences

a) National Institute of Standards and Technology, Gaithersburg, MD, USA

b) University of Debrecen, Experimental Physics Department, Debrecen, Hungary

c) Max Planck Institute for Nuclear Physics, Saupfercheckweg 1, Heidelberg, Germany

d) Physics Department, University of Connecticut, Storrs, CT, USA

[1] C.M. Lisse, D.J. Christian, K. Dennerl, K.J. Meech, R. Petre, H.A. Weaver, and S.J. Wolk, Science 292 (2001) 1343.

[2] T.E. Cravens, Science 296 (2002) 1042.

[3] H. Tawara, E. Takács, L.P. Ratliff, J.D. Gillaspy, and K. Tőkési, Nucl. Instr. and Meth. B. 205 (2003) 605.

[4] J.B. Greenwood, I.D. Williams, S.J. Smith, and A. Chutjian, Phys. Rev. A 63 (2001) 062707.

[5] V. Kharchenko and A. Dalgarno, J. Geophys. Res. 105 (2000) 18351.

[6] P. Beiersdorfer, K.R. Boyce, G.V. Brown, H. Chen, S.M. Kahn, R.L. Kelley, M. May, R.E. Olson, F.S. Porter, C.K. Stahle, and W.A. Tillotson, Science 300 (2003) 1558.

4.1 Ni KLL Auger spectra photoexcited from Ni nanofilms

L. Kövér, I. Cserny, W. Drube[a], M. Novák and S. Egri[b]

Photon-induced KLL Auger spectra of 3d metals are important for understanding excitation processes associated with K-shell hole creation as well as the role of the local density of the unoccupied electronic states (around the atom excited) in these excitation processes using resonant and non-resonant conditions [1-4]. Extracting electronic structure information from Auger spectra of solids, however, is difficult because of the electron scattering processes in the material. A comparison between Auger spectra excited from a bulk metal to that emitted from an ultrathin layer is very helpful and sheds light on the effects distorting the spectral shapes due to multiple bulk and surface scattering of the signal electrons during their transport within the solid. For the present studies a high purity polycrystalline Ni sheet was used as thick sample, while the nano-film sample of less than 1 nm thickness was obtained by in situ electron beam evaporation of Ni onto a glassy carbon wafer. High energy resolution measurements of the Ni KLL Auger spectra photoexcited from both samples were performed with the Tunable High Energy XPS (THE XPS) instrument [5] at the BW2 beamline (the instrument is equipped with a Scienta SES-200 hemispherical analyzer) using high energy resolution (0.2 eV). The exciting photon beam was focussed onto the samples by a Si (220) monochromator and a proper positive bias voltage was applied on the samples. In the case of the nanolayer sample a grazing angle of incidence photon beam was used. In Fig. 1 the measured Ni KLL spectra are shown, comparing thick sample and nanolayer for non-resonant excitation. For nanolayer spectra, a significant reduction of the inelastic background and a strong increase of the peak to background ratios can be seen, and - in the case of the resonant spectra - an enhancement of the spectral details. In addition, the photoelectron peaks excited by the characteristic X-rays photoinduced internally in the sample, are absent in the case of the nanolayer spectra.

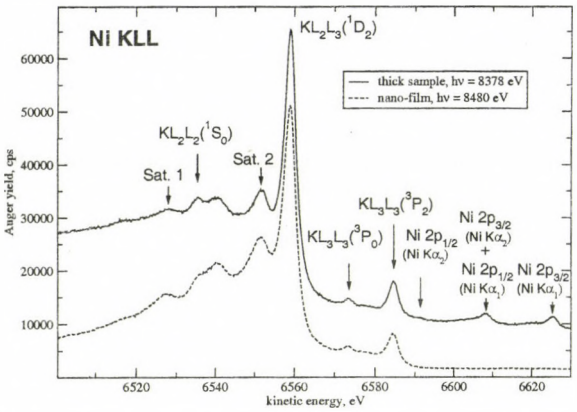

Figure 1. Ni KLL Auger spectra photoexcited from a thick polycrystalline Ni sample (solid line) and from a Ni nanolayer deposited in situ onto a glassy carbon substrate (dashed line), using non resonant conditions (photon energy above the K-shell ionization threshold).

Acknowledgements

This work was supported by the DESY and the European Community under Contract RII3-CT-2004-506008 (IA-SFS).

a) Hamburger Synchrotrostrahlugslabor HASYLAB at Deutsches Elektronen-Synchrotron DESY, Notkestraße 85, D-22603 Hamburg, Germany

b) Department of Experimental Physics, Debrecen University, H-4026 Debrecen, Bem tér 18/a.

[1] L. Kövér, Zs. Kovács, J. Tóth, I. Cserny, D. Varga, P. Weightman and S. Thurgate, Surf. Sci. 433, 833 (1999).

[2] I. Cserny, L. Kövér, H. Nakamatsu and T. Mukoyama, Surf. Interface Anal. 30, 199 (2000).

[3] L. Kövér, Z. Berényi, I. Cserny, L. Lugosi, W. Drube, T. Mukoyama and V. R. R. Medicherla, Phys. Rev. B73, 195101(2006).

[4] L. Kövér, T W. Drube, Z. Berényi, I. Cserny, V. R. R. Medicherla, T. Ishii, H. Ikeno and H. Adachi, Surf. Sci., (in press)

[5] W. Drube, T. M. Grehk, R. Treusch and G. Materlik, J. Electron Spectrosc. Relat. Phenom. 88-91, 683 (1998).

4.2 Field theoretical approach to magnetically coupled layered superconductors

I. Nándori, K. Vad, S. Mészáros, U.D. Jentschura[a], *S. Nagy*[b], *K. Sailer*[b]

High transition temperature superconductors have usually a layered structure. The superconducting layers separated by insulating planes are coupled by magnetic or Josephson coupling. Due to this layered structure the lowest energy topological excitations in these systems are not conducting electrons (which are created from Cooper-pairs) but small supercurrent "rings" which carrie magnetic flux. These are called vortex type excitations.

Vortex dominated properties of magnetically coupled superconducting layered systems have recently been investigated in Ref.[1]. Since the planes are magnetically coupled, the pancake type vortices of single layers can form a Pearl-type vortex stack. However, above a critical temperature, due to the thermal fluctuations, the vortex stack is broken up into a number of pancake vortices of fractional flux. Therefore, this configuration undergoes a phase transition of the Kosterlitz-Thouless-Berezinskii (KTB) type at a layer-dependent critical temperature

$$T_{\rm KTB}^{(N)} = T_{\rm KTB}^{\star} \frac{(N-1)}{N}$$

which is connected with the dissociation of the stack. This result has already been obtained in the literature on the basis of approximative methods, therefore, rigorous renromalization group (RG) analysis has been required to clarify the conjecture. The real space RG study of $N = 2$ layers discussed in Ref.[1] has been assumed to go beyond the previously used approximations but it is based on some a priori assumption and, hence, it loses its predicting power, and it appeared to be rather difficult to generalize for $N > 2$ layers.

In Refs.[2,3,4,5] we open a new platform to consider the vortex dynamics of magnetically coupled layered systems by constructing a multi-layer sine–Gordon (MLSG) type field theoretical model where the two-dimensional sine–Gordon fields characterizing the layers are coupled by an appropriate general mass matrix. The action of the MLSG model reads as

$$S = \int d^2x \left[\frac{1}{2} \sum_{n=1}^{N} (\partial_\mu \phi_n)^2 + V(\phi_1, ..., \phi_N) \right]$$

with the interaction terms

$$V = \frac{1}{2} G \left(\sum_{n=1}^{N} (-1)^{n+1} \phi_n \right)^2 + \sum_{n=1}^{N} y \cos(b\phi_n)$$

where the parameters are the Fourier amplitude y, the frequency b and the coupling strength G. For $N = 1$ the MLSG model reduces to the massive sine-Gordon model. By the exact mapping of the MLSG model into the equivalent gas of topological excitations we recover the interaction potential given in Ref.[1] and, hence, prove the applicability of the model. We analyze the phase structure of the MLSG model by a differential RG method performed in momentum space and determine the layer-dependence of $T_{\rm KTB}^{(N)}$. Our results validate the conjecture obtained by the approximative entropy method. In our field theoretical RG approach, the RG flow can be calculated in one step for an arbitrary number of layers from first principles. We envisage that further investigations of the MLSG model could enrich our understanding of the layered structures, and that of the curious properties of magnetically coupled high-T_c superconductors.

a) Max–Planck–Institut für Kernphysik, Saupfercheckweg 1, 69117 Heidelberg, Germany

b) Department of Theoretical Physics, University of Debrecen, H-4032, Debrecen, Hungary

[1] A. De Col, V. B. Geshkeinbein, G. Blatter, Phys. Rev. Lett. **94** (2005) 097001.

[2] I. Nándori, K. Sailer, Phil. Mag. B**86** (2006) 2033

[3] I. Nándori and K. Vad, J. Opto. Adv. Mat. **8** (2006) 1161.

[4] I. Nándori, K. Vad, S. Mészáros, U. D. Jentschura, S. Nagy, K. Sailer, submitted to Phys. Rev. B

[5] I. Nándori, U.D. Jentschura, S. Nagy, K. Sailer, K. Vad, S. Mészáros, submitted to J. Phys. C

4.3 Determination of Al concentration in Al doped ZnO using Auger spectra excited by Mo X-rays

J. Tóth, Á. Németh[a)], L. Kövér, Z. Lábadi[a)], I. Cserny, D. Varga

A good conductor with excellent transparency is of crucial importance for the window layer of CIGS solar cells. Al doped ZnO is a good candidate for this purpose, its conductivity depends on the concentration and chemical state of the Al dopant atoms. It was demonstrated that the non-conventional XPS using Mo X-rays for excitation is a very sensitive tool for the detection of Al, P, Si [1, 2, 3]. The present paper compares the experimental ratios for Zn/Al photoinduced peak intensity ratios obtained using both Al and Mo X-ray excitations. The Mo excited Zn/Al intensity ratios can be determined with higher selectivity and sensitivity than the Zn/Al intensity ratios excited by Al X-rays. The experiments were performed with a hemispherical deflector electron spectrometer [4]. The chemical state of the Al was identified to be close to that in Al_2O_3. The atomic concentrations were determined using a calibration curve based on ZnO/Al samples with known composition of Al. The energy dependent efficiency of the electron spectrometer was determined comparing REELS spectra of Cu specimen to standard spectra measured by K. Goto (Nagoya Institute of Technology, Japan). For evaluation of the Al atomic concentrations from the measured photoelectron intensities the photoionisation cross-sections of Band et al [5] and the IMFP data of S. Tanuma et al [6] and C.J. Powell and A. Jabłoński [7] were used.

a) Research Institute for Technical Physics and Materials Science (MFA) Hungarian Academy of Sciences, H-1525 Budapest, P.O. Box 49., Hungary

[1] L. Kövér, et al. SIA 20 (1993) 659

[2] J. Tóth, et al, Tue-QA-10 Abstract, ECASIA-2005, Vienna

[3] J. Tóth, et al, Abstracts p293. ECASIA-2001, Avignon

[4] L. Kövér, et al. Surface and Interface Analysis, Vol.19 (1992) 9

[5] Band, et al, Atomic and Nuclear Data Tables, Vol. 23 (1979) 443

[6] S. Tanuma, C.J. Powell, D.R. Penn, Surf. Interface Anal, Vol 21 (1994) 165

[7] C.J. Powell and A. Jabłoński, J. Phys. Chem. Ref. Data, Vol 28 (1999) 19

Note: the paper was presented by J.Tóth at JVC-11 Int. Conf, Sep 24-28, 2006, Prague

4.4 Quantification of elastic backscattering of electrons, based on the backscattering yield

G. Gergely[a)], S. Gurban[a)], M. Menyhárd[a)], J. Tóth, D. Varga, K. Tőkési, I. Cserny, L. Zommer[b)], A. Jabłoński[b)], K. Goto[c)]

The determination of electron spectra in absolute units has been developed by K. Goto using his special CMA. Our present paper applied the backscattering yield (BY) (defined by ISO 18115/5.49) and the 50 eV loss range of Ni, Cu and Si for reference samples of the elastic peak. The BY is a physical material parameter, slightly varying with E energy. Experimental BY data of El-Gomati et al and of other authors were compared to our results. Our theoretical BY data were calculated by a new Monte Carlo procedure, proposed by A. Jablonski applying his new stopping power data .Our experimental backscattering spectra were measured by a HSA type electron spectrometer of high energy resolution in the E = 0.6 - 3 keV energy range, normal incidence and 50° angle of detection (ESA-31, Debrecen). Integrating the backscattering spectra results in BY for the solid angle of the spectrometer. The spectra were calibrated by assuming cosine distribution for backscattered electrons and considering the solid angles of detection. Evaluating the spectra the transmission of the CMA was determined and verified (see Goto's recent results). BY is a suitable reference for elastic peak electron spectroscopy. However it is also very promising to use the ratio of loss spectrum integrated for 50 eV and the elastic peak in the process of the determination of IMFP of electrons in REELS. Comparing the experimental elastic peak ratios for sample pairs and calculated data, using the EPESWIN software, the SEP parameters of Chen and Kwei et al were tested as well. All of the mentioned procedures are very important in the quantitative analysis of surface electron spectroscopic methods.

a) Res. Inst. Techn. Phys. H-1525 Budapest, P.O. Box 49

b) Inst. Chem. Phys. PAS Warsaw, Kasprzaka 44/52

c) AESI, Nagoya Japan

Note: the paper was presented by G. Gergely at JVC-11 Int. Conf, Sep 24-28, 2006, Prague

4.5 Morphology, surface roughness, electron inelastic and quasi-elastic scattering in elastic peak electron spectroscopy of polymers

B. Lesiak[a)], *A. Kosinski*[a)], *R. Nowakowski*[a)], *L. Kövér, J. Tóth, D. Varga, I. Cserny, A. Sulyok*[b)], *G. Gergely*[b)]

Elastic peak electron spectroscopy (EPES) deals with the interaction of electrons with atoms of a solid surface, studying the distribution of electrons backscattered elastically. The nearest vicinity of the elastic peak, (low kinetic energy region) reflects both, electron inelastic and quasi-elastic processes. The incident electrons produce surface excitations, inducing surface plasmons with the corresponding loss peaks separated by 1 - 20 eV energy from the elastic peak. Quasi-elastic losses result from the recoil of scattering atoms of different atomic number, Z. The respective energy shift and Doppler broadening of the elastic peak depend on Z, the primary electron energy, E, and the measurement geometry. Quantitative surface analytical application of EPES, such as determination of parameters describing electron transport, requires a comparison of experimental data with corresponding data derived from Monte Carlo (MC) simulation. Several problems occur in EPES studies of polymers. The intensity of elastic peak, considered in quantitative surface analysis, is influenced by both, the inelastic and quasi-elastic scattering processes (especially for hydrogen scattering atoms and primary electron energy above 1000 eV). An additional factor affecting the elastic peak intensity is the surface morphology and roughness. The present work compares the effect of these factors on the elastic peak intensity for selected polymers (polyethylene, polyaniline and polythiophenes). X-ray photoelectron spectroscopy (XPS) and helium pycnometry are applied for deriving the surface atomic composition and the bulk density, while scanning electron microscopy (SEM) and atomic force microscopy (AFM) for determining surface morphology and roughness. According to presented results, the influence of surface morphology and roughness is larger than those of surface excitations or recoil of hydrogen atoms. The component due to recoil of hydrogen atoms can be observed in the elastic peak electron spectra for selected primary electron energies. Experimental and MC simulated ratios of hydrogen contribution to elastic peak are compared.

a) Institute of Physical Chemistry Polish Academy of Sciences, Kasprzaka 44/52, 01-224 Warszawa, Poland

b) Research Institute for Technical Physics and Materials Science Hungarian Academy of Sciences, P. O. Box 49, H-1525 Budapest, Hungary

Note: the paper was presented by B. Lesiak-Orlowska at JVC-11 Int. Conf, Sep 24-28, 2006, Prague

5.1 Fabrication of insulator nanocapillaries from diatoms

R.J. Bereczky, K. Tőkési

Diatoms are unicellular microscopic organisms with silicon-dioxide based skeleton enveloped with an organic material, which composes essentially polysaccharides and proteins (see Fig. 1a.). As it was shown, the valva of the diatoms build up almost from clean silicon-dioxide [1]. Therefore, removing the organic compounds from the diatom, we can have in our hand an ideal, about 100 μ m-sized, and almost cylindrical shaped insulating nanostructure.

There are various techniques available to disembarrass the diatom from its organic compounds. We used the so called hydrogen peroxide method. The advantageous properties of this method are the followings: a) this is one of the fastest procedures among the possible methods, b) do not require special equipment, c) cheap, and last but not least it is less harmful for health compared to other methods. This procedure can be an alternative way of the fabrication of insulator nanocapillaries. In this case the preparation of the nanocapillaries is simple and quick. Moreover, we do not need to invest expensive special techniques, (like micromachining-, electrochemical etching technique, moulding process etc) as it was necessary for the case of previously developed method producing insulator nanocapillaries [2,3]. Fig. 1b and Fig. 1c. show the scanning electron micrograph of the skeleton of the diatoms. The size of the cylindrical holes are roughly 200 *nm* (see Fig. 1c).

Acknowledgements

The work was supported by the grant "Bolyai" from the Hungarian Academy of Sciences, and the National Office for Research and Technology.

[1] R.J. Bereczky, K. Tőkési, J. Tóth, ATOMKI Annual Report (2006)

[2] R.T. Rajendra Kumar, X. Badel, G. Vikor, J. Linnros, R. Schuch, Nanotechnology 16 (2005) 2.

[3] H. Masuda, K. Yasui, T. Yanagishita, M. Nakao, T. Tamamura and K. Nishio, Jpn. J. Appl. Phys 39 (2000) 256.

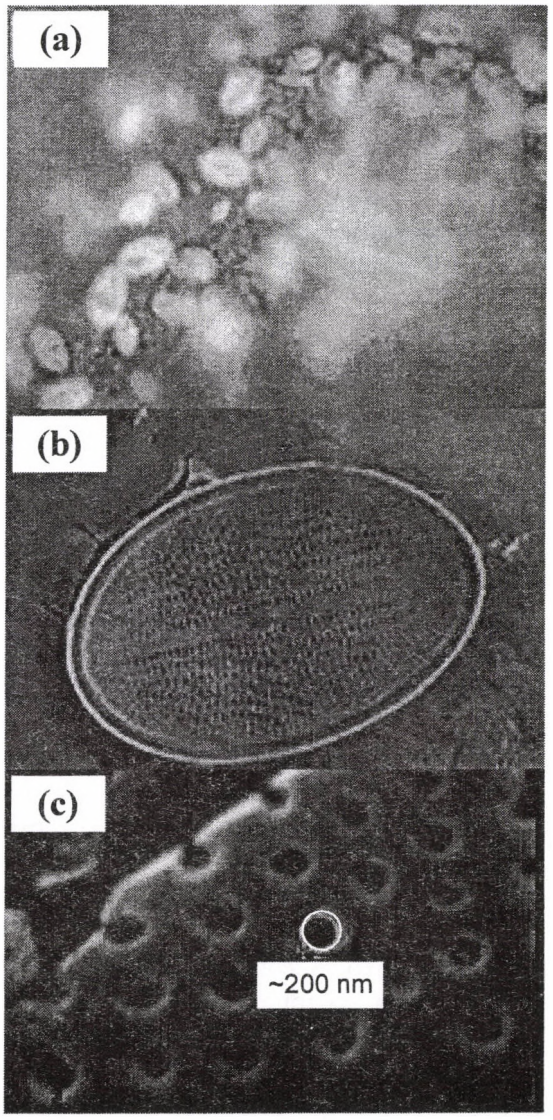

Figure 1. Micrographs of the diatom. (a) optical micrograph of the living microalgae, (b), (c) Scanning electron microscope image of the skeleton of the diatom.

5.2 Study of Pennales diatoms by X-ray Photoelectron Spectroscopy

R.J. Bereczky, K. Tőkési

Algae are unicellular organisms, which can be find in great mass in the nature. In some cases these organisms form cylindrical shape skeleton. In this work the elementary composition of the skeleton of Pennales diatoms is studied by X-ray Photoelectron Spectroscopy (XPS). XPS measurements were preformed with the home built ESA-31 electron spectrometer [1]. The spectrometer consist of a 180° hemispherical electrostatic analyzer with a 250 mm working radius, floatable up to 10 keV and completed with a multi-element zooming electron-optical lens. During the measurements the vacuum in the analysis chamber was better than $5 \times 10^{-}9$ mbar. The samples were cleaned by argon ion sputtering before the measurement with an AGS-2 ion gun using beam energy of 2 keV and a current of 15 μA in time of 3 minutes. The cleanliness of the sample surface was also monitored by XPS analysis.

The photo-electron spectra were excited by the help of a dual-anode (Al, Mg) x-ray source with an Al filter foil. In the present experiment 1486.67 eV excitation energy was used. Fig. 1a. shows the XPS spectrum of the skeleton of Pennales diatoms (curve 1. in Fig. 1). The dominant peaks originated from oxygen and silicon. According to this observation we performed reference measurements using silicagel specimen (see curve 2. in Fig. 1). The silicagel contains 100 % SiO_2. The spectra are normalized to the oxygen peaks. Si peaks are enlarged in Fig. 1b. According to our recent XPS measurements, we found that the shell of the Pennales diatoms contains approximately 80 % SiO_2. Due to this fact the skeleton of Pennales diatoms behaves as an insulator nanocapillary.

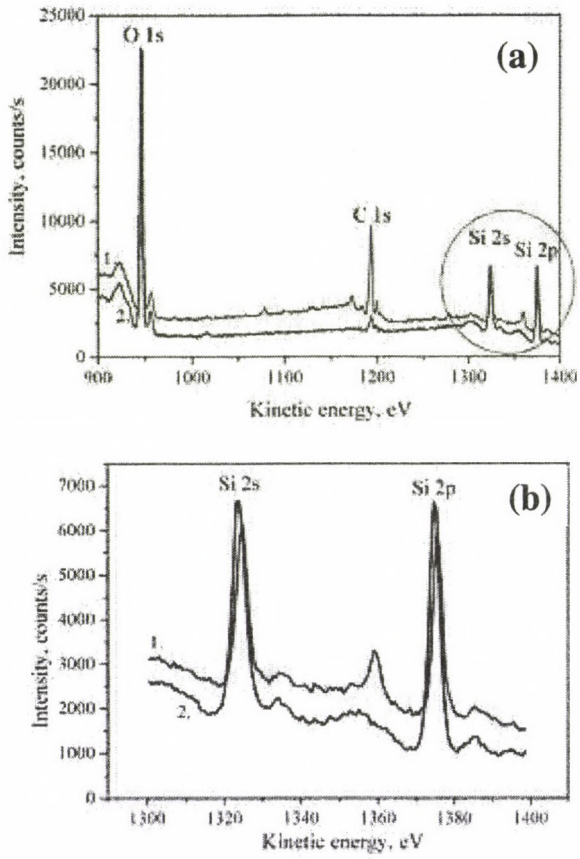

Figure 1. Al K_α excited photo-electron spectra measured by the ESA-31 electron spectrometer. 1) skeleton Pennales diatoms, 2) silicagel.

Acknowledgements

The work was supported by the grant "Bolyai" from the Hungarian Academy of Sciences, and the National Office for Research and Technology.

[1] L. Kövér, D. Varga, I. Cserny, J. Tóth, K. Tőkési, SIA 19 (1992) 9.

5.3 Electron Emission by N^{6+} Ions Scattered at a Magnetized Iron Surface

B. Solleder[a], *C. Lemell*[a], *K. Tőkési* , *J. Burgdörfer*[a]

Magnetized materials are of considerable interest in the electronics industry (hard discs, spintronics, etc.). A detailed understanding of the properties of magnetized surfaces is therefore important to optimize technical applications. In the last decades, different experimental techniques have been developed to probe spin effects in magnetized materials.

In this work the spin polarization of electrons emitted during the impact of N^{6+} ions on a magnetized Fe surface is investigated. We study potential emission (PE) of electrons as well as secondary electron (SE) production and transport in the target with the help of Monte Carlo (MC) simulations. Spin dependence of electron transfer processes and of transport in the solid are included.

Fig. 1 shows the results of our simulation for the energy distribution and spin polarization of emitted electrons in comparison with experimental data of Pfandzelter *et al.* [1] for the interaction of N^{6+} ions with magnetized Fe. Electrons with energies higher than 200 eV are predominantly PE electrons, emitted close to the surface via autoionization (AI), Auger capture (AC) and Auger deexcitation (AD) channels. Low energy electrons are dominated by promoted, autoionized, and secondary electrons. The polarization of above surface electrons is determined by the hight of the potential barrier separating projectile and target. At large distances, the barrier drops only slightly below the Fermi edge and enables transitions of electrons from this part of the band structure which has about 50% polarization. These electrons are transferred to high n states feeding promotion and AI processes between high lying states. Electrons emitted by these processes therefore reflect the polarization near the Fermi edge. Close to the surface, the barrier is low enough to allow for electron capture from the entire conduction band. K-Auger electrons are emitted in immediate vicinity of the surface and therefore mirror the average polarization, which is about 27% for Fe. We find good agreement with experiment for this energy range and partial agreement at low energies, see fig. 1 and [2].

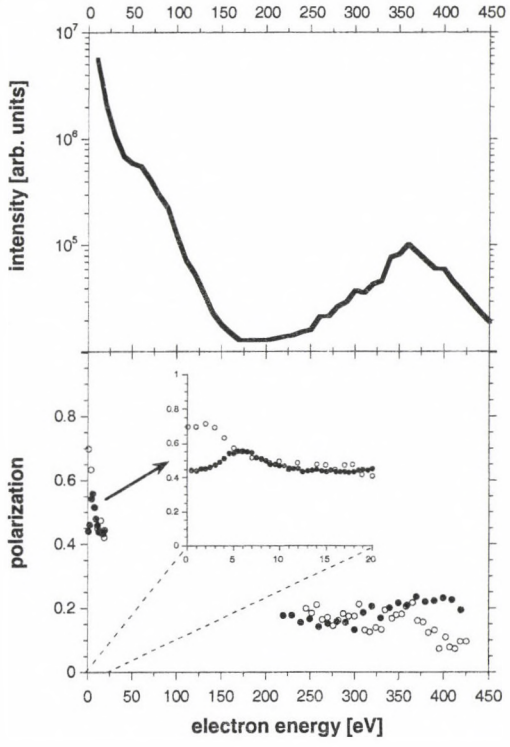

Figure 1. Upper panel: MC result for the energy spectrum. Lower panel: the spin polarization of emitted electrons is shown in two different energy ranges, one for emission energies lower than 20 eV (inset) and the high energy range of K-Auger electrons ($\sim$ 350 eV). Full circles: MC results, open circles: measured data from [1].

Acknowledgements

This work has been supported by Austrian Science Foundation FWF (Project n. P17449-N02), by EU under contract no. HPRI-CT-2005-026015, the Hungarian Scientific Research Found: OTKA nos. T046095, T046454, and the grant "Bolyai" from the Hungarian Academy of Sciences, the TeT Grant no. A-15/04.

a) Institute for Theoretical Physics, Vienna University of Technology, A-1040 Vienna, Austria, EU

[1] R. Pfandzelter, T. Bernhard and H. Winter, Phys. Rev. Lett. 86 (2001) 4152.

[2] B. Solleder, C. Lemell, K. Tőkési, J. Burgdörfer, Nucl. Instrum. Meth. Phys. Res. B, in press.

5.4 Investigation of Sb diffusion in amorphous silicon

A. Csik, G.A. Langer[a)], G. Erdélyi[a)], D.L. Beke[a)], Z. Erdélyi[a)], K. Vad

During the last years amorphous Si and a-Si based alloys have been widely studied and utilized in micro- and optoelectronic devices [1]. The new generation of these devices (thin film transistors, single electron transistor, etc.) require p- or n-type doped active channels with high level of concentration and concentration variation control. Antimony (Sb) is the most frequently used n-type dopant [2]. Thus the knowledge of diffusion mechanisms and data is highly desired for understanding the physical properties of this material. Although the diffusion of Sb in crystalline Si is widely studied, there are only few dates about diffusion in amorphous silicon. Study of diffusion in amorphous materials presents some difficulties. One of the main problems is to keep the thermal stability of the amorphous phase.

In our previous work [3] the diffusion and transformation processes in amorphous $Si_{1-x}Sb_x$ mono-, $Si/Si_{1-x}Sb_x/Si$ tri- and $Si/Si_{1-x}Sb_x$ multilayers systems with different composition (x=13-26 %) were investigated. After annealing the samples the most interesting result was that under hydrostatic pressure (100 bar-4,7 kbar Ar) in the Si/SiSb/Si trilayers (and only in this type of samples and only under hydrostatic pressures) the SiSb layer underwent a spinodal-like decomposition, resulting in three Sb-rich stripes parallel to the interfaces. The transformation at given temperature strongly depended on the initial Sb concentration of the SiSb layers and the applied hydrostatic pressure. No such stripes could be detected when the samples of the same geometry and composition were annealed in vacuum. In this work, we present additional experimental results on the diffusion of Sb in the amorphous $Si/Si_{1-x}Sb_x/Si$ system. In contrast to our former experiments, the concentration of Sb in the samples was reduced to 5 % to avoid the fast crystallization and decomposition in the SiSb layer. Secondary Neutral Mass Spectrometry (SNMS) has been applied to measure the distribution of Sb in as-deposited and heat treated films. In order to detect the possible crystallization and structural transformation processes of the samples Transmission Electron Microscope (TEM) measurements were carried out. The SNMS measurements showed that no concentration changes take place during the annealing of the series of samples in vacuum at temperatures 723 K, 773 K and 823 K for different times. It was showed that sample with 5% Sb concentration annealed lower then 823 K remains in amorphous state. From the time evaluation of SNMS concentration profile $D_{Sb} = 1 \times 10^{-21} m^2/s$ diffusion coefficient was calculated for Sb diffusion in amorphous Si at 823 K. To get information for the temperature dependence of diffusion coefficient we carried out the annealing of the same samples at higher temperatures range (873-1023 K). Unfortunately, as it can be seen from TEM pictures that the samples annealed at 873 K in vacuum and under 100 bar Ar pressure for 5 hours become crystalline. It can be clearly seen that small crystals appears at 873 K and sample annealed 150 K higher can shows fully crystallized sate.

Acknowledgements This work was supported by OTKA Grant No. D-048594, T-043464, F-043372. Z. Erdélyi acknowledges support from Bolyai János Foundation.

a) Department of Solid State Physics, University of Debrecen, P.O. Box 2, H-4010 Debrecen, Hungary

[1] C.N. McKinty, A.K. Kewell, J.S. Sharpe, M.A. Lourenco, T.M. Butler, R. Valizadeh, J.S. Colligon, K.P. Homewood, Nucl. Inst. and Methods B 161-163 (2000) 922.

[2] F. Dimroth, C. Agert, W.A. Bett, Journal of Crystal Growth 248 (2003) 265.

[3] A. Csik, G. Erdelyi, G.A. Langer, L. Daroczi, D.L. Beke, J. Nyeki, Z. Erdelyi, Vacuum 80 (2005) 168.

5.5 Depth profile analysis of electrodeposited nanoscale multilayers by Secondary Neutral Mass Spectrometry (SNMS)

G.L. Katona, Z. Berényi, L. Péter[a)], K. Vad

Nanoscale multilayers have been in the focus of research since the discovery of the giant magnetoresistance (GMR) effect in this family of nanostructures. The first observation of GMR on sputtered magnetic/non-magnetic multilayers was followed by the detection of the same effect in electrodeposited Co-Ni-Cu/Cu multilayers within half a decade. Electrodeposition has long been considered as an inexpensive alternative of the high-vacuum methods to produce multilayers with GMR, although the GMR effect observed for electrodeposited multilayers is usually inferior to multilayers produced by physical methods. Electrochemistry appears to be an exclusive technology to produce multilayered nanowires by using porous templates. In spite of the large number of papers about the multilayers themselves, data on the depth profile of electrodeposited multilayer samples are very scarce. It has long been known that the simultaneous electrodeposition of the iron group metals takes place in the so-called anomalous manner. The diagnostic criterion of the anomalous codeposition is that the metallic component of lower standard potential (the Co in the case of Ni/Co) can be discharged together with the more noble one (Ni) at potentials where the less noble component (Co) alone cannot be deposited onto a substrate composed of the parent metal; moreover, the less noble metal (Co) is deposited preferentially. We have investigated the composition gradient along the growth direction of electrodeposited Co/Cu and CoNiCu/Cu multilayers films using SNMS.

Samples were electrodeposited using the single bath method. Commercial Cu sheets and an Cr/Cu layer evaporated onto Si (111) surface were used as substrates with high and low roughness, respectively. The depth profiles of the samples were recorded using SNMS (INA-X, Specs GmbH, Berlin) in the Direct Bombardment Mode.

Depth profile analysis of electrodeposited magnetic/nonmagnetic layered structures on substrates with different roughness showed that although the depth resolution of samples deposited on commercial Cu sheet was somewhat lower than of the samples deposited on Si(111), the difference is less pronounced than what could be expected. Additionally the SNMS depth profile analysis revealed a significant concentration gradient in the magnetic layers even in the beginning of the layers (see Fig. 1). This concentration gradient within the magnetic layer is usually neglected, although as it can be seen the concentration change along the growth direction is significant even at the beginning of the layer (closer to the substrate). This draws attention on the concentration inhomogeneity in the magnetic layers which could influence GMR properties.

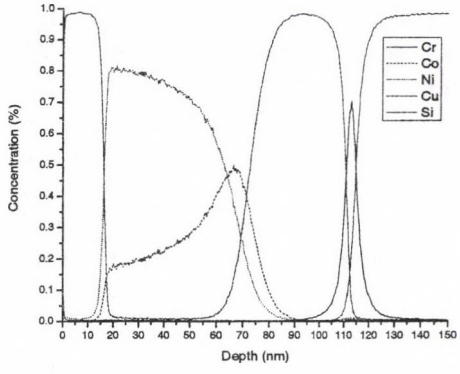

Figure 1. Depth profile of Cu(20nm) / Co-Ni-Cu (50nm) / Cu(20nm / Cu(20nm) / Cr(5nm) / Si(111) sample

Acknowledgements This work was supported by OTKA Grant No. K-60821.

a) Research Institute for Solid State Physics and Optics, Hung. Acad. Sci.

6.1 Fine mapping of tritium emission using absorption vapour samplers

G. Vodila, M. Molnár, M. Veres[a)], É. Svingor, I. Futó, I. Barnabás[b)], S. Kapitány[b)]

Püspökszilágy Radioactive Waste Treatment and Disposal Facility is a near-surface engineered repository designated for disposal of low- and intermediate-level wastes from various institutes, research facilities and hospitals in Hungary. The repository consists of compartments of concrete vaults containing both unconditioned and conditioned wastes packaged in plastic bags or metal drums ("A" type vaults), concrete vaults for storage of organic solvents ("C" type vaults) and steel-lined wells for disposal of spent sources ("B" and "D" type).

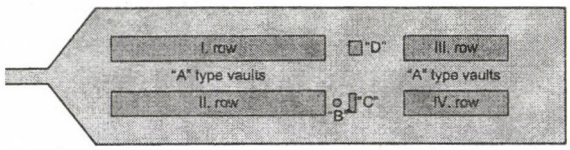

Figure 1. Compartment types and layout at Püspökszilágy RWTDF

In every disposal site gas generation occurs. The gas can get into the environment from the vaults. In order to monitor the continuous emission two special automatic $^{3}H/^{14}C$ sampling units were installed at the site, one near the vaults and the other one near the administrative building, as a reference. The sampling unit near the vaults measured higher ^{3}H (T) and ^{14}C activity concentrations by two orders of magnitude than the reference one. The surplus must have come from the vaults.

To locate the leakages small absorption vapour samplers (AVSs) were developed and placed directly on the ground surface to collect the vapour coming from the vaults. As absorbent silica gel coloured with cobalt was used. After saturation the water was recovered from the silica-gel in the lab. The tritium concentration in the recovered water was measured with a low background Canberra Tri-Carb liquid scintillation counter.

17 AVSs were placed near the vaults and wells, and 2 ones were settled outside the site as reference. From the measured data tritium distribution maps were constructed with SURFER 8.0 (Golden Software). The highest activities were measured under the metal cover of vault "C" (6400 ± 200 and 1990 ± 60 Bq/l), and at the still open vault in the IV. row of "A" type vaults (2940 ± 90 Bq/l). Far lower but considerable activity was detected at the dilatation gap of the III. row of "A" vaults (119 ± 4 Bq/l) while at the dilatation gap of the IV. row of "A" vaults the activity was only 7.1 ± 0.8 Bq/l. Around the rows of "A" type vaults covered by clay and soil layers (rows I. and II.) the tritium activity was rather low (<20Bq/l) but from the tritium distribution map it was possible to locate the leakages of the compartments through the 1m thick clay and soil cover (Figure 2).

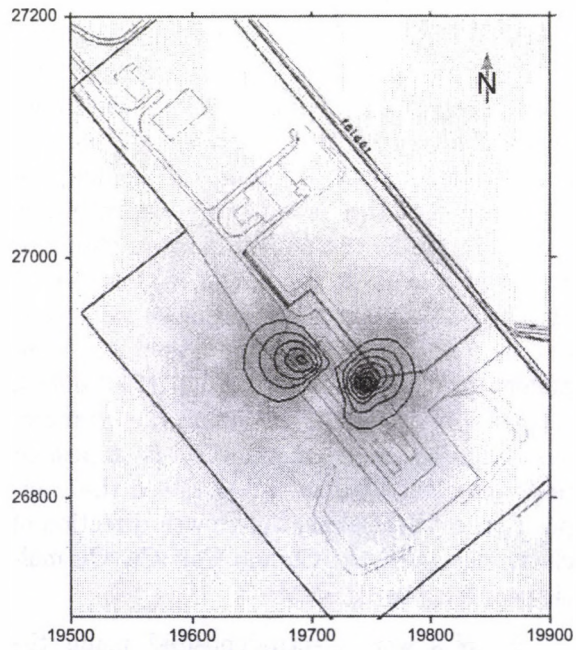

Figure 2. Distribution of tritium released from rows I. and II. of "A" vault

a) Isotoptech Co. Ltd., Debrecen, Hungary

b) Radioactive Waste Treatment and Disposal Facility, Püspökszilágy, Hungary

6.2 Monitoring of the ^{14}C activity in the atmosphere

É. Svingor, M. Molnár, T. Bujtás[a)], *I. Futó, L. Rinyu*

The distribution of atmospheric radiocarbon has been extensively investigated both in the Northern and Southern Hemisphere as well as in the Tropics for a number of decades. Systematic global observations of $^{14}CO_2$ in the troposphere were made during and after atmospheric nuclear weapon tests in the 1950s and 1960s by several laboratories. Nowadays the monitoring of ^{14}C in regions adjacent to nuclear power plants (NPP) or sites of land-filled radioactive wastes has growing importance in determining the frequency and activity of anthropogenic ^{14}C released to the environment. On the other hand, the depletion of ^{14}C in the atmosphere gives information about the regional fossil fuel CO_2 contributions (Figure 1., Prague-Bulovka).

The ^{14}C activity of the atmosphere has been monitored in the vicinity of Paks NPP by sampling environmental air monthly since 1994. Four differential sampling units collect air samples less than 2 km away from the 100-m-high stacks of Paks NPP (A-type stations), and for reference a sampler is operated at a station (B24) ca. 30 km away from Paks NPP.

The highest ^{14}C values were measured at the site located less than 1km away from Paks NPP. The influence of the ^{14}C discharge in the environment decreases rapidly with the distance from the source and under normal operating conditions the effect of Paks NPP is negligible at a distance of 2.5km.

In Figure 1. we have compared our data for Paks NPP measured during the time span of 2000 - 2005 with data from different European monitoring stations. (The ^{14}C activities are given in Δ values: $\Delta^{14}C(‰) = (A_{sample}/A_{standard}\text{-}1) \cdot 1000$.)

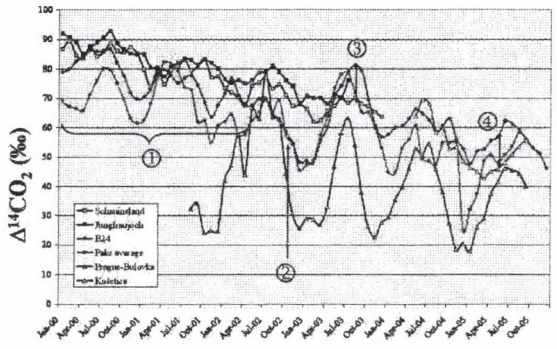

Figure 1. Comparison of the average of $\Delta^{14}CO_2$ data measured in the vicinity of Paks NPP, in station B24, "clean air" data from Jungfraujoch, data set representing the mean continental European troposphere from Schauinsland [1], data from an agricultural/foresty site (Košetice, Czech Republic) and from a strongly polluted area (Bulovka, border part of Prague) [2].

In 2000-2001 the excess ^{14}C at Paks NPP compared to the B24 was 5-10 ‰but its Δ value didn't exceed the tropospheric background (1).

With the growing traffic the inactive CO_2 emission (Suess effect) exceeded the influence of the NPP (2).

After a cleaning tank incident at unit 2 of Paks NPP in April 2003 a 5-10 ‰rise of $\Delta^{14}CO_2$ was observed at all stations (3). During the remediation activities this decreased slowly in 2004 and ceased by the second half of 2005 (4).

a) Paks Nuclear Power Plant, Paks, Hungary

[1] I. Levin and B. Kromer, Radiocarbon 46(3), 1261 (2004)

[2] I. Světlík et al., Czechoslovak Journal of Physics 56 (1) 291 (2006).

6.3 Review of Holocene lacustrine carbonate formation in the light of new radiocarbon data from a site of Csólyospálos, Central Hungary

M. Molnár, I. Futó, É. Svingor, P. Sümegi[a)]

The deposition of lacustrine marls and the formation of freshwater carbonates have been traditionally linked to the Boreal Phase of the Early Holocene in Hungary. These were all based on the assumptions that the dry and hot climate of the Hazelnut Stage (between the 7500 and 5000 yr BP ^{14}C dates) favored a partial desiccation of minor ponds, leading to the precipitation of carbonates, and the formation of extensive lacustrine carbonate beds.

In order to corroborate these initial assumptions new sample sites were drawn under investigation from the central and western parts of the Carpathian Basin as well. The present study details the findings of such a single site from the central parts of Hungary and tries to put the newly gained information into a wider context to corroborate or refute these initial presumptions mentioned earlier.

Radiocarbon measurements were implemented in the Laboratory of Environmental Studies of the ATOMKI in Debrecen, Hungary (^{14}C Lab Code: Deb-). For the above mentioned purpose, 20 g of cleaned mollusk shells have been utilized taken from the samples. Shell fragments were boiled in distilled water and cleaned with diluted H_2O_2 before the further pre-treatment.

The comparative analysis of newly gained radiocarbon results (Table 1.) from a site of Csólyospálos, Central Hungary with those of other Hungarian lacustrine carbonates yielded stunning new results. According to these, carbonate deposition must have initiated much earlier, possibly around the 10,000 - 11,000 yr BP ^{14}C age (9500 BC - 11000 BC) in the Carpathian Basin. Furthermore, the formation of lacustrine carbonates must have come to an end at very different times in different parts of the basin contrasting previous views on the uniform and synchronous cessation of lacustrine carbonate formation in Hungary. According to the newest results presented here, carbonate deposition in the southern and southeastern parts of the basin ceased around the 6000 yr BP ^{14}C date ($\sim$ 4900 BC). Meanwhile, in the central parts it continued as long as the terminal Bronze Age; i.e. till around 1300 BC.

a) Department of Geology and Palaeontology, University of Szeged, Hungary

[1] Gy. Szöőr et al. Quarter és neogén Molluscahéjak kemotaxonómiai és paleoökológiai elemzése (Chemical taxonomy and paleoecology of modern and older Quaternary mollusk shells) In: SZÖŐR GY. ed. Fáciesanalitikai, paleobiogeokémiai és paleoökológiai kutatások. MTA Debreceni Bizottsága, Debrecen. pp. 111-181. (1992) (in Hungarian with English abstract)

Table 1. Radiocarbon dates from the outcrop of Csólyospálos (* from Szöőr et al. 1992 [1])

Lab Code	Depth [cm]	^{14}C age [yr BP] (1 σ)	cal BC
Deb-2635	30 - 40	3391 $\pm$ 80	1890 - 1490
Deb-1067*	60 - 65	8040 $\pm$ 200	7600 - 6500
Deb-3303	70 - 75	8603 $\pm$ 90	7950 - 7480
Deb-3282	80 - 85	8747 $\pm$ 70	8200 - 7550
Deb-3290	90 - 85	9237 $\pm$ 80	8640 - 8270
Deb-3286	105 - 115	10119 $\pm$ 81	10400 - 9350

6.4 Determination of radiocarbon content in young stalagmites of Baradla cave and its interpretation

M. Molnár, I. Futó, L. Rinyu, É. Svingor, Z. Dezső[a)]

It was demonstrated by international references that ^{14}C dating with dead carbon corrections (*dcp*) of stalagmites could be used as a substantive, inexpensive and efficient absolute dating method [1]. Detecting of varying of specific *dcp* for different regions or different time periods could provide substantial information about the regional climatic changes or about the variations of carbon-dynamic conditions in the karstic systems. Up to the present ^{14}C dating was not applied sufficiently in the study of stalagmites in Hungary.

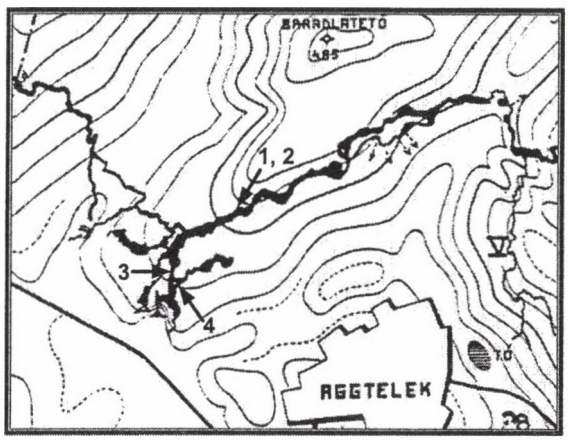

Figure 1. Location of sampling points in the Baradla cave.

Radiocarbon content of four different young stalagmites (S-1 to S-4, see numbers in Figure 1.) from Baradla cave, Aggtelek (Hungary) was measured in the Laboratory of Environmental Studies at the ATOMKI.

Samples were formed on artificial surfaces between 1991 and 2004. Using ^{14}C data of the young stalagmites and that of the atmospheric CO_2 in this period, dead carbon portion (*dcp*) has been calculated for each sample. Typical *dcp* values were between 5 and 7 % for three samples (S1, S2 and S4). The outlier fourth result (S3) showed that if the dissolved carbonate had to seep through a long way in a karstic system before reaching the cave and in this period the radiocarbon concentration of the atmosphere is significantly changing, then comparison of the ^{14}C content of a stalagmite and the atmosphere at the time of its formation is not realistic.

a) Department of Environmental Physics, University of Debrecen, Hungary

[1] M. Molnár et al. ^{14}C mérés alkalmazása a karsztkutatásban (Application of ^{14}C dating in study of karst). Karsztfejlődés IX. Eds.: Veress M. Szombathely, Hungary, BDF 9-, 2004 (in Hungarian with English abstract)

Table 1. The *dcp* results calculated for the individual stalagmite samples.

Stalagmite sample	$\delta^{13}C$ (‰) (PDB)	^{14}C activity (pMC) (NBS)	*dcp* (%)
S-1	-9.5 ± 0.2	104.2 ± 1.0	5.3 ± 1.3
S-2	-9.9 ± 0.2	103.6 ± 1.0	5.8 ± 1.3
S-3	-6.2 ± 0.2	106.9 ± 1.0	2.8 ± 1.3
S-4	-8.5 ± 0.2	102.6 ± 1.0	6.7 ± 1.3
CO_2 air (1991 - 2004)	-9 ± 2	110.0 ± 1.0	

6.5 Radiochemical analysis of ice cores from Borţig Ice Cave, Apuseni Mts, Romania

M. Molnár, Z. Kern[a)], *B. Nagy*[a)], *A. Perşiou*[b)]

Validation of cave ice in paleoclimatology is mainly criticised due to the episodically appearing multiannual negative mass balance periods. Not only the total amount of increment is destructed during these periods but previously deposited ice could also be destroyed creating longer hiatus in the startigraphy than the melting period.

Borţig Ice Cave is the third largest ice cave of the Apuseni Mountains, Romania. The main shaft has approximately 45 m depth to the ice surface; the ice thickness is estimated for 20 m (Figure 1.). The cave contains about 25000 m^3 of ice. We decided surveying and estimating the age and ascertain the potential gaps of the upper ice layers in Borţig Ice Cave.

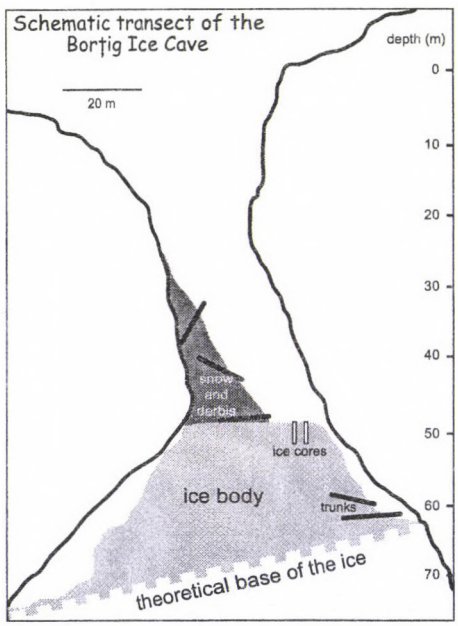

Figure 1. Schematic transect of the Borţig Ice Cave. Approximate place of extracted cores are indicated.

We have chosen the anthropogenic bomb-peak of tritium (^3H) concentration as reference horizon, because it has a well-known and distinct maximum in the atmospheric precipitation at June of 1963 according the "nuclear silence" on the Northern Hemisphere.

We extracted ice cores with approx. length of 2 metres from Borţig Ice Cave on 11^{th} and 12^{th} of December 2005. Sequence of ice layers with different physical properties within the cores was recorded. The core profile suggested that a less dense, grainy ice and a denser, transparent ice layer coupling together and form one higher order stratigraphic unit.

The tritium activity was measured on water melted from the twenty samples of BA core (from BA-1 to BA-20) using liquid scintillation technique in the ATOMKI. The resulted activities suggest the position of the raised tritium concentration from the year of 1963 is between 81 and 102 cm below the ice surface at the drilling date (Figure 2.).

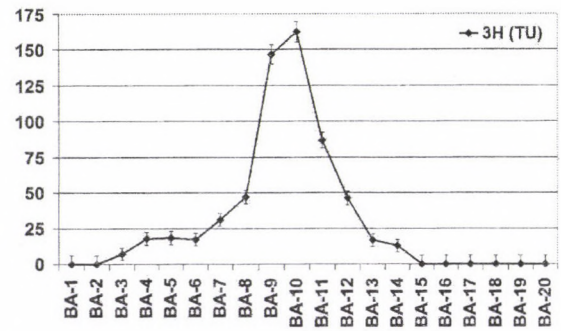

Figure 2. Tritium "bomb-peak" in the BA core.

Following some calculation we predict that the position of the tritium peak is probably at 95 cm below the ice surface. In addition, we argue that the higher order startigraphic units represents the annual increment at the Borţig Ice Cave. Finally, we have ascertained three periods since 1950 with different ice accumulation rates: 1 cm/a for 1992-2005; 2.8 cm/a for 1963-1992; even higher for 1953-1963 period.

a) Department of Physical Geography, Eötvös Loránd University, Budapest, Hungary

b) "Emil Racoviţă" Institute of Speleology, Cluj Napoca, Romania

6.6 Vörs-Máriaasszonysziget - an interdisciplinary study of the prehistoric site

Zs. Medzihradszky[a)], K. T. Bíró[b)], M. Molnár, É. Svingor, L. Rinyu, I. Futó

Vörs-Máriaasszonysziget is located close to the south-western corner of Lake Balaton in the marshes called Kis-Balaton. It represents a very special environment. Its primary importance is in supplying new data on the beginning of agriculture in the Carpathian Basin. It is also important as a possibility for diachronic investigation of a characteristic ecological niche, offering a unique possibility to study the gradual appearance of human impact in various aspects of the landscape and the environment.

Several campaigns of rescue excavations took place on the site in the early 1990-ies [1]. These works resulted in the discovery of Early Neolithic material belonging to the Starčevo culture, one of the most important proofs of the Northern expansion of the culture. The site is located at the northernmost known boundary of the culture, its significance is therefore essential for the neolithisation of the Carpathian Basin. Apart from the Early Neolithic material, features and finds of 7 more archaeological cultures were found: the archaeological evidence ranges from Early Neolithic till Middle Ages.

During the early Neolithic period of the settlement, dated by radiocarbon method to the middle of the 6th millennium BC (Figure 1) the shore of the lake and the small islands were covered with closed mixed forests. Very small changes in the precipitation and temperature effected patches of beech forest in the mainly dominant mixed oak forests. Along the shore lines narrow alder forests appeared. In the shore area the dominance of the bulrush vegetation is evident. The water depth of the bay was about 2 m. According to the archaeobotanical investigation of the locality the crop cultivation and animal husbandry were clearly observable though not on a large scale. The surrounding waters supplied essential portion of the nutrients [2].

Sporadic settlement traces in various periods of the Copper Age (4^{th} millennium BC) give evidence of the human presence between 4500 and 2800 BC (Figure 1).

The second most significant period of habitation is represented by the Early Bronze Age (around 2000 BC, Figure 1), when the settlement area was surrounded with a circular ditch. This time the forests opened because of the human activity.

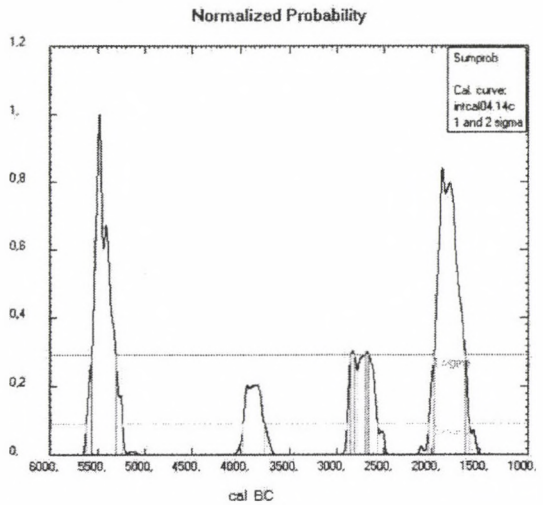

Figure 1. Cumulative probability density functions of cultures from Early Neolithic to Early Bronze Age in Vörs-Máriaasszonysziget [3]

a) Hungarian Natural History Museum, Dept. of Botany, Budapest, Hungary

b)Hungarian National Museum, Budapest, Hungary

[1] N. Kalicz et al., Vörs, Máriaasszony-sziget. Archaeological investigations in Hungary Budapest, Kulturális Örökségvédelmi Hivatal és a Magyar Nemzeti Múzeum, 2002. pp 15-26.

[2] Zs. Medzihradszky, Holocene vegetation history and human activity in the Kis-Balaton area, W. Hungary. Studia Botanica Hungarica 36, 77 (2005)

[3] M. Stuiver and PJ. Reimer, Radiocarbon 35, 215 (1993)

6.7 Spatial variation of ^{222}Rn activity concentration in dry carbon dioxide spas

I. Csige and S. Gyila[a)]

Introduction

The relatively high flux of seepage of deep origin geogas, containing mostly carbon dioxide, is used in many places in the form of dry carbon dioxide spas (mofettes) to treat patients suffering mostly from vaso-constriction diseases. In these spas the geogas fills up ordinary pools and patients submerge into the gas up to their chest level.

Naturally occurring radon gas is also present in the geogas. In this work we have used the Radamon type [1] etched track radon detectors to measure the spatial distribution of ^{222}Rn activity concentration in such a pools.

Results

We have found that despite the similar construction of different pools the vertical profile of ^{222}Rn activity concentration exhibits different behaviours in them.

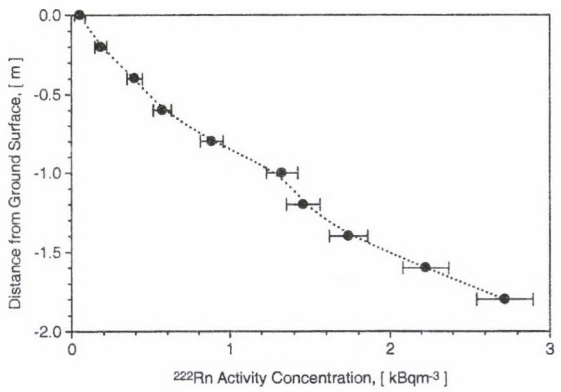

Figure 1. Variation of ^{222}Rn activity concentration in the pool of the Great-mofette of the Cardiovasculare Hospital (Covasna, Romania).

In some cases, like in the case of the Great mofette of Covasna (Fig. 1.), the ^{222}Rn activity concentration decreases approximately exponentially from the bottom of the pool upwards to the ground level, where carbon dioxide is levelled by overflow facilities. This suggests that the source of ^{222}Rn should be found on the bottom of the pool.

In other cases, like in the case of the Bardócz-mofette, found also in Covasna (Fig. 2), however, we have found that ^{222}Rn activity concentration increases from the bottom of the pool and has a maximum near the ground level.

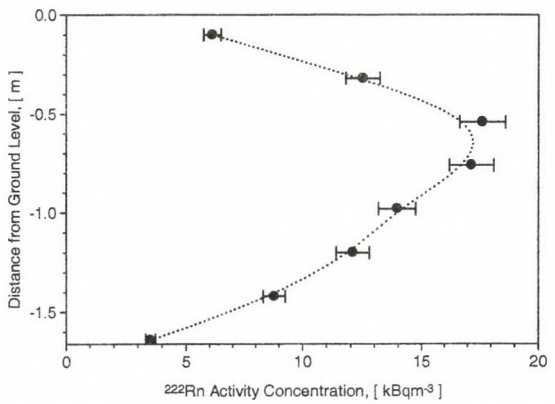

Figure 2. Variation of ^{222}Rn activity concentration in the pool of the Bardócz-mofette (Covasna, Romania).

This suggests that the source of ^{222}Rn gas in this case is not on the bottom of the pool but somewhere on the sidewalls of the pool near the surface. This, however, also suggests, that the source of carbon dioxide may also be found on the sidewalls of the pool.

a) Spital de Recuperare Bali Cardiovasculare, lab. Fisica. str. Eminescu, No. 160. 4055 Covasna, Romania.

[1] Csige I. and Csegzi S. (2001) The Radamon radon detector and an example of application. Radiation Measurements, 34(1-6), pp. 437-440.

6.8 Variation of the PM10, PM2.5 and BC particulate masses of urban aerosol in Debrecen

I. Borbély-Kiss, E. Dobos, Zs. Kertész, E. Koltay, Gy. Szabó

Airborne particulate mass and its elemental composition are usually used for the qualification of local air at a given region.

PM10 particulate mass includes both fine and coarse dust particles less than 10 micrometers in diameter. PM2.5 mass includes fine particles less than 2.5 micrometers in diameter. Coarse dust particles are between 2.5 and 10 micrometers in diameter. Black carbon (BC) is a particulate pollutant of aerosol emitted from the combustion of carbonaceous material.

Mass concentrations of coarse and fine aerosol fractions, and the BC content of fine aerosol were studied from Nov. 1996 to Nov. 2006 in the Institute of Nuclear Research of the Hungarian Academy of Sciences (ATOMKI). Elemental concentrations of both aerosol fractions were also determined (see next abstract).

Aerosol samples were collected in the yard of ATOMKI twice a week with a two-stage "GENT" SFU (stacked filter unit) sampler. Airborne particulate masses (coarse and fine) were measured using a Sartorius microbalance. The black carbon content of fine aerosol was determined by a Smokestain reflectometer.

Monthly average concentrations of the particulate mass were calculated from the database. From the variation of the monthly average concentrations conclusions were drawn on the seasonal behaviour of the PM10, PM2.5 and BC concentrations. Smoothed curves on Fig.1. show winter maxima of concentration in PM2.5, BC and PM10. The concentration of fine mode aerosol exceeds the concentration of coarse one in this site. Comparing our data to the annual standard value set by the European Commission (40 $\mu g/m^3$) we can conclude that PM10 concentrations are under this limit. EU legislation has no standard yet for PM2.5. We compared our fine mode data to the US-EPA annual standard (15 $\mu g/m^3$) and can remark that the PM2.5 concentrations here exceeded this limit almost always in the last decade.

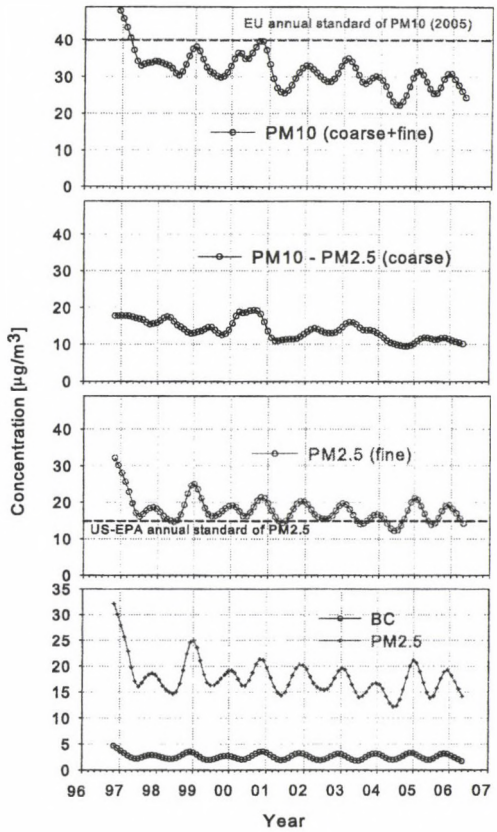

Figure 1. Smoothed curves of the monthly average concentrations of PM10, PM2.5, BC and the existing annual standard values.

Acknowledgements

This work was supported by the National Research and Development Program (NRDP 3A/089/2004) and the Hungarian Research Foundation (OTKA F603777).

6.9 Variation of the elemental concentrations of urban aerosol in Debrecen

I. Borbély-Kiss, E. Dobos, Zs. Kertész, E. Koltay, Gy. Szabó

Coarse and fine aerosol samples described in the previous abstract were analyzed by PIXE (Particle Induced X-ray Emission) method.

Elemental concentrations of Al, Si, P, S, Cl, K, Ca, Ti, V, Cr, Mn, Fe, Ni, Cu, Zn, As, Br, Pb elements were determined.

Monthly and yearly average concentrations and enrichment factors of the above elements were calculated from the database obtained by the analyses.

As a first step the possible source of an element can be determined by the E_f enrichment factors:

$$E_f = (C_x/C_{Ti})_{aerosol}/(C_x/C_{Ti})_{Earthcrust}$$

where C_x is the concentration of the element in question, C_{Ti} is the concentration of Ti. Ti was used as reference element, as it has no other considerable source besides Earth crust. $E_f \approx 1$ values mean natural (crustal) source, and $E_f \geq 10$ values imply anthropogenic origin. Elements above have been sorted into two groups - natural (crustal) and anthropogenic - according to their possible sources. Fig.1. for instance shows smoothed curves of the monthly average concentrations of Si, S, Ca, Ti, and Pb elements measured in fine and coarse mode aerosol. S and Pb belong to the anthropogenic group, Si, Ca, Ti belong to the natural one.

From the variation of the monthly average concentrations conclusions were drawn on the seasonal behaviour of these elements. Concentrations of S, Pb, derived mainly from anthropogenic sources, both in fine and coarse mode (except fine S) have their maxima in winter. Concentrations of Si, Ca, Ti, derived mainly from natural sources have their maxima in summer during the investigated time interval.

Further statistical analyses show us the tendencies of concentration for each element.

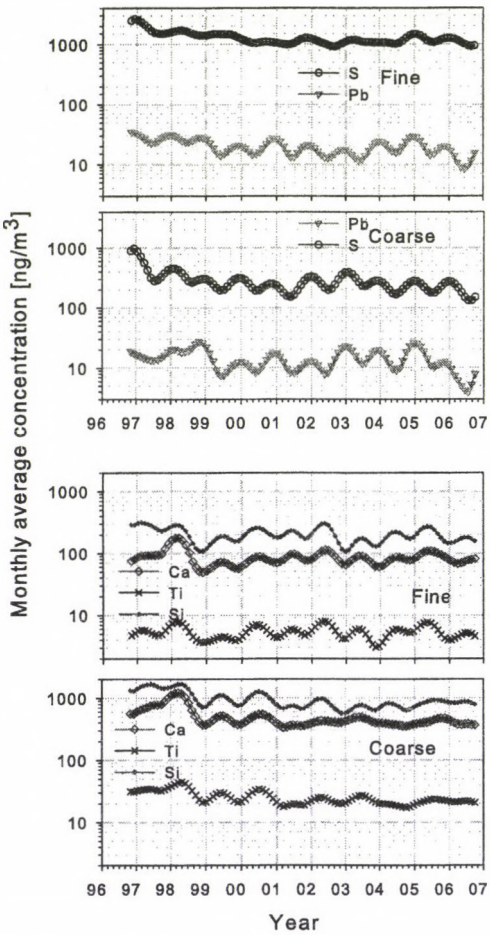

Figure 1. Smoothed curves of the monthly average concentrations of Si, S, Ca, Ti, and Pb elements measured in fine and coarse mode aerosol.

Acknowledgements

This work was supported by the National Research and Development Program (NRDP 3A/089/2004) and the Hungarian Research Foundation (OTKA F603777).

6.10 Comparison of Debrecen fine fraction aerosol data with others collected in some European collaboration

E. Koltay, I. Borbély-Kiss, E. Dobos, Zs. Kertész, Gy. Szabó

Recently a number of papers have been published by European groups [1], [2], [3], [4] organized mainly by western- and middle European laboratories, in which comparative data have been presented from co-ordinated research programs for air qualification in a number of urban sites based on joint evaluation of elemental composition and reflectance of ambient fine aerosol particles.

The time interval June 2000 to December 2001 scanned in the co-ordinated program of *Götchi et al* [1] is mainly covered by a part of our long term data set. All together 107 sampling days have been used here work over the above time interval.

Due to the gross parallelism of the total observation periods and the principal similarity of the used analytical methods in their and our works, we found it plausible to find out how much the air quality characteristics observed at our location fit in the general European trends.

Sampling sites arranged in selected European regions are numbered as follows: **West and Central Europe:** Antwerp South (1), Antwerp City (2), Paris (3), Erfurt (4), Basel (5); **Spain:** Barcelona (6), Galdakao (7), Albacete (8), Oviedo (9), Huelva (10); **Alpine France:** Grenoble (11); **Northern Italy:** Pavia (12), Turin (13), Verona (14); **England:** Ipswitch (15), Norwich (16); **Scandinavia:** Reykjavik (17), Gothenburg (18), Umea (19), Uppsala (20); **Estonia:** Tartu (21); **Hungary:** Debrecen (22).

For a first orientation about the existence of similarities and differences within and among the regional features, respectively, yearly average concentrations are presented in Figure 1 for silicon, and sulphur elemental constituents and PM2,5 integral concentrations for sites 1 22. Silicon, sulphur, and black carbon are considered as main representatives of the crustal material, traffic and long-range background pollution components, respectively, while PM2.5 is a parameter accepted for measuring overall air quality from the point of view of human health conditions in a site. For a qualitative evaluation of air conditions in Debrecen site, yearly values for sites 1-21 are shown with long dashed lines.

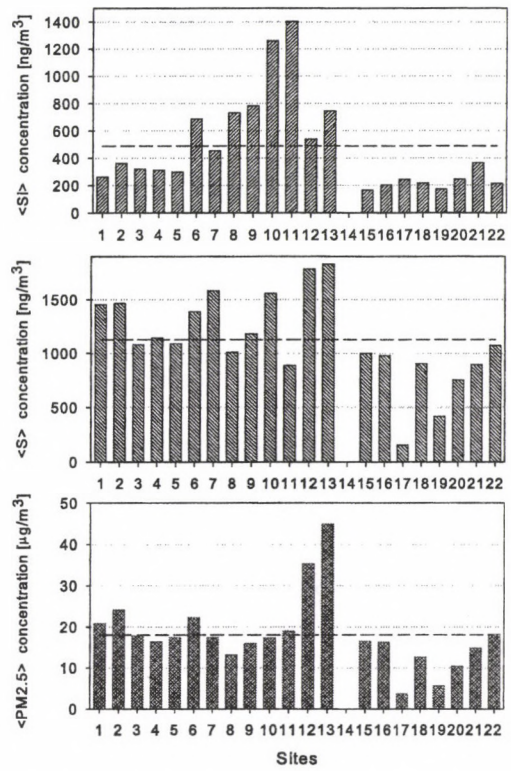

Figure 1. Yearly average elemental concentrations of Si and S as well yearly averages of PM2,5 mass in sampling sites defined in text, for the period June 2000-May 2001. They are considered as main representatives of traffic, crustal material and long-range background sources, respectively.

[1] T. Götchi et al., Atmospheric Environment 30, 369 (2005).

[2] R. Hitzenberger, et al., Atmospheric Environment 38, 6467 (2004).

[3] J.P. Putaud et al., Atmospheric Environment 38, 2579 (2004).

[4] R. Van Dingenen et al., Atmospheric Environment 38, 2561 (2004).

6.11 Examination of the soil redistribution through the vertical distribution of the radionuclide-content of undisturbed soils

Á. Bihari, Z. Dezső[a] and Sz. Szabó[b]

Recent concern for the problems of natural and anthropogenic landscape- and slope-transformation has highlighted the need for quantitative data on longer term soil redistribution rates. The analysis of the vertical distribution of fallout ^{137}Cs in soils can be used to deduce information on the magnitude and temporal pattern of soil erosion. This paper summarizes the intermediate results of a pilot study testing the capabilities of this kind of analysis in Hungary.

The basics of the fallout ^{137}Cs method, the characteristics of the studied area and the determination of the reference inventory and depth distribution have been introduced in our previous report [1]. Continuing, we have started to examine a rapidly evolving dell downslope to the ref. point. It is an uncultivated piece of land with an altitude between approx. 230 and 260 m a.s.l. This area is of particular interest because its deepening and opening in the backward direction threatens the sustainability of the agricultural work around the valley head (near the ref. point).

The basic assumption of the fallout ^{137}Cs method is that landscape points with higher/lower radiocaesium inventory compared to the local ref. inventory are subjected to net accumulation/erosion, respectively. This assumption is valid mostly for cultivated areas where radiocaesium is thoroughly homogenized in the plough layer so the ^{137}Cs content of the eroded/accumulated material is more-or-less constant. In case of uncultivated soils, however, usually there is a decrease in ^{137}Cs activity concentration (AC_{Cs}) with increasing depth. This means that the radiocaesium content of the eroded and the accumulated sediment can be rather different for the same landscape point as these possess a much larger temporal variation, compared to a cultivated area receiving the same fallout input. This kind of depth dependent radionuclide analysis is very rarely applied in practice (e.g. [2]) because commonly used models require the knowledge of total inventories only.

Major experimental work has been carried out for the examination of the vertical and horizontal distribution of ^{137}Cs. From 31 locations of the studied area, covering approximately 2 ha, soil samples have been collected. The total sampling depth has been 40 cm; in 26 cases these have been taken in three sections (0–20 cm, 20–30 cm, 30–40 cm), while in the remaining 5 cases the upper 30 cm has been sectioned with a 5 cm increment. The majority of the sampling have been performed along the thalweg of the dell, while the remaining sampling points can be found on the two valley-sides. Standard preparation procedures have been applied to the collected samples and the activity concentration and inventory of ^{137}Cs, as well as the mass density of every layer have been determined.

The results show a great variety throughout the studied area. In the upper 20 cm the average AC_{Cs} is 11.3±3.1 Bq/kg, with a minimum of 6.2 Bq/kg and a maximum of 19.2 Bq/kg. Within the next layer (20–30 cm) the average AC_{Cs} is 4.4±3.4 Bq/kg, with a minimum of 0.2 Bq/kg and a maximum of 11.1 Bq/kg. In the last sampled layer (30–40 cm), we have found an average AC_{Cs} of 1.1±1.6 Bq/kg, with a minimum of 0.0 Bq/kg and a maximum of 5.5 Bq/kg. The decrease of AC_{Cs} with depth is valid for most samples but there are exceptions, especially when it is examined with higher resolution (see later).

As a more detailed example, the depth distribution of AC_{Cs} of a landscape point with equilibrium-state (Fig1. a), with net erosion (Fig1. b) and with net accumulation (Fig1. c) are presented here. There is a common feature in the deeper region of each depth distribution: a large difference between the AC_{Cs} of two neighboring layers can be seen, but the position of this breakpoint and the magnitude of the breakdown is different in each case. The

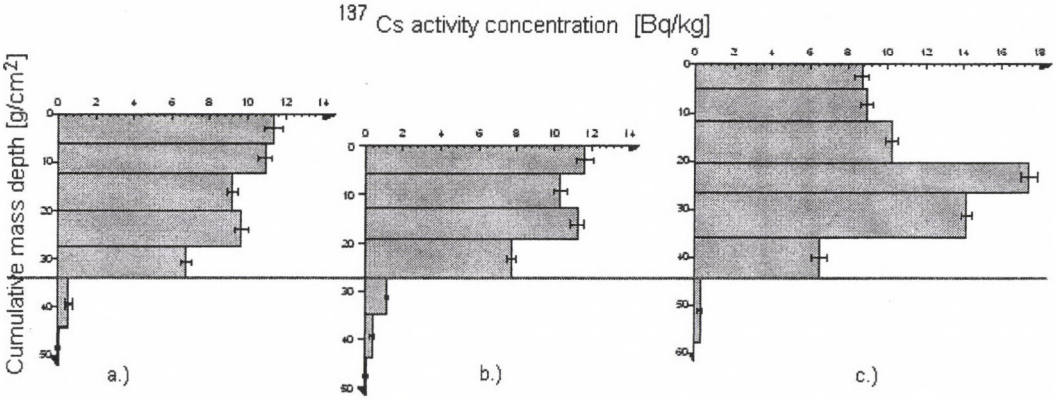

Figure 1. The depth distribution of ^{137}Cs at three sampling points

ratios of AC_{Cs}s are 11 to 1, 7 to 1 and 22 to 1, respectively. The presence of the breakpoint is caused by the phenomena that under present precipitation conditions the moisture content below about 25 cm is usually not high enough for the effective downward migration of radiocaesium. The different magnitude of the breakdown can be explained by the fact that the lower limit of the soil's wetting follows the current soil surface. Thus at an eroding site the limit moves downward allowing further migration, while at an accumulating site it is in the opposite way.

If the depth of the breakpoint is used to level the three depth distributions (see gray line on Fig1.), one can obtain the total net soil loss or gain (in kg/m^2 or in mm) of the second and third distribution compared to the first (in which the total ^{137}Cs inventory is 3296±58 Bq/m^2 which equals with the experimental value of the local ref. inventory (3229±313 Bq/m^2) within errors). These are the cumulative effect of about 50 years of soil redistribution. The eroding site has a net erosion rate of –1.3 kg/m^2/year or –1 mm/year, while the accumulating one has a net accumulation rate of 2.2 kg/m^2/year or 1.8 mm/year.

In the middle region of the distributions there is also a common feature: a local maximum which is the time-stamp of the most intensive bomb-derived fallout. While below this depth the radiocaesium content is entirely bomb-derived, the upper layers can contain a mix of bomb-derived and Chernobyl-derived ^{137}Cs with both direct and sediment origin. The peak of the bomb-derived fallout is best preserved in the third distribution because it is covered with a thick layer of sediment with an average AC_{Cs} of about 9 Bq/kg. There is no sign for the Chernobyl-derived ^{137}Cs in the near-surface layer(s) of this distribution - it seems to be removed completely. In the other two distributions also only a fragment of the theoretical value can be found.

Out of all points sampled, the highest net erosion and accumulation rate is found to be about –2.3 kg/m^2/year and 4.8 kg/m^2/year, or –1.8 mm/year and 4.0 mm/year, respectively. It must be noted that the highest net accumulation rate does not belong to the point with the highest total ^{137}Cs inventory.

a) Univ. of Debrecen, Dept. of Environ. Physics

b) Univ. of Debrecen, Dept. of Landscape Protection and Environmental Geography

[1] Z. Dezső *et al.*, ATOMKI Ann. Rep. 2003 (2004) 57–58.

[2] R. A. Sutherland, Hydrological Processes 21 (1998) 995–1007.

7.1 Radioisotopic Study of Methanol Transformation over H- and Fe-Beta Zeolites; Influence of Si/Al Ratio on Distribution of Products

É. Sarkadi-Pribóczki, N. Kumar[a)], D.Yu. Murzin[a)] and Z. Kovács

The acid-basic properties of Beta zeolite can be modified by dealumination and/or ion-exchange. The wide-pore H-Beta zeolite has strong Brønsted acid sites and other chemical environment which govern adsorption and conversion of methanol to dimethyl ether and hydrocarbons during catalysis [1-2]. Partly Fe-ion-exchanged Beta i.e. Fe-H-Beta zeolite keeps this behavior to a certain extent; however, the presence of Fe ions can modify the reaction pathway. In the present work, the methanol conversion was studied over H- and Fe-Beta zeolites at two different Si/Al ratios. ^{11}C-methanol was used to follow-up adsorption as well as desorption of methanol and its derivates. Therefore, a radioactivity detector was integrated to the gas chromatograph for exact identification of the labelled methanol and its derivates.

H-Beta and Fe-Beta zeolites were applied at two different Si/Al ratios i.e. H-Beta(25) and H-Beta(300) and Fe-H-Beta(25) and Fe-H-Beta (300), respectively. A glass tube fixed-bed reactor was used as a closed static reactor. The ^{11}C-radioisotope ($T_{1/2}$=20.4 min) was produced in ^{11}C-labelled carbon dioxide form by cyclotron. The ^{11}C-methanol tracer was produced by radiochemical process [3]. The mixture of ^{11}C-methanol and non-radioactive methanol was then introduced into zeolite by He gas flow. The volatile products of catalytic conversion of ^{11}C-methanol were analyzed by radio-gas chromatography (gas chromatograph with flame ionization detector (FID) coupled on-line with a radioactivity detector).

The methanol conversion rate and product selectivities to dimethyl ether, hydrocarbons (methane, C_2-C_6 olefins and paraffins), formaldehyde and carbon-oxides were measured and calculated over H- and Fe-Beta zeolites at two different Si/Al ratios at 250 and 350 °C.

Over H-Beta(25) C_2-C_6 hydrocarbons (mostly as alkanes) with high conversion rate and some dimethyl ether were detected due to presence of strong Brønsted acid sites (~270 μmol/g). Contrary, over H-Beta(300) a negligible amount of above gas products was detected at 250 °C due to less Brønsted acid sites (~82 μmol/g). At higher temperature (350 °C) the methanol conversion rate increased resulting in higher selectivity to C_1-C_2 and higher olefin/paraffin product ratio over H-Beta(300) compared to H-Beta(25).

Over Fe-modified Beta zeolite as a bifunctional beta zeolite the methanol conversion rate was high with high selectivity to dimethyl ether and only small amount of hydrocarbons (irrespectively of Si/Al ratios) was formed at 250 °C. Nevertheless, formaldehyde as an additional product was detected at 350 °C besides lower amounts of ether and hydrocarbons due to the presence of Fe-ion and reduced acidity.

a) Laboratory of Industrial Chemistry, Process Chemistry Centre, Åbo Akademi University, FIN-20500 Åbo / Turku, Finland

[1] Hunger M. and Horvath T., Catalysis Letters 49 (1997) 95.

[2] Tsoncheva T. and Dimitrova R., Applied Catalysis A: General 225 (2002) 101.

[3] Sarkadi-Pribóczki É., Kumar N., Salmi T., Kovács Z. and Murzin D. Yu., Catalysis Letters 93 (2004) 101.

7.2 Ion beam microanalysis of human hair follicles

Zs. Kertész, Z. Szikszai, P. Pelicon[a], J. Simčič[a], A. Telek[b] and T. Bíró[b]

Hair follicle (HF) is an appendage organ of the skin which is of importance to the survival of mammals and still maintains significance for the human race - not just biologically, but also through cosmetic and commercial considerations. However data on the composition of hair follicles are scarce and mostly limited to the hair shaft. In addition, to the best of our knowledge, no data are available concerning the distribution of elements in human hair follicle with various growth and cycling phases.

In this study [1] we provided detailed quantitative elemental distribution of organ-cultured hair follicle in anagen and catagen growth phases using ion microscopy in order to reach a better understanding of the function, development, and cyclic activity of the hair follicle. The microprobe analysis was carried out at the scanning ion microprobe facilities at the ATOMKI Debrecen, and at the Jožef Stefan Institute, Ljubljana, Slovenia, using combined STIM and PIXE ion beam analytical techniques.

Human anagen hair follicles were isolated from skin obtained from females undergoing face-lift surgery. Cultured anagen HFs were treated by either vehicle or by 10 μM capsaicin for 5 days.

Elemental distributions and absolute concentrations were determined along 5 capsaicin treated (catagen), and 4 control (anagen) hair follicles. The investigated length varied between 1.5 and 2 mm. Average elemental concentration values of the whole sample and the different morphological parts were also determined.

Concentrations for most of the elements were found to be the same in the corresponding parts of the anagen and the catagen hair follicles. However, significant differences were observed in the Ca concentration between the anagen and catagen HFs. With respect to the distribution of Ca, in anagen (control) HFs, the following concentrations were measured (given in μg/g dry weight): dermal papilla, ~500; matrix of the bulb, 1000-1500; outer/inner root sheath keratinocyte layers, 1000-2000; hair shaft, 1000-2000. The induction of catagen transformation essentially did not change the Ca concentrations in the dermal papilla, bulb matrix regions nor in the hair shaft (1000-2000 in all parts). In contrast, we observed a remarkable increase in the outer/inner root sheath keratinocyte layers up to 4000-8000 μg/g Ca concentration.

In capsaicin-treated catagen HFs, the Ca concentration was increased mostly in those layers which possess a significant expression of TRPV1, the receptor for capsaicin. Since TRPV1 functions as a Ca-permeable channel, the elevated Ca in the TRPV1-expressing layers suggest that the activation of TRPV1 by capsaicin resulted in a prolonged elevation of intracellular Ca-concentration which, in turn, led to the inhibition of proliferation of HF keratinocytes as well as the induction of HF apoptosis. Moreover, our findings also show that ion microscopy may serve as a fine tool to detect changes in elemental distribution related to the human hair-cycle.

Acknowledgements

This work was supported by the Hungarian-Slovenian Intergovernmental S & T Cooperation programme (contract no. OMFB-00427/2006) and the Hungarian Research Fund (contract no. K063153).

a) Jožef Stefan Institute, Ljubljana, Slovenia

b) Department of Physiology and Cell Physiology Research Group of the H. A. S., University of Debrecen, Medical and Health Science Center, Research Center for Molecular Medicine.

[1] Zs. Kertész et al., Nuclear Instruments and Methods B, in press, ref.: NIMB 54339

8.1 Status Report on Cyclotron Operation

Z. Kormány, P. Kovács, I. Szűcs, I. Ander, F. Tárkányi

The operation of the cyclotron in 2006 was concentrated to the usual 9 months; January, July and August were reserved for maintenance and holidays. As an exception, an extra one-week-long isotope production run (^{48}V and ^{56}Co) was done in the middle of July for the Paks Nuclear Power Plant Company. The overall working time of the accelerator was 3445 hours; the time used for systematic maintenance was 441 hours. The breakdown periods amounted to 62 hours last year. The cyclotron was available for users during 2942 hours. The effectively used beam-on-target time is summarized in Table 1.

Table 1. Statistics of the irradiation time (beam-on-target) for different research groups

Projects	Hours	%
Nuclear spectroscopy	359	21.2
Nuclear astrophysics	630	37.3
Radiation tolerance test	142	8.4
Nuclear reaction data	152	9.0
Medical isotope production	194	11.5
Thin layer activation (TLA)	105	6.2
Total	**1690**	**100**

During the summer shutdown period the construction of a new beam line for the mass separator in vault Nr.6 has been started. The 45° bending magnet, originally used in vault Nr.3, was installed into the straight transport line to deflect the beam to the separator. Other elements of the dismantled beam lines (quadrupole lenses, steering magnets, beam pipe and diagnostic boxes) will also be utilized for building the new transport line.

Two new power supply units (arc and filament heating) for the ion source of the cyclotron have been put into operation. Control and stabilization of the arc were achieved by linking the power supplies via software feedback, which was accomplished by the control code running in the programmable logic controller (PLC).

8.2 Activities at the Van de Graaff Accelerator Laboratory

L. Bartha

During 2006 the beam time of the VdG-1 machine amounted to 1201 hours. The accelerator delivered $^{12}C^{+}$ and $^{4}He^{+}$ beams used for low-energy atomic physics, in 101 and 1100 hours beam time, respectively.

Because of the reconstruction carried out within the framework of Economic Competitiveness Operational Programme (GVOP) (see the article 8.3 in this Annual Report), the 5 MV Van de Graaff machine was put into operation again in September, and was runing for 863 hours. Proton (46.2 %), $^{3}He^{+}$ (27.8 %), $^{4}He^{+}$ (2.7 %) and $^{14}N_2^{+}$ (23.3 %) particles were accelerated.

The beam time was distributed among different research subjects as shown in Table 1.

Table 1. Time distribution among different research activities at VdG-5

Field	**Sign**	**Hours**	**%**
Atomic physics	AP	201	23.2
Nuclear physics	NP	240	27.8
Nuclear astrophysics	NAP	83	9.6
Analytical studies	IBA	181	21.0
Micromachining	MM	39	4.5
Machine tests	MT	119	13.9
Total		**863**	**100**

8.3 Results of the Economic Competitiveness Operative Programme (GVOP): Analytical laboratory

Á.Z. Kiss, L. Bartha, Z. Elekes, Zs. Fülöp, Gy. Gyürky, Zs. Kertész, Z. Pintye, I. Rajta, A. Simon, Z. Szikszai, I. Uzonyi

2006 September was the end of a project run for 18 months in the institute with the aim to develop the old Electrostatic Accelerator Laboratory into an up to date on the world level Nuclear Microanalytical Laboratory. The development was 90 % financed by the EU co-funded Economic Competitiveness Operative Programme (GVOP-3.2.1.-2004-04-0402/3.0) and 10 % by Atomki itself. The total amount of the project was 400.000 Euro, which was supplemented by a considerable amount of mechanical work performed by the workshop of the institute and the technical staff of the laboratory. The project was divided into 6 main parts called "packages", 4 of them were purchasing equipments needed no special installation, and 2 packages where the above mentioned mechanical work was needed. The 6 packages are the followings:

Microscope

Zeiss Axio Imager Optical Microscope (delivered by Carl Zeiss Technika Ltd). Most important specifications: ocular lens and CCD digital camera, objective lenses (5x, 10x, 20x, 50x, 100x), manual focus and stage, transmitted and reflected light illumination, Contrast modes: bright field, ADF (Advanced Dark Field), C-DIC (Circular Differential Intereference Contrast), TIC (Total Intereference Contrast).

X-ray detector + electronics

Si(Li) X-ray detector and electronics were purchased from Gresham Scientific Instruments Ltd. The type of the detector is Sirius30/Be having an active area of 30 mm^2, energy resolution (FWHM) of 136 eV (at 5.9 keV energy) and Dura Be window with thickness of 12.5 μm. The detector is equipped with a manually retractable tube of 14.3 mm diameter aligned 45 degrees downwards and a cryostat of 7.5 l capacity. The preamplifier is a low noise, self restoring one (CDXP) which is connected to a Gresham-type Titan Digital X-ray Pulse Processor. This detector serves for the detection of medium and high energy X-rays in our microPIXE setup. The low energy X-rays are detected with a previously purchased Gresham-type Super Ultra Thin Windowed (SUTW) Si(Li) X-ray detector.

Nuclear electronics

A package of up to date nuclear electronics units was purchased.

ORTEC:
- Model 449-2 Log/Lin Ratemeter/Audible output,
- Model 710 Quad 1-kV Power supply,
- Model 419 Precision Pulse Generator,
- Model 671 Spectroscopic Amplifier/Cable sets,
- Model 142A Preamlifiers,
- Model 474 Timing Filter Amplifiers,
- Model 935 Quad 200 MHz Const.-Fract. Discriminator,
- Model GG8020 Octal Gate and Delay Generator);

MERION:
- Model NU-8205 NIM crate; KineticS:
- Model 1507 Powered CAMAC Minicrate,
- Model 3922-Z1B Parallel Bus Crate Controller,
- Model 2915-ZA PCI Interface to 3922 Controller,
- Sparrow Kmax Linux Driver;

altogether 18 items (delivered by Spektrum Méréstechnika Ltd). With the help of the new nuclear electronics units improved experimental technique can be used in the fields of both ion beam analysis and nuclear astrophysics.

Vacuum coating system

Leybold UNIVEX 350 Vacuum Coating System (delivered by Kon-Trade+ Ltd). The evaporator provides the possibility of thermal and electron beam evaporation. The system is equipped with computer controlled vacuum system, programmable electron beam sweeper, film thickness monitor, automatic source shutters and rotatable substrate holder.

Oil free vacuum system

To suit the requirements of many fields of basic and applied physics (e.g .: nuclear astrophysics with few 100 keV – few MeV protons and ion beam analysis of thin layers) in our laboratory the vacuum system of the 5 MV electrostatic accelerator has been replaced with a complete hydrocarbon free vacuum system. It consists of oil-free vacuum pumps piston/scroll fore-vacuum pumps and turbopumps (Pfeiffer Vacuum, delivered by Magnificat Ltd), and all the Wilson type vacuum sealings were changed to edge welded vacuum bellows. Except for a few Viton-sealed connection, metal gaskets were applied everywhere. Certain beamlines were separated off by differentially pumped section from the high purity, carbon free vacuum system.

Magnetic Quadrupole Singlet Lens

OM50 (delivered by Oxford Microbeams Ltd), main specifications: cut to micron precision from a single stress-relieved billet of high quality magnet iron. Hyperbolic pole profile and precise four-fold simmetry ensures very pure quadrupole field quality over the 15 mm lens bore diameter. Negligible parasitic aberrations. Nickel plated for a durable finish.

The magnetic quadrupole doublet lens of the scanning nuclear microprobe situated in the 0° beamline of the 5 MV Van de Graaff accelerator was completed with this singlet lens. The newly built quadrupole triplet focusing system was tested both with high and low beam currents. The resulted 20 pA beam intensity at 1.5x1.5 μm^2 focus measured in routine circumstances and the achieved 600×700 nm^2 focus at very low beam current (i.e. 300 Hz proton countrate) corresponds to the results achieved with other microprobes, and as it was expected, they are about 3 times better values from those ones produced by magnetic doublet quadrupole focusing systems also in routine circumstances.

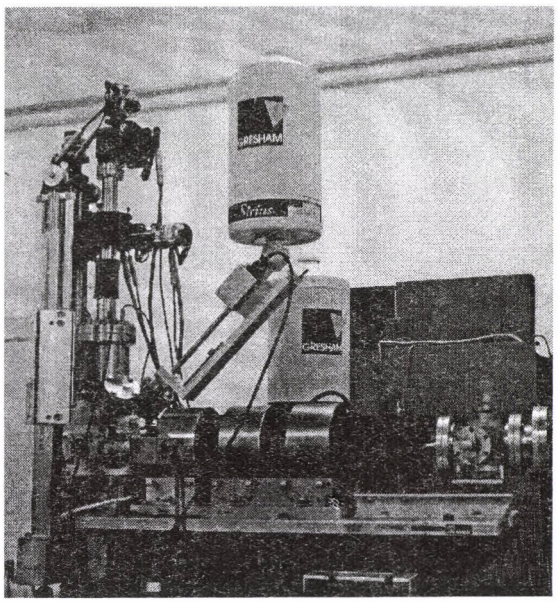

Figure 1. Photograph of the new system

For more information see the web page:
http://www.atomki.hu/atomki/VdG/iba/gvop.html

Magyarország célba ér

NEMZETI FEJLESZTÉSI TERV

A projekt az EU társfinanszírozásával, az Európa Terv keretében valósul meg.

8.4 The micromachined logo of Atomki

I. Rajta and S.Z. Szilasi

Proton Beam Micromachining, also known as P-beam Writing, is a direct write 3-dimensional lithographic technique. Conventional resist types are PMMA (polymethylmethacrylate), and SU-8 (of MicroChem Corp.); they are positive and negative resists, respectively.

In this work we used SU-8, the most common negative resist material. SU-8 was spun on a flat surface, typically Silicon or glass. A direct write proton beam was scanned over an arbitary structure (the Atomki logo can be replaced by any other structure), which produces chain scissioning in the polymer. Post exposure bake (PEB) is usually needed in case of conventional optical lithography, but using protons this bake is done in situ as the ions heat up the sample in vacuum. Subsequently chemical etching takes place, the solvent is available at MicroChem Corp. The schematic diagram of the above described micromachining process is shown on Fig. 1.

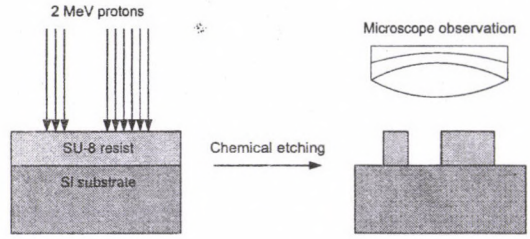

Figure 1. Schematic diagram of micromachining process.

The irradiation requires a scanning proton microbeam system equipped with suitable beam scanning and blanking facilites. This is available in the Institute, our setup has been upgraded from doublet to triplet focusing system (Oxford Microbeams Ltd.). For scanning we use a DIO card (PCI-6731 of National Instruments), and the IonScan software [1].

Sample preparation was carried out at our "semi clean" room. This is also where chemical development of the samples and the optical microscopy have been done too. A Zeiss Axio Imager microscope is available (equipped with 5 objective lenses, 4 different contrast methods, transmitted or reflected light illumination). Fig. 2. shows a typical example of the Atomki logo. This is a bright field image, a number of different nice and colourful images can be produced with the other contrast techniques (for more images see the Institute website: http://www.atomki.hu/).

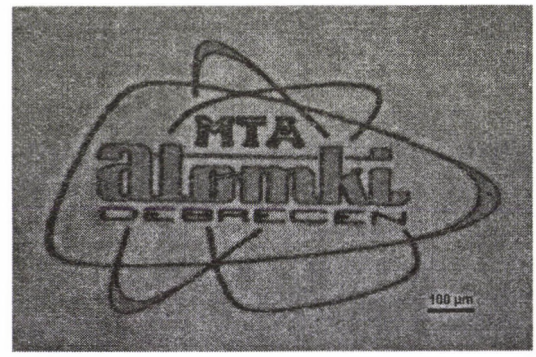

Figure 2. Micromachined Atomki logo.

Acknowledgements

This project was supported by the Hungarian National Research Foundation OTKA (Grant Nos. A080, M041939, M36324 and F042474). I. Raptis and M. Chatzichristidi (IMEL, Athens) provided us with the samples and developer which is gratefully acknowledged.

[1] A.A. Bettiol, C.N.B. Udalagama, J.A. van Kan, F. Watt, Nucl. Instr. and Meth., B231 (2005) 400.

8.5 Refractive index depth profile in PMMA due to proton irradiation

S.Z. Szilasi, I. Rajta, J. Budai[a], Z. Tóth[b], P. Petrik[c], E. Baradács[d]

During Proton Beam Writing the beam damage causes chain scissioning in the polymer resist material (e.g. PMMA (Polymethyl methacrylate)), producing smaller molecular weight chains. Hydrogen implantation also takes place at the end of range. Compaction of the sample has been observed too, which means that the sample density becomes higher at the places where proton irradiation occurred. Furthermore, P-beam Writing has been successfully used to create buried channel waveguides in PMMA [1], since proton irradiation increases the refractive index.

There are two ways of fabricating waveguides using P-beam Writing, one of them applies direct micromachining of the high refractive index core followed by the coating of a lower refractive index cladding layer. In this application the refractive indices of the substrate, the core and the cladding have to be known, which should be homogeneous within the whole structure. The other method allows producing buried waveguides. In this case proton beam writing is used to modify the refractive index along the ion path in the sample, where most of the ion energy is deposited near the end of range also known as the Bragg peak. For polymers 10^{-3} refractive index change has been reported, which is usually sufficient for forming waveguides. Those measurements of the refractive index change have been performed by the refracted near field technique.

In this work we used ellipsometry, in order to measure the optical parameters of the P-beam treated sample near the surface, and along the Bragg curve. Ellipsometry measures the change in the polarization state of light occurring during reflection. This change is related to the quality of the reflecting surface (i.e. the physical structure, layer thicknesses, optical constants, surface roughness, etc.). From these measurements the refractive index and the extinction coefficient can be determined rather accuratly, which makes ellipsometry a powerful tool for the determination of optical properties.

All irradiations in this work have been performed on the 5 MV Van de Graaff accelerator of the Institute. The samples were Röhm GS233 type PMMA. The main irradiation parameters were: ~2 MeV proton energy and 100 nC/mm^2 fluence, because these are typical values for P-beam Writing on PMMA.

In this experiment, what we called "PMMA foil method", the proton energy was varied in the range 1.7-2.1 MeV. A 50 μm thick PMMA foil was attached to the top of bulk PMMA samples in order to decelerate the protons. Depending on the used energy, different energy delivery levels were reached at the bulk PMMA surface (Fig. 1.).

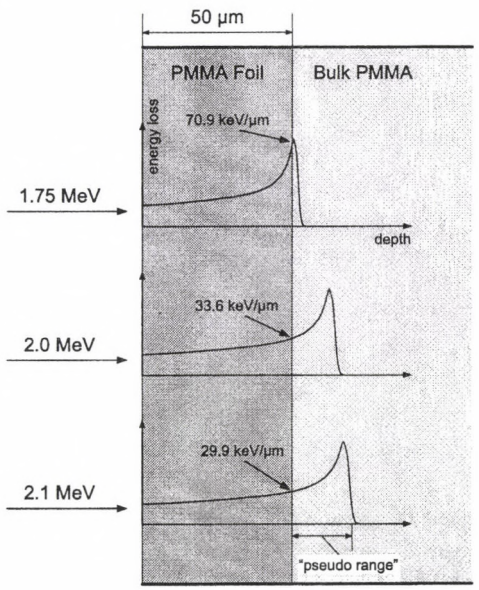

Figure 1. 50 μm PMMA foil placed on top of a bulk PMMA, and the proton energy was chosen between 1.7-2.1 MeV to place the end of range near the bulk PMMA surface.

The ellipsometric analyses were performed on a Woollam M2000F rotating compensator ellipsometer in Szeged. The measurements were carried out at 476 different wavelengths

in the range of 245-1000 nm. The angle of incidence (50°, 52°, 54°, 56°, 58°) was chosen to be near the Brewster-angle of PMMA.

From the ellipsomtric measurements the refractive index and the extinction coefficient as a function of the wavelength can be determined by a special modeling procedure. For full details of this work see the complete paper [2]. Here we present one particular visualisation of the results. In the investigated proton energy range the Bragg curves behave similarly, the protons slow down by many collisions of small energy transfer to the electrons of the sample. We calculated the energy loss $\Delta E/\Delta x$ for the 1.7-2.1 MeV protons after passing through 50 μm of PMMA, then we found the same energy loss value on the 2 MeV protons Bragg curve in bulk PMMA. Having the refractive index values at the 1.7-2.1 MeV protons at 50 μm depth, we plotted the refractive index values caused by 2 MeV protons at the calculated depths. Fig. 2. shows these results. In addition we also plotted the Bragg curve of 2 MeV protons on the same depth scale.

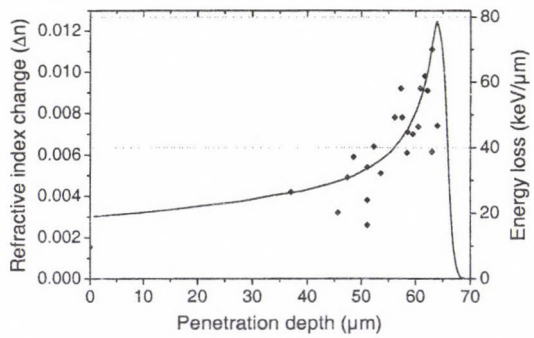

Figure 2. Refractive index change of PMMA at 633nm as a function of ion penetration depth. For comparison the Bragg curve was plotted on the same graph, and one can see a good correlation.

Since the agreement between the measured refractive indices and the Bragg curve looks very good, we concluded that the assumption above was good, i.e. the primary reason of the refractive index change is due to the deposited energy. Since at the end of range implantation also occurs, we can not rule out the possibility that implanted ions (protons will pick up an electron and the hydrogen will certainly find an open chain to connect to) have also an effect on the refractive index. This also takes place where the ion energy loss is the highest, it always appears at the same region. A slight increase of extinction coefficient (or absorbance), resulting in only low propagation losses, was also observed.

Acknowledgements

This project was supported by the Hungarian National Research Foundation OTKA (Grant Nos. A080, M041939, M36324, F042474 and TS049872).

a) Department of Optics and Quantum Electronics, University of Szeged, Hungary

b) Research Group on Laser Physics of the HAS, Szeged, Hungary

c) Res. Inst. for Techn. Phys. and Mat. Sci. of the HAS, Budapest, Hungary

d) Dept. of Environ. Phys., Univ. of Debrecen,

[1] T.C. Sum, A.A. Bettiol, H.L. Seng, I. Rajta, J.A. van Kan and F. Watt, Nucl. Instr. and Meth., B210 (2003) 266.

[2] I. Rajta, S.Z. Szilasi, J. Budai, Z. Tóth, P. Petrik, E. Baradács, in Press: Nucl. Instr. and Meth. B

8.6 Performance test of a new graphite target production facility in ATOMKI

L. Rinyu, I. Futó, Á. Z. Kiss, M. Molnár, É. Svingor, G. Quarta[a)], L. Calcagnile[a)]

Radiocarbon dating by gas proportional counter system has a long tradition in ATOMKI. The institute aimed to enlarge its ^{14}C dating possibilities by the installation of the tandetron accelerator facility obtained from Oxford Radiocarbon Accelerator Unit (ORAU). Laboratory of Environmental Studies Group has been developing the sample preparation system for AMS radiocarbon dating measurements. Performance test of the gas handling line and the graphite target production system was the first step towards the realization of the system in collaboration with CEDAD, University of Lecce.

Graphite is produced by hydrogen reduction of carbon dioxide gas over an iron powder catalyst [1]. The schematic of our gas handling line is shown in Figure 1.

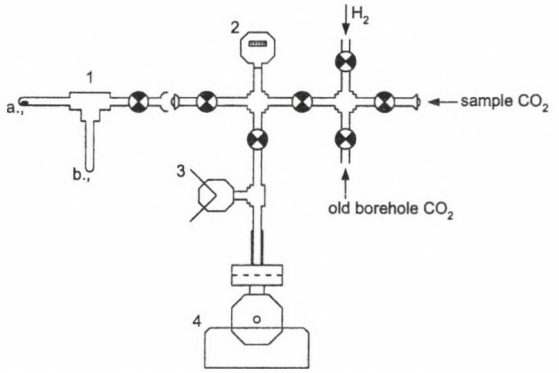

Figure 1. The gas handling line. (1) Reaction rig; (a.,) quartz tube containing the iron powder; (b.,) reusable water trap tube; (2) Digital pressure gauge; (3) Vacuum gauge; (4) Two-stage oil sealed vacuum pump.

^{14}C background of the gas handling line and the graphite target production system was tested by graphitization of old borehole carbon dioxide gas (^{14}C dead, purity 4.5, Linde AG, Répcelak, Hungary), at different furnace temperatures and by using different iron powder preactivation methods.

We also checked the memory effect of the system by graphitization of modern CO_2 gas, which has significant ^{14}C activity, between graphitization of inactive old borehole carbon dioxide gases. The modern CO_2 gas was prepared in the gas preparation line of our GPC system from a VIRI A sample, we obtained in the frame of Fifth International Radiocarbon Inter-comparison program.

After the performance test of our new system we found that the adequate hydrogen and carbon dioxide ratio was approximately 2.1, the temperature of the furnace during the graphitization process was 580 ^{o}C and we got better results when we left out the oxidation step from the iron powder activation process. All of these conditions are for mg size graphite samples.

The investigation of the ^{14}C background level of the gas handling line and the graphitization system gave good agreement with the CEDAD's sample processing background value [2]. The memory effect in our system was eliminated on the score of ^{14}C concentration measurements results. The AMS results of modern ^{14}C graphite samples were also good agreement with the consensus value.

a) CEDAD, Department of Engineering of Innovation, University of Lecce, Italy

[1] J.S. Vogel, D.E. Nelson and J.R. Southon, NIMB 5 (1984) 289.

[2] L. Calcagnile, G. Quarta, M. DElia, A. Rizzo, A. Gottdang, M. Klein and D.J.W. Mous NIMB 223-224 (2004) 16.

8.7 Transformation of the ATOMKI-ECRIS into a Plasma Device

S. Biri, É. Fekete, I. Iván, I. Gál

In order to extend the capabilities of the electron cyclotron resonance (ECR) ion source (ECRIS) of ATOMKI it has been transformed into a special plasma facility [1,2]. The transformation is reversible and was simply done by changing several main components of the ion source by new ones, namely: the hexapole magnet, the plasma chamber and the microwave source. The basic requirements of the transformation were: (1) most parts of the present ECRIS should be used in the new assembly in the same way and (2) the transformation time between the two operation modes should not be more than 2-3 days (in both directions). The following sub-systems are used identically in both configurations: solenoid coils, vacuum system, gas dosing system, ovens, probes. The extraction optics and beam transport system can also be used in the new configuration to check the components and charge-state of the plasma.

A new, large, but unusually thin cylindrical NdFeB hexapole magnet was designed with large internal and external diameters. Additionally, elementary trapezoidal magnetic blocks with different orientation of magnetism were also purchased to assemble later other types of multipoles (8-pole, 12-pole or open 6-pole). Every multipole produces a magnetic field larger than 0.6 Tesla in the plasma chamber so resonance frequencies upto around 13...14 GHz can be coupled (for 12-poles upto 12 GHz).

After the hexapole was delivered we designed and manufactured a new, large-size plasma chamber with water cooling in all its walls around. The geometrical data of the hexapoles and chambers are shown in Table 1. We note that the diameter of the old plasma chamber is 58 mm, while the new one is almost twice as large (102 mm). The large size at the injection side makes an easy access to the plasma (ovens, sample holders, electro-static probes, motion feedthroughs, water cooling, etc.). Another plasma chamber will be designed and fabricated for the other three multipoles (to be formed from individual pieces) in next years.

Table 1. Comparison of the multipoles and plasma chambers

	Old hexapole, glued	New hexapole, glued	Multipoles made from elementary blocks (not glued)		
			6-pole	8-pole	12-pole
Material (NEOREM)	490i/400i	537i	537i		
Sections*segments	2*24	3*24	3*24		
Internal Diameter (mm)	65	115	115		
External Diameter (mm)	135	155	155		
Length (mm)	200	240	242		
Plasma chamber ID (mm)	58	102	100		
Plasma chamber length (mm)	180-250	200-400	200-400		
Magnetic induction at chamber wall (T)	0.95	0.65	0.64	0.62	0.54
Plasma volume (liter)	0.7	> 2	> 2		
Microwave frequency (GHz)	14.5	6.5-13.6 variable	6.5-13.6 variable		
Microwave power (W)	10-1000	0.1-20	0.1-20		

We can keep and use the present high power klystron-based 14.5 GHz microwave amplifier with the new hexapole, as well. Meanwhile two low-power, wide-frequency traveling wave tube amplifiers (TWTA) were also purchased (10 W, 6.5-13.6 GHz and 20 W, 8-18 GHz) and tested.

The new ECR plasma source was assembled and plasmas were successfully and easily produced at 9.2 GHz frequency by one of the TWTAs. Figure 1 shows the modified ATOMKI-ECRIS with the new hexapole and chamber.

Actually a new facility with two sharply different operation modes was established: the "old" ECR ion source will be used to produce highly charged ion beams and the "new" ECR plasma device described in this paper will form large-size, low-charged plasmas for materials research and for plasma experiments and investigations.

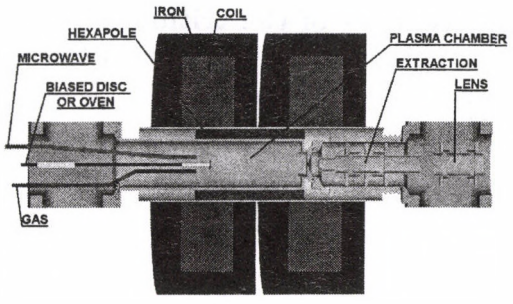

Figure 1. The ATOMKI-ECRIS with the new hexapole and plasma chamber.

[1] Biri S., Fekete É., Iván I., Gál I. 17th Int. Workshop on ECR Ion Sources (ECRIS'06). Lanzhou, China, September 2006. Proceedings will be published in the High Energy Physics and Nuclear Physics.

[2] Project number: GVOP-3.2.1-2004-04-0054/3.0.

8.8 Analysis of the tritium gas sample by gas chromatography: one of the basic steps in the fuel cycle of the ITER

Z. Szűcs

The international consortium (EU, USA, Russia, Japan, South Korea, China and India) signed a formal agreement to build the *International Thermonuclear Experimental Reactor (ITER)* on November 21, 2006. The official objective of ITER is to "demonstrate the scientific and technological feasibility of fusion energy for peaceful purposes". The deuterium-tritium fusion process releases roughly three times much energy as uranium 235 fission and millions of times more energy than a chemical reaction such as the burning of coal or hydrocarbons. It is the goal of a fusion power plant to harness this energy to produce electricity. The Atomki recognized this perspective trend at time and it was involved into the fusion research by the Hungarian Fusion Association from September 2005. This short communication is referring about the cooperation, which was realized between the Atomki and the Tritium Laboratory Karlsruhe (TLK) in field of the analysis of the tritium gas samples from spring of 2006.

The tritium is one of the main important fuel materials for the fusion reactor. As a radioactive gas it needs special attention for its handling and analysis. In the TLK has been developed gas-chromatographic technology for checking of the tritium gas sampling, origin from the different parts of the Tritium Plant. However this method is already 14 years old and the old staff was changed 2 years ago, loosed some important knowhow at the same time. Therefore was necessary to check the system and to carry out some important maintenance. All of them are summarized in the following 4 points:

1. The continuously increasing of the retention time of the Porapack Q column created the question: Nor the resin phase of the column already damaged or the resin works properly and any other effect (leak on the pipe system or in the valves or in pressure regulators, changing of the inlet and outlet pressure and the changing of the ratio of the flow rates) occurs this effect. The comparison of the old and the new theoretical plates (TP) of the column can answer for this question. The determination of the theoretical plates (TP) was done by a few chromatograms, which were only store. The calculation was made by the following equation:

$$TP = 16(Rt/w)^2$$

where the "w" is equal with the latitude of the peak measured in the inflection point to baseline. The result can be seen in Table 1.

Table 1. Comparison of the old and newly determined TP values

Date	Rt(CO_2)	Rt(O_2)	TP(CO_2)	TP(O_2)	T (°C)
20.01.06	8.47	2.47	2534	2087	40
21.02.06	8.49	2.4	1858	1764	40
21.03.06	8.8	2.54	1010	1284	40
11.04.06	9.08	2.48	1925	2187	40
17.03.97	5.25		1764		40

From the comparison it is clear that the TP not changed significantly through the last 10 years. It means that the Porapack column is a good working condition yet.

2. The requirement of the separation between the H_2 and N_2 ($\geq 1.5 * (0.5w_1 + 0.5w_2)$) can be fulfil more easy using the lower temperature. In +40 °C (now this is the routine working temperature) there is a risk to cut some hydrogen sample to the minor contaminating gas analysis or to cut some nitrogen to the Q_2 sample, destroying the separation on the Alox column. Therefore the temperature of the separation was optimised by the separation factor and was suggested to use as 5 °C.

3. During the optimization of the separation temperature were necessary to reregulate the

flow rate of the carrier and make up gases. This procedure discovered several major and minor defects in the GC and they were fixed: He leaks in the injectors, H leak in the He-detector, broken needle valves, old gas purifier.

4. After the maintenance of the GC the system was recalibrated with the new reference gases in three different concentration regions. The systematic investigation discover the fact, that the O_2 reference gas in the ppm concentration range practically "disappears" due to an oxidation or absorption effect on the iron surface of the gas bottle during 1 month. Therefore the reference gas mixtures are useable to calibrate the GC only for the N_2, CO, CH_4 and CO_2. The calibration for the N_2 needs more attention because of the additional small amount of the N_2, which is also loaded from the N_2 air of the box in to the column due to the very small leak of the sample injector. The practice shoved that the determination of this "added N_2" is more easy by the mathematical calculation and it is easy to omit from the measured N_2 than the fixing this small leak in the injector. The following chart explains the calibration data for the N_2, where the intersection point of the trend line on the "y" axis line determinates the value of the "added N_2".

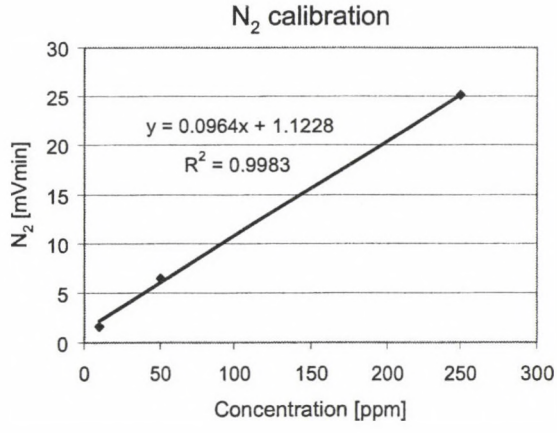

Figure 1. Calibration curve of N_2 on the GC. Evaluation of the regression of the data and determination of the "added N_2" by the intersection point on the "y" axis.

If the concentration of the contaminating N_2 gas in the tritium gas sample is expected under 50 ppm, it is necessary to calculate this "added N_2" for the exact measurement.

This half year work with the GC of the TLK shoved that this type of the GC is able to analyse the tritium gas samples yet, but it is also necessary more attention for the maintenance in the future even to develop a new design of the GC, which can warrant the more easy reparation of the GC.

8.9 Design and construction of ion sources for the isotope separator

M. Hunyadi, Z. Gácsi

As part of the installation of the isotope separator a surface-ionization and an electron-impact ion sources were designed and constructed to meet specific requirements of various proposed applications at this facility [1]. A surface-ionization ion source was constructed based on the ANUBIS design [2] for the purposes of producing μA beams of high melting point elements with low ionization energies. On the other hand, ion beam implantation techniques and isotope enrichment may need much higher beam currents and a broader range of elements. In this respect, the choice of a Freeman electron-impact ion source was found the most appropriate [3]. This type of ion source is almost exclusively employed in ion implanters all over the world, which is partly due to its excellent and stable operational parameters including high efficiency, milliamper beam currents and good energy resolution, and also to the ease of its operation and maintenance. In addition to gases, for ionizing solid elements or compounds with melting point of moderate temperatures an oven can also be attached to the arc chamber, as well as samples can be placed inside the arc chamber for sputtering techniques.

A prototype of a Freeman ion source has been designed and built in Atomki, which is currently in testing phase. Using noble gases for ionization, limits on extracted beam currents have been reached due to the capacity of power supplies and electronic units presently available at the separator laboratory. The high beam current in the range of few mA is provided primarily by the high plasma density created around a straight filament with a diameter of 1.5-3 mm heated by 150-180 A d.c. The filament, the arc chamber and its holder elements are typically made of refractory metals (tungsten, molybdenum, tantalum), while high-current feedthroughs are made of copper. All insulator components and the oven are manufactured from boron nitride and alumina.

In parallel, the construction of the beam extraction and focusing electrodes are still in progress, together with the development of a complete electronic control system, which is planned to provide optimized operational conditions for both the ion source and beam transport for the isotope separator.

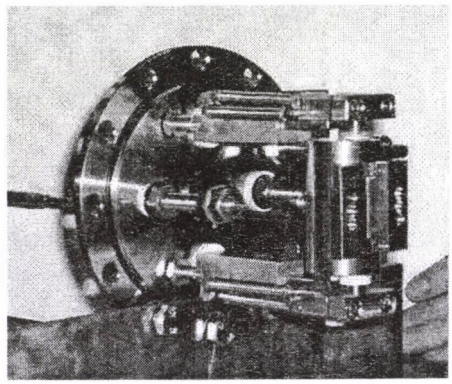

Figure 1. The Freeman ion source constructed in Atomki for isotope enrichement and implantation purposes at the isotope separator.

[1] Z. Gácsi, *et al.*, Atomki Ann. Rep. 70 (2005)

[2] L. Jacobsson, *et al.*, Nucl. Instr. Meth. **B26** 223 (1987)

[3] J.H. Freeman, Nucl. Instr. Meth. **22** 306 (1963)

8.10 Capacitance-voltage investigation of silicon photodiodes damaged by MeV energy light ions

G. Kalinka, A. Simon, M. Novák, M. Jakšić,[a], Ž. Pastuović[a], Á.Z. Kiss

Nuclear radiation creates not only deep centers, but in addition influences shallow dopant concentration in semiconductors, as well. At a given temperature the maximum frequency a center can respond to depends on its energy level, therefore the capacitance-voltage (C-V) characteristics of radiation damaged semiconductor diodes should ideally be measured as function of frequency in order to obtain the physical and energy depth distribution of ionized centers [1,2]. In our experiments C-V plots of MeV energy ion irradiated photodiodes were taken at fixed 1 kHz frequency, which is low enough to be sensitive at room temperature to some of the deep levels expected. During, for example, an irradiation with 5.5 MeV α particles the capacitance of a p^+nn^+ diode increased significantly at low voltages, but showed rather small changes at higher ones. The former turned out to be merely related to a decrease of the built in voltage, corresponding to a lifetime to relaxation type transition of the semiconductor [3]. Rescaling C-V data for this change, the remaining, actual capacitance changes could be interpreted as related to nuclear recoil caused damage located around the end of particle tracks.

C-V technique has also been used for follow up investigation of spontaneous self annealing at room temperature of irradiated samples. This is shown here by plotting capacitance data normalized to their virgin values as function of depletion depth for irradiation with 430 keV protons, whose range is about 5 μm. The sensitivity of the method is illustrated for low fluence of 6.5 MeV oxygen, whose range is 5 μm, too, and where the normalization is now made to data taken one week after the irradiation.

Acknowledgement

This work was supported by the Hungarian Research and Technology Innovation Fund and the Croatian Ministry of Science, Education and Sports within the framework of the Hungarian-Croatian Intergovernmental Science and Technology Co-operation Programme (Project code: HR-31/2004) as well as by the International Atomic Energy Agency under the CRP contract No. 13261/R0.

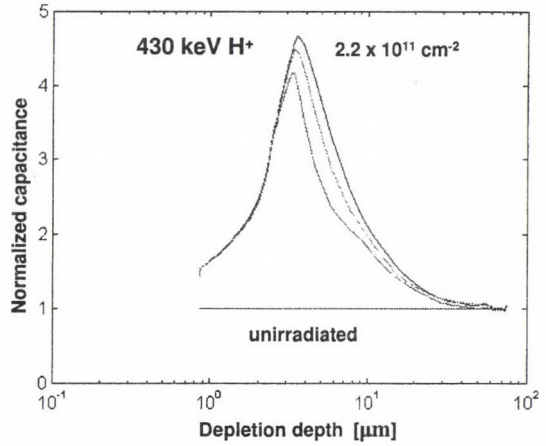

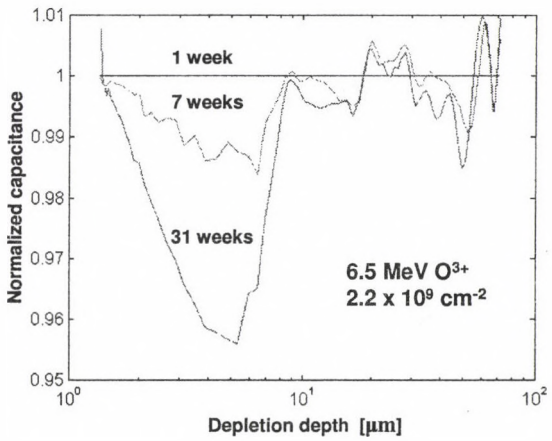

a) Ruđer Bošković Institute, Zagreb, Croatia

[1] W. Dąbrowski and K. Korbel, Nucl. Instrum. Meth. A276 (1989) 270

[2] Z. Li and H.W. Kraner, IEEE Trans. Nucl. Sci. NS-38 (1991) 244

[3] M. McPherson, Physica B 344 (2004) 52

8.11 Generation and diffusion current components in reverse biased charged particle irradiated Si pin photodiodes

G. Kalinka, M. Novák, A. Simon, M. Jakšić,[a)], Ž. Pastuović[a)], Á.Z. Kiss

Energetic radiation creates lattice damage in solids. In semiconductor detectors this translates to extra energy levels in the forbidden gap of the semiconductor. These bring about an increase of leakage current, reduction of charge collection efficiency, changes of detector capacitance, etc. Since the reverse leakage current of advanced silicon photodiodes, widely used for detection of nuclear radiation, is rather low, measurement of irradiation induced current is a very sensitive tool for monitoring radiation damage in the diode. The reverse leakage current in semiconductor diodes consists of generation and diffusion components. The former originates from carriers thermally generated in the depleted region, whereas the latter from carriers generated outside but diffusing into the depleted region. For uniform generation throughout the whole diode, generation current scales with the depleted volume, therefore an extrapolation of the total current to zero volume gives the (saturation) diffusion current [1]. In diodes irradiated with short range charged particles, the generation center distribution is nonuniform, thus the above method is inapplicable.

Taking, however, I-V plots starting from voltages much less than the thermal voltage kT/q, one can easily separate total diffusion current component. After subtracting the diffusion current, what remains is the generation component. This procedure can, of course, be done in virgin and irradiated state, alike, as seen in Fig. a. A set of I-V plots for different fluences of 5.5 MeV α-particles is shown in Fig. b. From these data an almost exact linear relationship has been obtained for the fluence dependence of generation current in the whole fluence range, in accord with literature data [2], while the diffusion current showed strong sublinearity below 3×10^8, and slight supralinearity above 8×10^8 ions/cm^2.

Acknowledgement

This work was supported by the Hungarian Research and Technology Innovation Fund and the Croatian Ministry of Science, Education and Sports within the framework of the Hungarian-Croatian Intergovernmental Science and Technology Co-operation Programme (Project code: HR-31/2004) as well as by the International Atomic Energy Agency under the CRP contract No. 13261/R0.

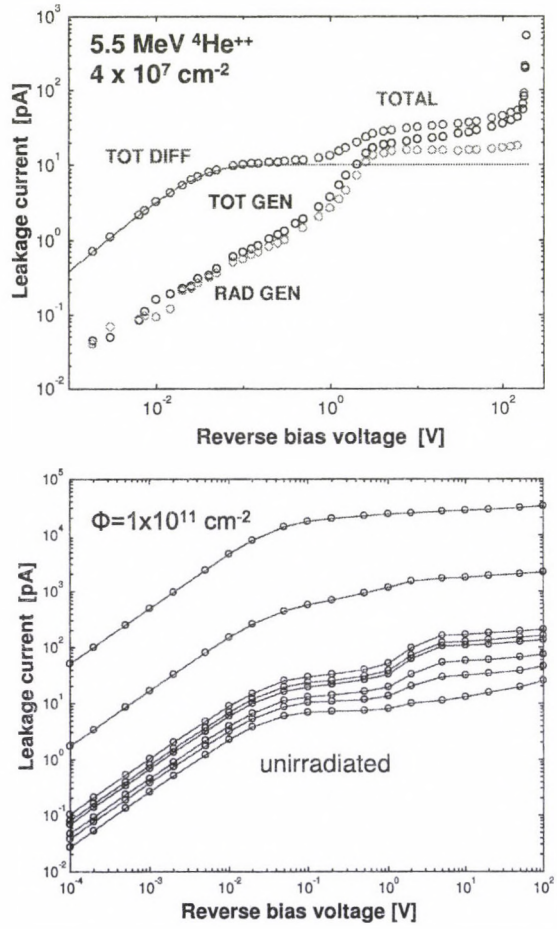

a) Ruđer Bošković Institute, Zagreb, Croatia

[1] E. Simoen *et al.*, Appl. Phys. Lett. 72 (1998) 1054

[2] R. Wunstorf, PhD Thesis, Universität Hamburg, 1992

8.12 Performance degradation of Si pin photodiodes, used as particle detectors, under 2 MeV proton irradiation

A. Simon, G. Kalinka, M. Jakšić,[a)], Ž. Pastuović[a)], M. Novák, Á.Z. Kiss

Nowadays high quality Si pin photodiodes are cheap and reliable alternatives to nuclear semiconductor detectors for a wide range of application, especially for charged particle detection. Normal silicon with low oxygen content, however, is known as having low radiation tolerance. Therefore, the performance degradation of Hamamatsu S-5821 diodes has been investigated as a function of fluence for a series of ions.

Selected areas of a photodiode were irradiated with various fluences of 2 MeV protons in the range of $1 \times 10^9 - 5 \times 10^{11}$ ion/cm^2 without applying any bias. In order to investigate the impact of the irradiation on the particle detection response of the diode the radiation induced changes were measured with IBIC mapping using also 2 MeV protons in a wide range of reverse bias, from 0 to 100 V in logarithmic steps. The major influence of the irradiation is the decrease of the charge collection efficiency (CCE), i.e. the shift of the spectral peak position towards lower energies, and the increase of the dispersion of CCE, i.e. the widening of the spectral peaks, in other words the increase of the FWHM values, Δ. Since within the irradiated regions these quantities show strong position dependence due to boundary effect, the evaluation of the experimental data was restricted to the central homogenous parts. Quantitative empirical relationships above 10 V bias for the radiation induced contributions to the CCE and FWHM have been deduced as follows [1]:

$$\delta(CCE)_{rad} = (-3.3 \pm 0.5) \times 10^{-13}\, \Phi[cm^{-2}]/U[V]$$

$$\Delta_{rad}[keV] = (4 \pm 1.5) \times 10^{-5} \sqrt{\Phi[cm^{-2}]}/U[V]$$

These contributions add linearly to irradiation free CCE, and quadratically to FWHM values, respectively. Since the effect of the irradiation - both on CCE and FWHM - is inversely proportional to the applied bias voltage, it can be significantly reduced by applying the possible highest bias without breakdown or increase of electrical noises due to increased leakage current. In this respect the particular diode investigated is a good choice, since several units can withstand higher than 300 V reverse bias.

Acknowledgement

This work was supported by the Hungarian Research and Technology Innovation Fund and the Croatian Ministry of Science, Education and Sports within the framework of the Hungarian-Croatian Intergovernmental Science and Technology Co-operation Programme (Project code: HR-31/2004) as well as by the International Atomic Energy Agency under the CRP contract No. 13261/R0.

a) Ruđer Bošković Institute, Zagreb, Croatia

[1] A. Simon *et al.*, Nucl. Instrum. and Methods B, in press

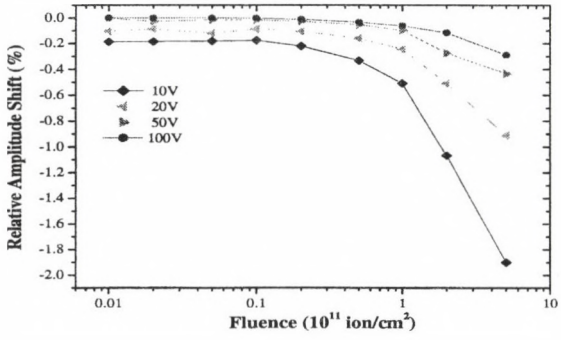

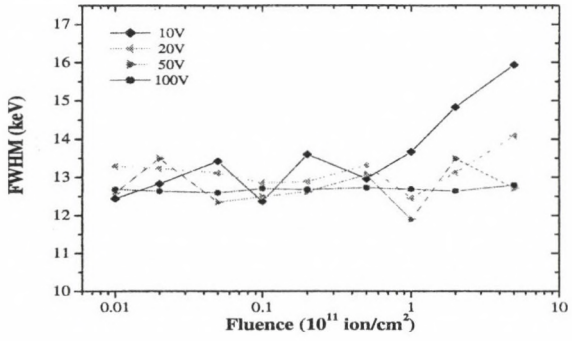

8.13 Monte Carlo code for the study of laser-matter interactions. The case of classical description.

K. Tőkési

In the last years advanced laser facilities have achieved intensities of the order of $10^{15} W/cm^2$ and pulse lengths of the order of 10 fs., which corresponds to few cycles of an electrical field of 800 nm wavelength [1]. The process of interaction of such short and strong pulses with matter is a topic which has attracted much interest recently. In the multiphoton regime, many experimental [2] and theoretical studies have been performed. In the tunneling regime, on the other hand, recent experiments [3] with linearly polarized lasers have shown structures in the momentum distribution of the photoionized electrons in rare gases which have not been fully understood so far. The role of interference in few-cycle pulses is actually been both theoretically and experimentally investigated [4].

Moreover, the combined laser and charged particle induced electronic processes either in ion-atom or ion-surface collisions are of considerable interest both for basic and applied sciences. In fundamental point of view they might broaden our general understanding of the dynamics of atomic processes for laser-matter interactions and field-free collisions. In the application point of view these studies can help us to find the way for the control of ultrashort quantum processes which are important in number of applications, like for example in laser-drive fusion, in plasma heating, or in the development of fast optical electronic devices.

Along this line, we developed a computer code for the investigation of ion-matter interactions in combined laser and charged particle excitations. The simulation code is based on the classical description of the collisions. In the present case we applied the three-body approximation, i.e. the many-electron target atom was replaced by a one-electron atom and the projectile ion was taken into account as one particle. Therefore in our model the three particles are the projectile, one atomic active target electron, and the remaining target ion, including the target nucleus and the remainder target electrons. The three particles are characterized by their masses and charges. The laser interaction in length gauge and dipole approximation is characterized by the oscillating electric field:

$$\vec{E}(t) = \vec{P} E_0(t) \sin(\omega t + \delta),$$

where ω is the frequency and δ is the initial phase. The electric field, $\vec{E}(t)$, is polarized along the direction $\vec{P}$. For the given initial parameters, Newton's equations of motion were integrated with respect to time as an independent variable by the standard Runge-Kutta method until the real exit channels are obtained.

We plan to study the hydrogen atom driven by a classical linearly polarized laser field. We will treat the problem both classically and quantum mechanically. For the first approach our recently developed computer code will be employed where the tunneling effects will also taken into account.

Acknowledgements
The work was supported by the grant "Bolyai" from the Hungarian Academy of Sciences, and the National Office for Research and Technology.

[1] G. G. Paulus et al., Nature 414, 182 (2001); T. Brabec and F. Krausz, Rev. Mod. Phys. 72, 545 (2000).

[2] G. G. Paulus et al., Phys. Rev. Lett. 72, 2851 (1994); G.G. Paulus et al., J. Phys. B 29, L249 (1996).

[3] A. Rudenko et al., J. Phys. B 37, L407-L413 (2004).

[4] F. Lindner et al., arXiv:quant-ph/0503165 (2005).

8.14 The upgraded TrapCAD code

É. Fekete, A. Derzsi[a)] *S. Biri, I. Iván*

The first TrapCAD code [1] was developed in the 90's to visualize the magnetic field line structure of magnetic traps (first of all traps of Electron Cyclotron Resonance - ECR - Ion Sources - ECRIS) and to simulate the movement of individual charged particles in the plasma chamber. The upgraded TrapCAD [2] has a more user-friendly interface and many new features.

The code requires input files containing the magnetic field values generated by the solenoid coils and a multipole magnet in discrete grid points. One output is the graphical display, which helps the user to specify the input parameters and gives impression on the result of the current simulation. The main outputs, however, are the 14 generated text files, which allow the study of some problems using graphical codes as post-processors. Some of the files contain the initial and final attributes of the particles (positions, energies, etc.), some contain other information about the whole system (resonant zone, magnetic map file, etc.).

From the menu one can choose one or both components of the magnetic field, one can switch on or off some effects like 'edge-effect', 'ECR heating', etc., the resonance surface can be calculated and drawn, a two dimensional magnetic map file can be generated, a single field line or set of field lines can be calculated and drawn, simulations of any number of particles can be started from the whole chamber, or from the resonant zone, or from a biased electrode.

In simulations with many (20000 or more) particles after a suitable simulation time the non-lost electrons draw out the shape of the plasma. This is shown in *figure 1*, together with plasma 'slices', which help understand the complicated spatial structure of the ECR electrons. Plasma ions are assumed to have similar structure and shape as the electrons due to the quasi-neutrality principle. This visualization of the plasma fits well with earlier visible light and X-ray photos and also with other simulations (see refs in [2]).

With the help of the output files one can also study the energy structure and distribution of the plasma electrons, can compare the energy spectra of lost and non-lost electrons, can study the time-evolution of the non-lost electron population depending on the starting positions, etc.

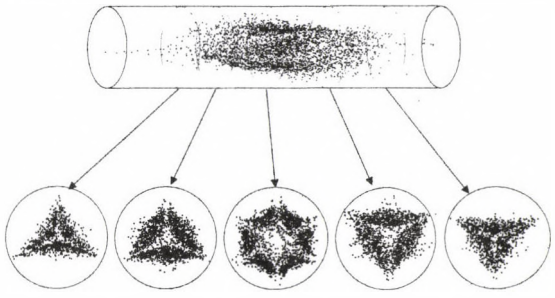

Figure 1. The spatial distribution of electrons in ECR ion sources.

The attributes of the lost electrons are saved in different files, according to the place they hit the wall (injection side plate, extraction side plate, chamber wall). These patterns are in very good agreement with the patterns observed visually in ECRISs. Also the energy distribution of these lost electrons can be examined. The energy distribution of the electrons lost on the injection and extraction plates is in very good agreement with the experimentally measured X-ray distribution curves [3].

The code will be soon available on the homepage of the ATOMKI ECRIS laboratory [4].

a) Babes-Bolyai Univ., Dept. of Physics, Cluj-Napoca, Romania

[1] J. Vámosi, S. Biri, Computer Physics Communications 98 (1996) 215

[2] S. Biri, A. Derzsi, E.Fekete, I. Ivan, accepted for publication in High Energy Physics and Nuclear Physics 2007

[3] C. Lyneis, D. Leitner, D. Todd, S. Virostek, T. Loew, A. Heinen, O. Tarvainen, Rev. Sci. Instr. 77 (2006) 03A342

[4] www.atomki.hu/atomki/ECR/

8.15 Quasiclassical trajectory Monte Carlo method

Á. Mikó, K. Tőkési

The classical trajectory Monte Carlo method (CTMC) is applicable for one electron atomic systems in general because the multi electron atoms are instable due to the electron-electron interactions. The CTMC method was extended by Kirschbaum and Wilets [1] where the multi electron atoms, including all electron-electron interactions, was stabilized via physically justified potentials, built into the classical Hamilton equation (see Eq. 1.). In the quasiclassical trajectory Monte Carlo method (QCTMC) the extra potentials force the fruition of the Heisenberg uncertainty principle ($rp \geq \hbar$, where r and p are the distance and the momentum of an electron with respect to the nucleus) and the Pauli exclusion principle ($r_{ij}p_{ij} \geq \xi_P\hbar$, where r_{ij} and p_{ij} are the relative distance and momentum of two electrons with similar spin, and ξ_P is a constant, characterized the given atomic shell).

In the QCTMC model the Hamiltonian equation can be written as

$$H = H_0 + V_H + V_P \tag{1}$$

where

$$H_0 = T + V_{Coul}. \tag{2}$$

The kinetic energy can be written

$$T = \frac{p_a^2}{2m_a} + \frac{p_b^2}{2m_b} + \frac{1}{2m_e}\sum_i p_i^2, \tag{3}$$

where a and b denote the nuclei and the index i denote the N_a electrons in the atom A and N_b electrons in the atom B. We can write the Coulomb potential as

$$V_{Coul} = \frac{Z_a Z_b e^2}{r_{ab}} - \sum_{\gamma=a}^{b}\sum_{i=1}^{N_a+N_b}\frac{Z_\gamma e^2}{r_{\gamma i}} + \frac{1}{2}\sum_{i,j}\frac{e^2}{r_{ij}}, \tag{4}$$

where $\mathbf{r}_{\alpha\beta} = \mathbf{r}_\beta - \mathbf{r}_\alpha$ $(\alpha, \beta = a, b, 1, 2, \ldots)$. The extra terms for nonclassical constraints can be written as

$$V_H = \sum_{\gamma=a}^{b}\sum_{i=1}^{N_a+N_b} f_H(r_{\gamma i}, p_{\gamma i}) \tag{5}$$

and

$$V_P = \frac{1}{2}\sum_{i=1}^{N_a+N_b}\sum_{j=1}^{N_a+N_b}\delta_{s_i,s_j} f_P(r_{ij}, p_{ij}), \tag{6}$$

where $\mathbf{p}_{\alpha\beta}$ is the relative momentum, and $\delta_{ij} = 1$ if the spins of the ith and jth electrons are the same and 0 if they are different. The extra potentials are in the from

$$f_c(r,p) = \frac{(\xi_c\hbar)^2}{4\alpha_c r^2\mu}\exp\left\{\alpha_c\left[1 - \left(\frac{rp}{\xi_c\hbar}\right)^4\right]\right\} \tag{7}$$

(C=H or P), where μ is the reduced mass, and α is the constant whose precise values is unimportant but affects to the values of ξ . We developed a Monte Carlo code based on the QCTMC model for investigation of ion-atom collisions. As a test, Monte Carlo simulation was performed for the study of the charge exchange cross sections in proton and helium atom collision. The QCTMC cross section are much closer to the experimental values compared to the CTMC data (see Fig. 1).

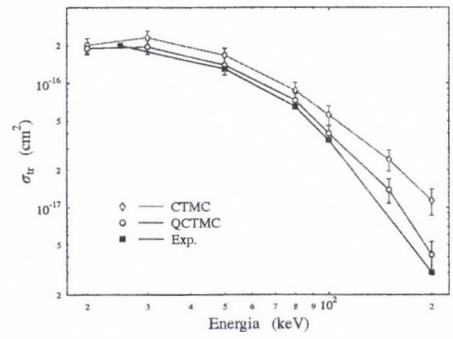

Figure 1. The cross sections of charge exchange process in proton and helium atom collisions.

Acknowledgements

The work was supported by the grant "Bolyai" from the Hungarian Academy of Sciences, and the National Office for Research and Technology.

[1] C. L. Kirschbaum and L. Wilets, Phys. Rev. A**21**, (1980) 834

9.1 Hebdomadal Seminars

12 January
Moore's law and materials characterization
J. Gyulai (*Research Institute for Technical Physics and Materials Science, Budapest*)

23 February
Achievements on the preparations for the ^{3}He+^{4}He experiment at Seattle
C. Bordeanu (*Bucharest*)

23 March
State of affairs
M. Pálinkás, R. Lovas (*Atomki*)

30 March
Planet research in the Solar system and beyond
K. Szatmáry (*University of Szeged*)

4 May
New infrastructure for radionuclide production at iThemba LABS
G.F. Steyn (*iThemba LABS, South Africa*)

18 May
Development of our concept of electromagnetism in the 18th century
Gy. Radnai (*Eötvös Loránd University, Budapest*)

25 May
Young scientists' reports
R. Dóczi, G. Katona, M. Novák, D. Sohler (*Atomki*)

30 May
Introduction to the Scopus database
A. Kmety (*Scopus trainer*)

31 May
Pharmaceutical industry and PET microdose investigations
Cs. Pankucsi (*Institute of Pharmacology of the University of Debrecen*)

1 June
Angular distribution of Ar LMM and Ne KLL Auger-electrons induced in ion-atom collisions
L. Tóth

15 June
Electron scattering from atomic inner shells and multi-charged ions
C.T. Whelan (*College of Sciences, Norfolk, Virginia*)

27 June
From the idea to the product
Open discussion

25 September
Beware of Rotten Compromises: The Moral Foundations of Einstein's Politics
R. Schulmann (*Emeritus Professor of History, Boston University*)

28 September
Hindrance in sub-barrier fusion
S. Misisiu (*National Institute for Nuclear Physics, Bucharest-Magurele*)

18 October
The FAIR project
W. Henning (*GSI, Darmstadt*)

19 October
Astrophysical importance and experimental investigation of the ^{3}He(α,γ) reaction
Gy. Gyürky (*Atomki*)

25 October
Nonequilibrium relaxation analysis on phase and transition
N. Ito (*The University of Tokyo*)

2 November
AMS (Accelerator Mass Spectrometer) and future accelerator plans
L. Bartha (*Atomki*)

16 November
Fragmenting Granular Gases
R.C. Hidalgo (*University of Barcelona*)

23 November
Ettore Majorana (1906-1938), problem of the existence of antineutrino and the double beta-decay
T. Toró (*External member of the HAS, Timişoara, Temesvár, Romania*)

30 November
Searching for the Higgs-boson: present and future picture
P. Igó-Kemenes (*Heidelberg University and CERN*)

7 December
Introduction of new colleagues in Atomki
E. Bene, R. Bereczky, L. Csige, R. Huszánk, A. Kapusi, B. Radics,
Sz. Szilasi, A. Vitéz, G. Vodila (*Atomki*)

14 December
ARXPS investigation of concentration profiles in ultrathin layers -
comparison of different algorithms
I. Cserny (*Atomki*)

19 December
Decay of Nuclear Resonances and Molecules
F. Haas (*IRES, Strasbourg*)

9.2 List of Publications

The list of the Institute's publications can be found on-line at:

http://www.atomki.hu/p2/years/yea02006.htm

Author index